Laboratory studies of new photochemical processes of NO_x and HO_x in the middle and upper atmosphere

中層・高層大気におけるNO_xおよびHO_xの

新しい光化学過程の実験的研究

Tomoki Nakayama

中山 智喜

Nagoya University

2006

報告番号	甲第 6839 号

主 論 文

題 目

Laboratory studies of new photochemical processes of NO_x and HO_x in the middle and upper atmosphere

(中層・高層大気における NO_x および HO_x の新しい光化学過程の実験的研究)

Contents

Abstract

Photochemical reactions of free radical play a crucial role in determining chemical composition of the atmosphere. Odd nitrogen radicals (NO_x = N + NO + NO_2) and odd hydrogen radicals (HO_x = H + OH + HO_2) are important in the middle and upper atmosphere. For example, the catalytic cycle including NO_x is a major removal process of ozone in the lower and middle stratosphere, and the catalytic cycle including HO_x becomes dominant O_3 sink in the upper stratosphere and mesosphere. Therefore, it is important for a reliable assessment of the ozone trend to understand the photochemical processes of NO_x and HO_x. In this study, the laboratory studies on several new important processes of NO_x and HO_x in the middle and upper atmosphere have been performed using laser spectroscopic techniques.

A new technique for high-sensitive detection of the electronic ground state nitrogen atom, $N(^4S)$, and the electronically excited oxygen atom, $O(^1S)$, has been developed in this study. The $N(^4S)$ atoms were detected by vacuum ultraviolet laser-induced fluorescence (VUV- LIF) technique at 120.07 nm which is resonant with the electronic transition N $3s^4P_{1/2} \leftarrow 2p^4S_{3/2}$. The subsequent fluorescence from the excited state is directly observed by a solar-blind photomultiplier. Tunable VUV radiation around 120.07 nm was generated by two-photon resonance four-wave sum frequency mixing in Hg vapor. The $O(^1S)$ atoms were detected by VUV- LIF technique at 121.76 nm which is resonant with the electronic transition $O(3s^1P_1 \leftarrow 2p^1S_0)$. Tunable VUV radiation around 121.76 nm was generated by two-photon resonance four-wave difference frequency mixing in a gas mixture of Kr/Ar. The VUV-LIF technique utilized in this study has a minimum sensitivity of 2×10^9 and 3×10^8 atoms cm^{-3} for detections of $N(^4S)$ and $O(^1S)$, respectively.

In Chapter 3, the formation of $N(^4S)$ from the UV photolysis of Nitrous oxide (N_2O) and impact on NO_x formation in the stratosphere has been described. N_2O is known to be a precursor of NO_x in the stratosphere. Most of stratospheric removal of N_2O transported through planetary boundary layer and the free troposphere to the stratosphere is photolysis by the solar UV radiation around 200 nm, while a small fraction of N_2O reacts with $O(^1D)$ atoms. Stratospheric NO_x production is thought to be due to the reaction of N_2O with $O(^1D)$. If the photodissociation channel of N_2O to

produce $N(^4S)$ + NO exist with a significant yield, it could be a new source of NO_x in the stratosphere. In the present study, the quantum yield for $N(^4S)$ formation from N_2O photolysis has been determined to be $(2.1 \pm 0.9) \times 10^{-3}$ at 193 nm. A sensitivity analysis to assess the impact of the $N(^4S)$ and NO formation from N_2O photolysis on stratospheric chemistry has been performed using a one-dimensional photochemical model. When considering the $N(^4S)$ + NO channel as an additional photolytic sink of N_2O, the steady state NO_x concentration increases up to ~3% around 25 km in comparison with that ignoring the $N(^4S)$ + NO channel.

In Chapter 4, the reaction kinetics of $N(^4S)$ atoms with NO_x have been described. The reaction of $N(^4S)$ with NO is though to act as a sink of NO_x in the upper stratosphere, mesosphere and thermosphere. The experimental technique of laser flush photolysis and the VUV-LIF detection was applied for the first time to the kinetic studies of the reactions involving $N(^4S)$. The $N(^4S)$ atoms were produced following 193 nm ArF laser irradiation of NO and NO_2. The photoexcitation processes of NO and NO_2 giving rise to the $N(^4S)$ formation have been discussed in detail. Based on the measurements of Doppler profiles of $N(^4S)$ atoms and photolysis laser power dependence of the $N(^4S)$ LIF intensity, the $N(^4S)$ formation from NO occurs predissociatively following one-photon absorption, while that from NO_2 includes two-photon processes. The rate constants for the reactions of $N(^4S)$ with NO and NO_2 at 295 ± 2 K have been determined to be $(3.8 \pm 0.2) \times 10^{-11}$ and $(7.3 \pm 0.9) \times 10^{-12}$ $cm^3 molecules^{-1} s^{-1}$, respectively. Those results are compared with the literature data.

In Chapter 5, the collisional relaxation processes of suprathermal $N(^4S)$ atoms, which are relevant to NO formation in the thermosphere, have been described. Although it had been proposed that a significant amount of lower-thermospheric NO molecules came from the reaction of suprathermal $N(^4S)$ atoms with O_2, no experimental evidence of the reaction was available. The reaction barrier of the $N(^4S)$ reaction with O_2 was reported to be ~0.24 eV. In this study, the competitive processes of the inelastic collisions to produce NO and the elastic collisions to thermalize the translational energy of $N(^4S)$ have been investigated for the reaction of suprathermal $N(^4S)$ reaction with O_2 at initial center-of-mass collision energy of about 0.24 - 0.6 eV. The suprathermal $N(^4S)$ atoms which have an average translational energy of 0.92 ± 0.095 eV in the laboratory flame were produced by 193 nm photolysis of NO_2 in bath gas of O_2. Doppler profiles of the $N(^4S)$ atoms were recorded by VUV-LIF detection

of $N(^4S)$, from which the average kinetic energy of the $N(^4S)$ atoms were obtained as a function of thermalization time. No clear evidence of the NO production has been observed, which will be explained by a relatively large value of the thermalization cross section compared with the inelastic collision cross section. Monte-Carlo calculations employing an elastic hard-sphere collision model have been performed to estimate the hard-sphere collision radii and thermalization cross section. The thermalization cross section, which reproduced the experimental results, were (3.8 ± 0.4), (2.8 ± 0.4), (1.8 ± 0.2), and (2.3 ± 0.2) in units of 10^{15} cm^2 for $N(^4S)$ + N_2, O_2, He and Ar, respectively. The thermalization cross sections will make it possible to perform more precise model calculations for NO formation processes in the thermosphere.

In Chapter 6, the photolytic formation of $O(^1S)$ from the UV photolysis of O_3 around 200 nm and its subsequent reactions with small molecules relevant to middle and upper atmospheric chemistry have been studied, and impact on HO_x formation in the stratosphere and mesosphere through $O(^1S)$ + H_2O reaction has been described. The quantum yield for $O(^1S)$ formation from O_3 photolysis at 295 K has been determined to be (2.5 ± 1.1) × 10^{-3}, (1.4 ± 0.4) × 10^{-4} and (5 ± 3) × 10^{-5}, at 193, 215 and 220 nm, respectively. The rate constants for the reactions of $O(^1S)$ with O_2, CO_2, H_2O, O_3 and HCl at 295 ± 2 K have been determined to be (2.85 ± 0.31) × 10^{-13}, (3.09 ± 0.29) × 10^{-13}, (6.38 ± 0.38) × 10^{-10}, (4.63 ± 0.45) × 10^{-10} and (5.47 ± 0.27) × 10^{-10} $cm^3molecules^{-1}s^{-1}$, respectively. Based on the present laboratory data we obtained, impact of the $O(^1S)$ formation from O_3 photolysis on the OH radical formation in the stratosphere and mesosphere has been investigated. It has been concluded that, the reaction of H_2O with $O(^1S)$ produced from O_3 photolysis around 200 nm provides a new source of OH in the stratosphere and mesosphere, which is up to ~2.5 % of the conventional OH production by $O(^1D)$ + H_2O reaction at 30 km altitude in mid-latitude. Implications of the present results for the terrestrial airglow of $O(^1S)$ at 557.7 nm have also been discussed. It has been suggested that the impact of the direct formation of $O(^1S)$ from O_3 photolysis on the volume emission rate is less significant than the formation through the previously proposed Barth mechanism.

The results in this thesis show that the photolytic formation of $N(^4S)$ and NO from N_2O can act as a new source of stratospheric NO_x, and that the reaction of H_2O with $O(^1S)$ which is formed from O_3 photolysis can act as a new source of stratospheric and mesospheric HO_x. These new NO_x and HO_x sources should be taken into account

for detail understanding of the chemical processes in the middle and upper atmosphere. The results also demonstrate that the VUV-LIF technique which developed in the present study is a powerful tool to investigate both the photodissociation of small molecules and the kinetics involving $N(^4S)$ and $O(^1S)$ atoms.

Chapter 1

General Introduction

The Earth's atmosphere is commonly described as a series of layers defined by their thermal characteristic. The lowest layer, called the troposphere, exhibits generally decreasing temperatures with increasing altitudes up to a minimum called the tropopause. The tropopause locates near 12 km at the equator and near 8 km in polar region. Above the tropopause, the stratosphere begins, exhibiting increasing temperatures with increasing altitudes up to a maximum at the level of stratopause located near 50 km. At further high altitudes, the mesosphere begins, exhibiting decreasing temperature again up to a minimum at the level of mesopause near 85 km. The region located above the mesopause is called thermosphere. The temperatures there increase very rapidly with altitude. The altitude range between 12 and 100 km, which almost corresponds to the stratosphere and the mesosphere, is generally called "middle atmosphere". The altitude above 100 km, which corresponds to the thermosphere, is generally called "upper atmosphere". Most of the chemistry in the middle and upper atmospheres is driven by solar light. The photochemical processes of free radicals play a crucial role in determining chemical composition of the middle and upper atmosphere.

In the middle atmosphere, ozone (O_3) is the most important chemical constituent, because it is the only atmospheric specie which efficiently absorbs ultraviolet solar radiation. The ozone concentrations in the middle atmosphere are controlled mainly by catalytic reactions involving the odd nitrogens, NO_x (= N + NO + NO_2), odd hydrogens, HO_x (= H + OH + HO_2), and odd chlorines, ClO_x (= Cl + ClO). The catalytic cycle including NO_x is a major removal process of ozone in the lower and middle stratosphere, and the catalytic cycle including HO_x becomes dominant in the upper stratosphere and mesosphere [1]. Therefore, detailed understanding of the production and destruction processes of NO_x and HO_x in the middle atmosphere is important.

In the upper atmosphere, nitric oxide (NO) is one of the most important constituents. Emission at 5.3 μm from NO is an important cooling mechanism in the

thermosphere [2]. The NO molecules produced in the high-latitude lower thermosphere can be transported into the middle atmosphere where it couples into middle atmospheric chemistry. The understanding of the production and removal processes of NO in the thermosphere is crucial. It has been recognized for many years that observations of the airglow emission rates should provide a powerful tool for remotely sensing the state of the upper atmosphere. The most frequently observed emission is the atomic $O(^1S)$ greenline emission at 557.7 nm. This emission particularly provides the information about the variability of solar activity and atomic oxygen concentration in the upper atmosphere. The understanding of the $O(^1S)$ production processes is also important.

This thesis focuses on the photochemical processes related to NO_x and HO_x in the middle and upper atmosphere. The laboratory studies on some new processes of NO_x and HO_x in the middle and upper atmosphere have been performed using laser spectroscopic techniques. In this chapter, the importance of ozone and chemistry of NO_x and HO_x related to ozone in the middle atmosphere is described. Then, the importance of NO and $O(^1S)$ airglow emission in the upper atmosphere is described in detail.

1.1 Importance of ozone in the middle atmosphere

Ozone is central in highly coupled chemical, radiative, and dynamical processes of Earth's middle atmosphere, as shown in Figure 1.1. Ozone is produced by O_2 photolysis and destroyed by photochemical reactions involving radicals whose concentration depends on the ozone abundance as described below in detail. Ozone and other constituents are transported by winds that are related to the temperature distribution and driven by absorption in the atmosphere of vertically propagating waves. Ozone absorbs solar ultraviolet (UV) radiation between 240 and 320 nm which would otherwise transmitted to the Earth's surface. Such radiation is lethal to simple unimolecuar organisms and to the surface cells of higher plants and animals. Heating of the middle atmosphere following the absorption by ozone of solar UV, visible and Earth-emitted infrared (IR) radiation contributes to characteristic temperature profile of the middle atmosphere. Stratospheric air is statically stable because of the increase in temperature with altitude. Ozone absorption also provides a significant energy source for driving the circulation of the mesosphere and forcing tides in the upper mesosphere

and thermosphere.

The mixing ratio of ozone is typically 100-500 ppbv at tropopause, 3 ppmv at 20 km, 8-10 ppmv at 35 km, and 2 ppmv at stratopause [1,3]. Although the importance of atmospheric ozone has been recognized for more than sixty years, research has intensified dramatically over the last thirty years. Interest has been stimulated by concern that a variety of human influences might lead to detectable changes in the abundance of ozone in the middle atmosphere. It is now apparent that stratospheric ozone concentrations have been declining over past two decades and dramatic depletions of ozone over the Antarctic each year.

In 1930, Chapman [4] first proposed the fundamental ozone-forming and destruction reactions that lead to a steady state concentration of O_3 in the middle atmosphere. The reactions known as the Chapman mechanism are

$$O_2 + h\nu \rightarrow 2O \quad (1.1)$$

$$O + O_2 + M \rightarrow O_3 + M \quad (1.2)$$

$$O_3 + h\nu \rightarrow O_2 + O \quad (1.3)$$

$$O + O_3 \rightarrow 2O_2. \quad (1.4)$$

Because reactions (1.2) and (1.3) rapidly interconvert O and O_3, it is useful to think of the sum of O and O_3 as a single species, odd oxygen ($O_x = O + O_3$). Odd oxygen is produced only in reaction (1.1) and is lost in reaction (1.4). Ozone is the dominant form of odd oxygen below ~60 km.

Until about 1964, it was thought that the Chapman mechanism, oxygen-only reactions, could explain atmospheric ozone abundances. However, improved laboratory measurements of the rate constant of reaction (1.4) indicate that the reaction is considerably slower than previously thought. Then the field measurements indicated that the actual amount of ozone in the stratosphere was about a factor of 2 less than that what was predicted by the Chapman mechanism. Thus, additional ozone destruction pathway(s) are needed beyond reaction (1.4). Bates and Nicolet [5] introduced the idea of catalytic odd oxygen loss process involving hydrogen radicals. Crutzen [6] and Johnston [7] revealed the role of catalytic odd oxygen loss process involving nitrogen oxides. Stolarski and Cicerone [8], Morina and Rowland [9] and Rowland and Morina [10] elucidated the effect of chlorine-containing compounds on ozone chemistry.

The ozone destruction processes that must be added to the Chapman

mechanism take the form of a catalytic cycle involving NO_x, HO_x, ClO_x:

$$X + O_3 \rightarrow XO + O_2 \quad (1.5)$$

$$XO + O \rightarrow X + O_2 \quad (1.6)$$

Net: $O_3 + O \rightarrow O_2 + O_2$,

where X is free radical catalyst. X can be H, OH, NO, or Cl. The above cycle is catalytic in that X is not consumed in the process. The net result of the cycle is the conversion of two odd oxygen species (O_3 and O) to two even species ($2O_2$). Odd oxygen is needed to produce O_3. The relative importance of the cycle corresponding to a particular X species depends on the concentration of X and the rate constants of the reactions in the cycle. For most of such cycles, reaction (1.5) occurs rapidly so that the rate-determining step is reaction (1.6) [1].

Figure .1.2 shows the relative contribution of the HO_x, NO_x, ClO_x cycles as well as of the oxygen-only Chapman reactions to odd oxygen destruction. It is apparent that the catalytic cycles involving NO_x make a major contribution to destruction of odd oxygen in the middle stratosphere, while the catalytic cycles involving HO_x become more important in the upper stratosphere and mesosphere. Chemistry of the NO_x and HO_x in the middle atmosphere is described in detail in the following sections (Section 1.2 and 1.3).

1.2 Chemistry of NO_x in the middle atmosphere

1.2.1 NO_x cycles for ozone loss

The catalytic cycle involving NO_x makes a major contribution to destruction of odd oxygen in the middle stratosphere (25-35 km):

Cycle 1 $NO + O_3 \rightarrow NO_2 + O_2$ (1.7)

$$NO_2 + O \rightarrow NO + O_2 \quad (1.8)$$

Net: $O_3 + O \rightarrow 2O_2$.

In the lower stratosphere, reaction (1.8) is replaced by the photodissociation of NO_2:

$$NO_2 + h\nu \rightarrow NO + O_2 \quad (1.9)$$

The reaction (1.9) nullifies the ozone removal. In the lower stratosphere where ozone is more prevalent, another NO_x cycle is

Cycle 2 $NO + O_3 \rightarrow NO_2 + O_2$ (1.7)

$$NO_2 + O_3 \rightarrow NO_3 + O_2 \quad (1.10)$$

$$NO_3 + h\nu \rightarrow NO + O_2 \quad (1.11)$$

Net: $2O_3 \rightarrow 3O_2$.

Most atmospheric NO_3 formed by reaction (1.10) is removed by photolysis during daytime. The products of photodecomposition are $NO_2 + O$ (in which case there is no net loss of odd oxygen), and $NO + O_2$ (in which case odd oxygen is consumed). The nitrate radical can also react with NO_2 to produce dinitrogen pentaoxide, N_2O_5:

$$NO_3 + NO_2 + M \rightarrow N_2O_5 + M \quad (1.12)$$

N_2O_5 can decompose back to NO_3 and NO_2 either photolytically or thermally. Since its formation does not represent a permanent loss of NO_x. N_2O_5 is a reservoir species for NO_x.

The chemistry involving NO_x is closely intertwined with that of ClO_x and HO_x, for example, by following reactions:

$$NO + ClO \rightarrow NO_2 + Cl \quad (1.13)$$

$$NO + HO_2 \rightarrow NO_2 + OH \quad (1.14)$$

$$NO_2 + ClO + M \rightarrow ClONO_2 + M \quad (1.15)$$

$$NO_2 + HO_2 + M \rightarrow HO_2NO_2 + M \quad (1.16)$$

$$NO_2 + OH + M \rightarrow HNO_3 + M. \quad (1.17)$$

Because ClO and HO_2 are the analogs of NO_2 in their odd oxygen destruction cycles, the occurrence of reaction (1.13) or (1.14) enhances the importance of NO_x destruction cycle but diminishes the ClO_x and HO_x catalytic cycles. Nitric acid (HNO_3), Chlorine nitrate ($ClONO_2$), and pernitric acid (HO_2NO_2) produced in the reactions (1.15-17), save as temporary reservoirs for NO_x, ClO_x and HO_x taking them out of their ozone destruction cycles [3].

1.2.2 Production and destruction processes of NO_x

The principal natural source of NO_x in the stratosphere is nitrous oxide (N_2O) produced at the earth's surface by biological processes. Most of the N_2O transported to the stratosphere through the planetary boundary layer and the free troposphere. Figure 1.3a shows an UV absorption spectrum of N_2O [11]. Figure 1.4 shows solar photon flux at altitudes of 50, 30, and 0 km, respectively, as a function of wavelength at solar zenith angle (SZA) of 50°. The wavelength region between 185 and 220 nm is in so-called "stratospheric window" where non-negligible solar photons can penetrate into the stratospheric altitudes due to the gap of Shumann-Runge band of O_2 and the Hartley

band of O_3 as shown in Figure 1.4. Approximately 90% of N_2O in the stratosphere is destroyed by photolysis around 200 nm as shown in Figure 1.5,

$$N_2O + h\nu \rightarrow N_2 + O(^1D), \qquad (\lambda < 341 \text{ nm}) \qquad (1.18a)$$

where the long wavelength limit given in parentheses indicates the thermochemical threshold for channel (1.18a). The remainder, ~10% of N_2O in the stratosphere, reacts with $O(^1D)$:

$$N_2O + O(^1D) \rightarrow 2NO \qquad (1.19a)$$

$$\rightarrow N_2 + O_2. \qquad (1.19b)$$

Reaction (1.19a) is known to be the main source of NO_x in the stratosphere. About 58% of the $N_2O + O(^1D)$ reaction proceeds via channel (1.19a), the remaining 42% by channel (1.19b) [11].

Although N_2O photolysis has been considered to proceed through channel (1.18a) with an almost unit quantum yield [12], channels (1.18b-d) are also energetically possible.

$$N_2O + h\nu \rightarrow N(^4S) + NO \qquad (\lambda < 248 \text{ nm}) \qquad (1.18b)$$

$$\rightarrow N_2 + O(^3P) \qquad (\lambda < 742 \text{ nm}) \qquad (1.18c)$$

$$\rightarrow N_2 + O(^1S) \qquad (\lambda < 211 \text{ nm}). \qquad (1.18d)$$

If channel (1.18b) occurred with a significant yield, it could be a direct source of NO_x in the stratosphere as shown in Fig. 1.5. In this thesis, the photolytic formation of $N(^4S)$ from the UV photolysis of N_2O through channel (1.18b) and its impact on NO_x formation in the stratosphere have been described in Chapter 3.

The reaction of $N(^4S)$ with NO is considered as the destruction process of NO_x in the upper stratosphere and mesosphere:

$$N(^4S) + NO \rightarrow N_2 + O. \qquad (1.20)$$

The $N(^4S)$ atoms are mainly produced by photodissociation of NO in the middle atmosphere. In this thesis, the reaction kinetics of the $N(^4S)$ with NO and NO_2 have been described in Chapter 4.

1.3 Chemistry of HO_x in the middle atmosphere

1.3.1 HO_x cycles for ozone loss

OH and HO_2 play a critical role in stratospheric and mesospheric ozone chemistry either as direct reactants with odd oxygen or through control of the partitioning within other chemical families. The catalytic cycle involving HO_x

contributes significantly to destruction of odd oxygen in the upper stratosphere and mesosphere.

Above about 40 km, the major catalytic cycles involving OH are

Cycle 3 $OH + O \rightarrow H + O_2$ (1.21)

$H + O_2 + M \rightarrow HO_2 + M$ (1.22)

$HO_2 + O \rightarrow OH + O_2$ (1.23)

Net: $2O \rightarrow 2O_2$,

and

Cycle 4 $OH + O \rightarrow H + O_2$ (1.21)

$H + O_3 \rightarrow OH + O_2$ (1.24)

Net: $O + O_3 \rightarrow 2O_2$.

Between 30 and 40 km, Cycle 5 becomes important:

Cycle 5 $OH + O_3 \rightarrow HO_2 + O_2$ (1.25)

$HO_2 + O \rightarrow OH + O_2$ (1.23)

Net: $O_3 + O \rightarrow 2O_2$.

Below about 30 km, where there are very few oxygen atoms, Cycle 6 becomes dominant:

Cycle 6 $OH + O_3 \rightarrow HO_2 + O_2$ (1.25)

$HO_2 + O_3 \rightarrow OH + 2O_2$ (1.26)

Net: $2O_3 \rightarrow 2O_2$.

The relative importance of the cycles changes as the concentrations of key reactants (H, OH, and HO_2) and the temperature change. Interaction of HO_x with NO_x and ClO_x is important as described in the previous section for the case of NO_x. In addition to the coupling between HO_x and NO_x by reactions (1.14), (1.16), and (1.17), the coupling between HO_x and ClO_x occurred by reactions (1.27) and (1.28) [3]:

$OH + HCl \rightarrow H_2O + Cl$ (1.27)

$HO_2 + ClO \rightarrow HOCl + O_2$. (1.28)

1.3.2 Production and destruction processes of HO_x

The source of HO_x in the middle atmosphere is largely water vapor. Above 60 km, HO_x production is dominated by the photolysis of H_2O at Lyman-α radiation:

$H_2O + h\nu \rightarrow OH + H$. (1.29)

Below 60 km, the oxidation of H_2O by $O(^1D)$ is thought to be the main source of HO_x:

$$O(^1D) + H_2O \rightarrow 2OH. \quad (1.30)$$

The oxidation of methane by $O(^1D)$ has some contributions as a source of HO_x in the lower stratosphere. In turn, the removal of HO_x in the stratosphere and mesosphere occurs by termination reactions leading to the formation of water vapor or hydrogen peroxide [13,14]:

$$OH + HO_2 \rightarrow H_2O + O_2 \quad (1.31)$$

$$HO_2 + HO_2 \rightarrow H_2O_2 + O_2 \quad (1.32)$$

$$H + HO_2 \rightarrow H_2 + O_2. \quad (1.33)$$

Production of OH in reaction (1.30) is initiated by the photolysis of O_3 at wavelength shorter than about 320 nm to produce $O(^1D)$ as shown in Figure 1.6. Most of the $O(^1D)$ atoms is quenched to ground state atomic oxygen, $O(^3P)$, by collisions with N_2 or O_2, but a small fraction of $O(^1D)$ reacts with H_2O to produce OH. Ozone molecule has huge absorption cross-sections in the UV between 200 and 300 nm. The UV absorption spectrum reported by Malicet et al. [15] is shown in Figure 1.3b. There are various pathways for ozone photolysis, as listed in Table 1.1 along with their thermochemical threshold wavelengths [16]. The following two spin-allowed dissociation channels have been believed to be dominant in the photolysis of O_3 between 230 and 300 nm with reported quantum yields of ca. 0.9 and 0.1 [17]:

$$O_3 + h\nu \rightarrow O(^1D) + O_2(a^1\Delta_g) \quad (1.34a)$$

$$\rightarrow O(^3P) + O_2(X^3\Sigma_g^-). \quad (1.34b)$$

The spin forbidden channel (1.34c) occurs in the UV region above 300 nm as well as channel (1.34a) and (1.34b):

$$O_3 + h\nu \rightarrow O(^1D) + O_2(X^3\Sigma_g^-). \quad (1.34c)$$

Production of the $O(^1D)$ atoms above 310 nm has been attributed to both channel (1.34a) and via internally excited O_3 and spin-forbidden dissociation channel (1.34c) [18,19]. At around 200 nm, which corresponds to "stratospheric window" region, the two $O(^1S)$ production channels are energetically possible as listed in Table 1.1:

$$O_3 + h\nu \rightarrow O(^1S) + O_2(X^3\Sigma_g^-) \quad (1.34d)$$

$$\rightarrow O(^1S) + O_2(a^1\Delta_g). \quad (1.34e)$$

The de-excitation of $O(^1S)$ by N_2 and O_2 is very slow with the room temperature rate coefficients of $<5 \times 10^{-17}$ and 4.0×10^{-13} in units of cm^3 $molecule^{-1}$ s^{-1}, while that of $O(^1D)$ is very fast with the room temperature rate coefficients of 2.6×10^{-11} and 4.0×10^{-11} in units of cm^3 $molecule^{-1}$ s^{-1}. The reaction rates of $O(^1D)$ and $O(^1S)$ with H_2O do

not differ much from each other. Therefore, the formation of $O(^1S)$ from channels (1.34d and 1.34e) can be a source of OH radicals as shown in Fig. 1.6. In this thesis, the photolytic formation of $O(^1S)$ from the UV photolysis of O_3 around 200 nm and its subsequent reactions with small molecules relevant to middle and upper atmospheric chemistry have also been reported. Impact on HO_x formation in the stratosphere and mesosphere through $O(^1S) + H_2O$ reaction has been reported in Chapter 6.

1.4 Chemistry of NO in the upper atmosphere

Since Barth [20] discovered a large amount of NO in the upper atmosphere, the role of NO in the photochemistry and thermal budget of the lower thermosphere have been recognized. The escaping 5.3-μm NO radiation contributes significantly to cool the thermosphere [2]. The exothermic reactions involving odd nitrogen species are known as sources of thermospheric heating [2]. The downward flow of NO from the lower thermosphere to the upper stratosphere may cause significant loss of O_3, especially in the polar night regions [21]. Thermospheric NO has a peak concentration typically around 110 km. Satellite observations shows that the peak NO densities of $\sim 10^8$ molecules cm^{-3} at 105 ± 2.5 km in the latitude range 38°N-58°S [22].

The sources of thermospheric nitric oxide are the chemical reactions (1.35) and (1.36) as shown in Figure 1.7:

$$N(^2D) + O_2 \rightarrow NO + O \qquad (1.35)$$

$$N(^4S) + O_2 \rightarrow NO + O, \qquad (1.36)$$

while the recombination process,

$$N(^4S) + NO \rightarrow N_2 + O, \qquad (1.20)$$

is the main loss mechanism. Reaction (1.35) is thought to dominate the NO production in the lower thermosphere, while reaction (1.36), whose rate coefficient is very temperature dependent, becomes increasingly important at higher altitude where the temperature is larger. The contribution of reaction (1.36) to NO production was thought to be small because the reaction rate for (1.36) is small at the temperatures encountered in the lower thermosphere. Atmospheric models including the reaction (1.35) and (1.36) underestimate the observed NO density in the lower thermosphere around 105 km [22,23].

As an additional source, it has been suggested that suprathermal (or "fast" or "hot") $N(^4S)$ atom can react with O_2 to form NO in the thermosphere at an energy

depend rate, which is considerably faster than that at thermal equilibrium for gas temperature [24] (Fig. 1.7):

$$\text{fast } N(^4S) + O_2 \rightarrow NO + O. \quad (1.37)$$

The model calculations have extensively been performed to evaluate the translational energy distributions of $N(^4S)$ and the formation efficiency of NO through reaction (1.37) in the thermosphere [24,25,26,27,28].

In the thermosphere, nitrogen atoms, $N(^4S)$, $N(^2D)$, and $N(^2P)$, are produced by a series of photochemical processes involving the breaking of the N_2 bond [28,29]. The direct photodissociation by solar photons between 80 and 100 nm and by photoelectron impact provide major sources of nitrogen atoms:

$$N_2 + h\nu \rightarrow \text{fast } N(^4S) + N(^4S, {}^2D) \quad (1.38)$$

$$N_2 + e^* \rightarrow \text{fast } N(^4S) + N(^4S, {}^2D, {}^2P) + e. \quad (1.39)$$

The $N(^4S)$ atom carries excess energy and form a hot population in the thermosphere. Other reactions involving positive ions or metastable atoms also contribute to the production of suprathermal $N(^4S)$ atoms [28,29].

The suprathermal $N(^4S)$ atoms formed by these processes subsequently collide with ambient molecules (N_2 and O_2) in addition to reaction (1.37). The thermalization cross sections of $N(^4S)$ with ambient gases are crucial to evaluate the NO formation in the thermosphere. However, no laboratory study of the direct measurements for the thermalization cross section of suprathermal $N(^4S)$ atoms with ambient gases has been performed. In this thesis, the laboratory experiments about collisional relaxation processes of suprathermal $N(^4S)$ atoms have been described in Chapter 5.

1.5 $O(^1S)$ airglow in the upper atmosphere

In recent years, a great deal of aeronomic research has focused on airglow emissions, which are studied using ground-based, rocket and satellite techniques. The most frequently observed emission is the atomic $O(^1S)$ greenline emission at 557.7 nm. This emission particularly provides the information about the variability of solar activity and atomic oxygen concentration in the upper mesosphere and thermosphere.

The Barth mechanism is known to be the dominant excitation process of the nightglow emission peak around 100 km [30,31], that is,

$$O(^3P) + O(^3P) + M \rightarrow O_2^* + M \quad (1.40)$$

$$O_2^* + O(^3P) \rightarrow O_2(X^3\Sigma^-_g) + O(^1S), \quad (1.41)$$

where O_2^* is electronically excited state(s) of oxygen molecule. The production rate of $O(^1S)$ due to the Barth mechanism is proportional to the square of the density of atomic oxygen. Consequently, any change in the atomic oxygen concentration would directly affect the $O(^1S)$ 557.7-nm emission. Therefore, the nightglow observations have been used to investigate the transport processes of atomic oxygen in the lower thermosphere [32 and references therein].

Recently, the wind imaging interferometer (WINDII) on Upper Atmosphere Research Satellite (UARS) [33] has provided extensive data of dayglow emission throughout the 80 to 300 km altitude. The 557.7 nm dayglow emission shows two peaks in its emission rate, namely, one around 150-175 km and the other around 90-100 km. In the emission peak around 150-175 km, three important processes contribute to the production of this emission:

$$O_2^+ + e \rightarrow O(^1S) + O(^3P) \quad (1.42)$$

$$N_2(A^3\Sigma_u^+) + O(^3P) \rightarrow N_2 + O(^1S) \quad (1.43)$$

$$O(^3P) + e^* \rightarrow O(^1S) + e. \quad (1.44)$$

The model calculations show that the relative contributions to the production of $O(^1S)$ due to above sources change with altitude [34].

The production processes of $O(^1S)$ related to the emission peak around 90-100 km during daytime are shown in Figure 1.8. In this region, the three-body recombination process of atomic oxygen (Barth mechanism) is considered as the important process for $O(^1S)$ production. However, the WINDII data showed that the volume emission rate (VER) (number of photons emitted per units volume per second) of the green line emission was larger by a factor of three or more in the daytime than at night [35,36,37]. The observation indicates that further excitation processes should be involved in addition to the Barth mechanism. Shepherd and co-workers [35,36,37] have proposed that photodissociation of O_2 by the solar radiation between 100 and 130 nm, especially at Lyman-β (102.6 nm), is a primary source of $O(^1S)$ for the emission peak around 90-100 km in the daytime. In this thesis, the impact of the direct formation of $O(^1S)$ from the UV photolysis of O_3 on the greenline dayglow emission has been described in Chapter 6.

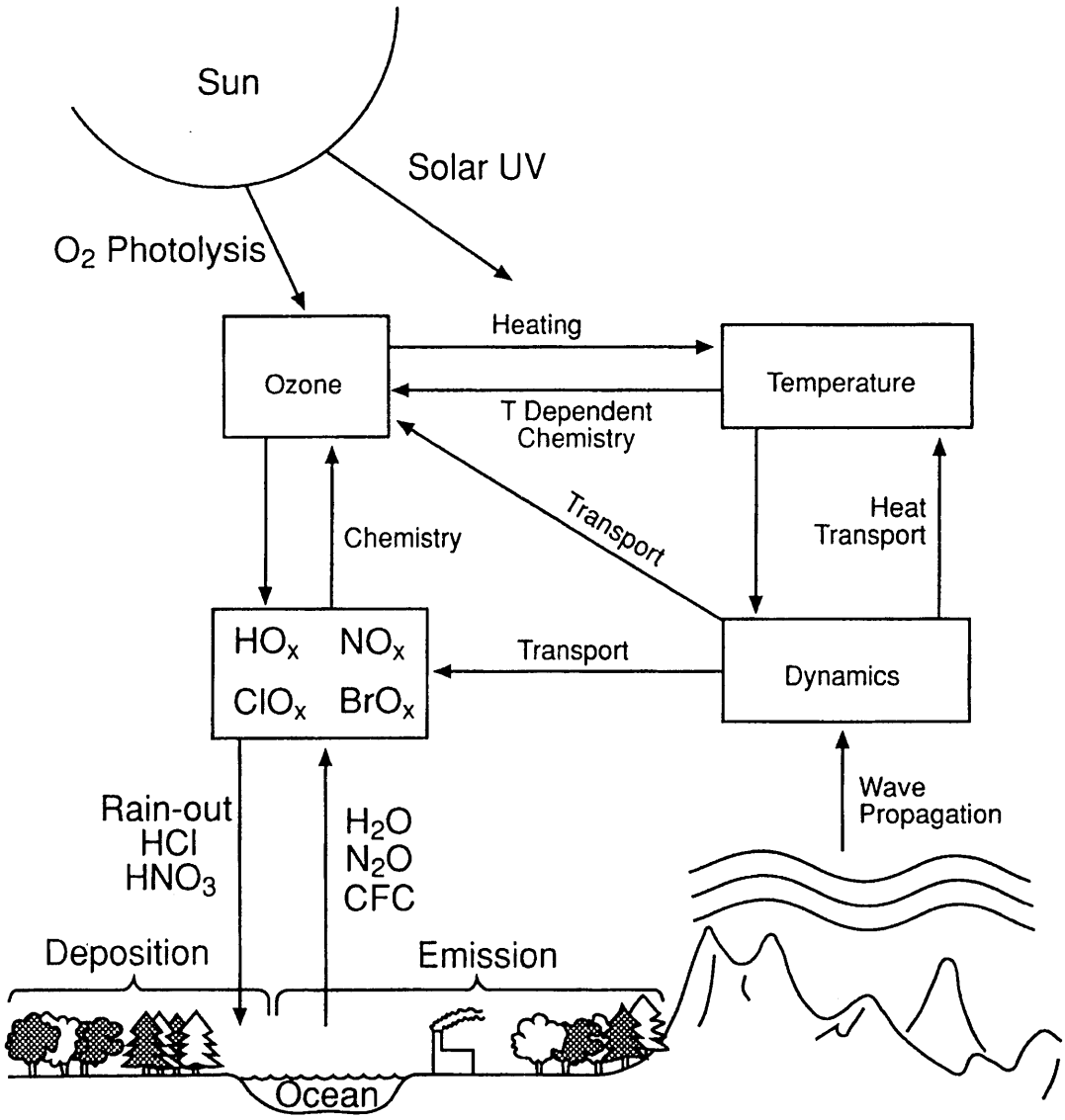

Figure 1.1. Representation of the couples chemical, radiative, and dynamical processes in the middle atmosphere [3].

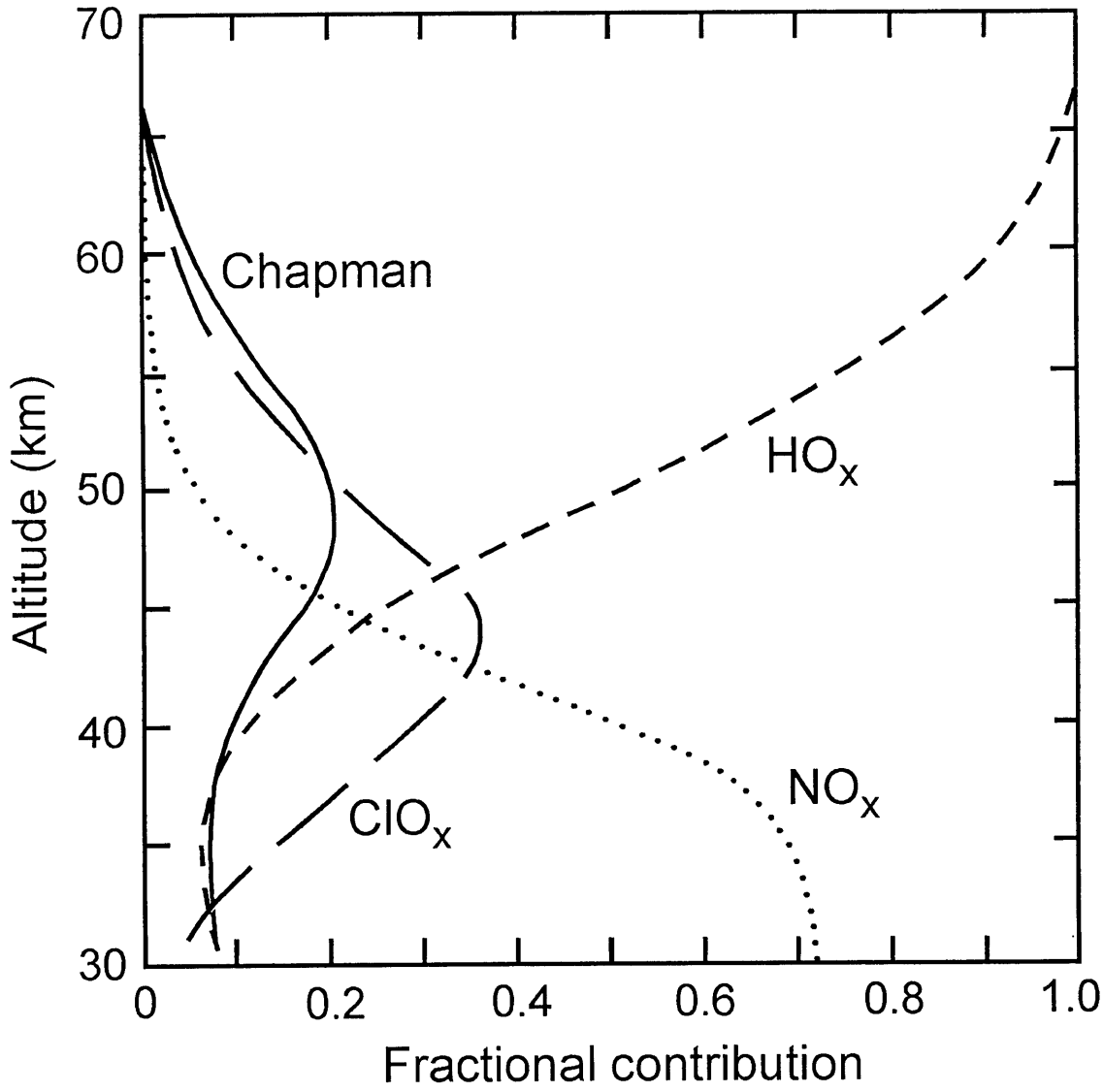

Figure 1.2. Fraction of the odd oxygen loss rate due to the Chapman mechanism and HO_x, NO_x, and ClO_x cycles (based on a mid-latitude diurnal average calculation) [1].

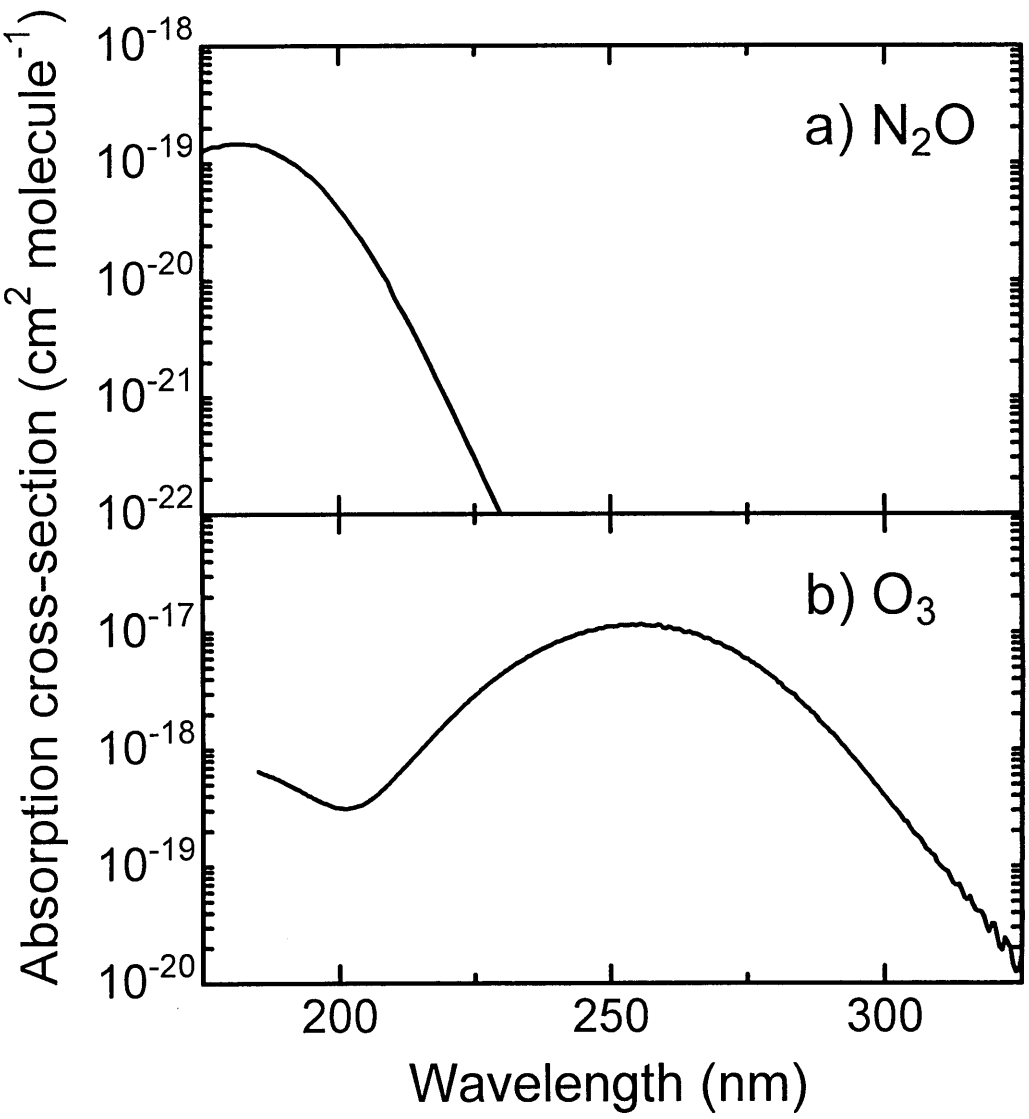

Figure 1.3. Absorption spectrum of a) N_2O and b) O_3 in the ultraviolet region at 298 K, in which the cross-section data of N_2O and O_3 were taken from Sander et al. [11] and Malicet [15], respectively.

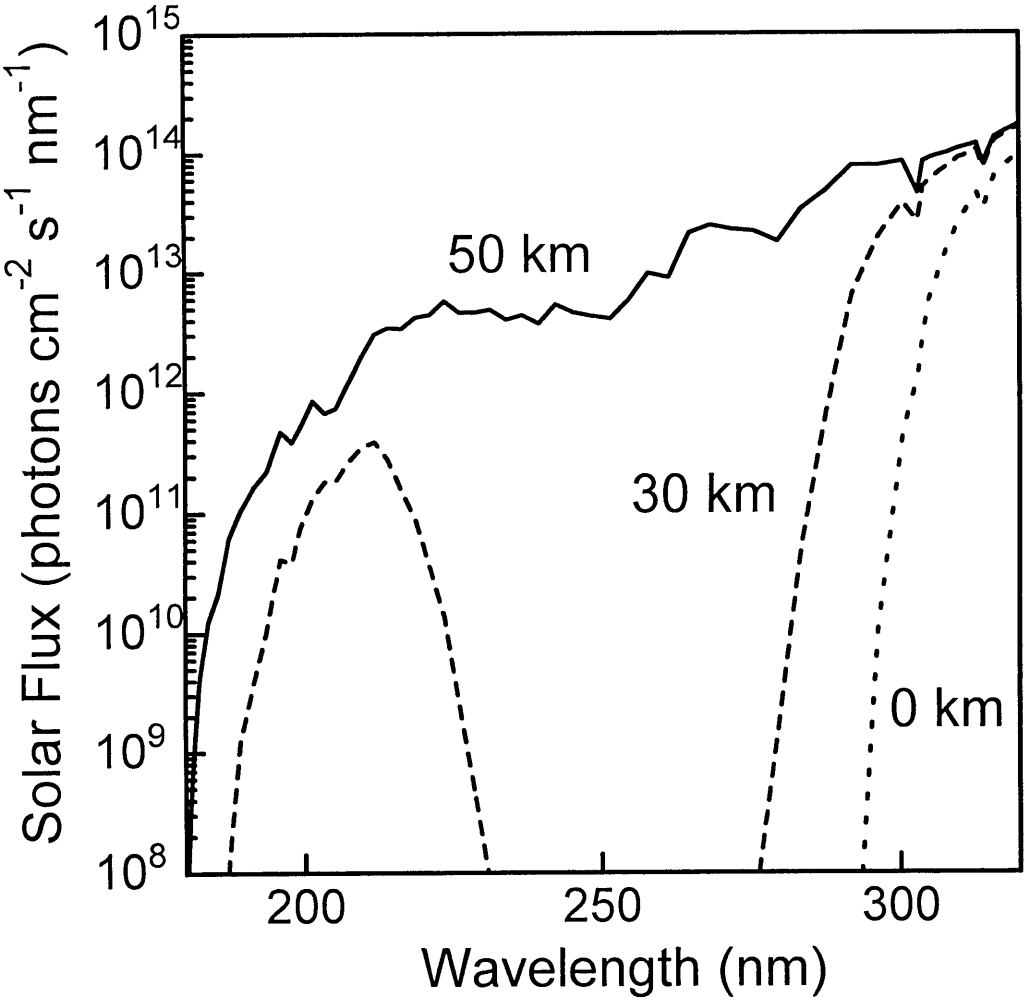

Figure 1.4. Solar photon fluxes at altitude of 50, 30, and 0 km, respectively above earth surfaces as a function of wavelength for US standard atmosphere at solar zenith angle (SZA) of 50°.

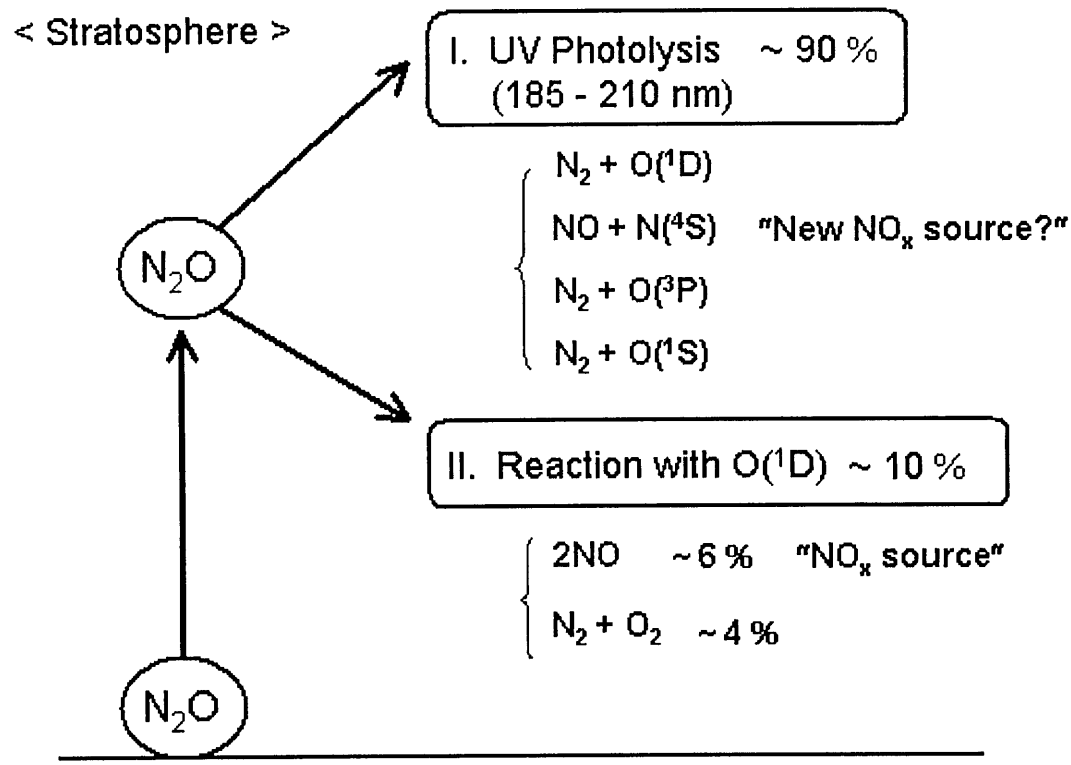

Figure 1.5. Schematics of the fate processes of N_2O in the stratosphere. The ratios of each sink are also presented.

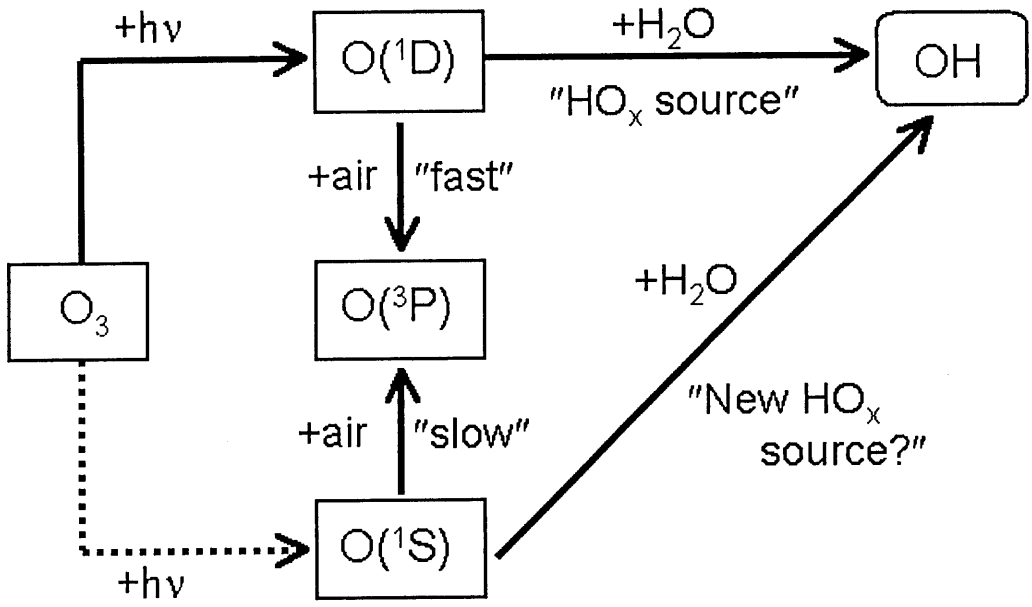

Figure 1.6. Schematics of the reaction pathways involving OH production in the middle atmosphere (see text).

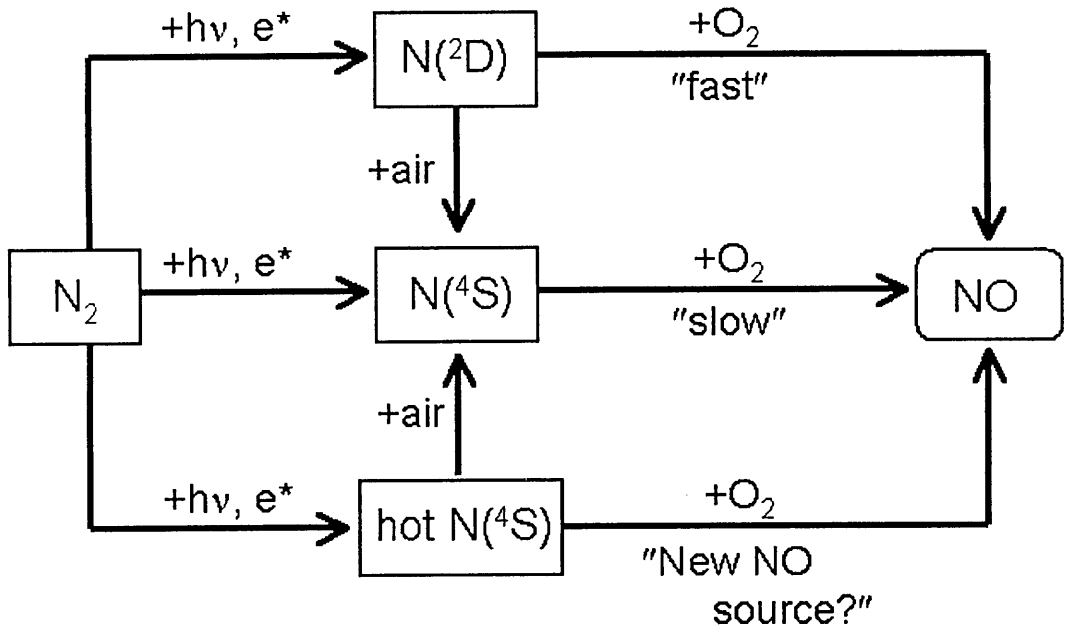

Figure 1.7. Schematics of the reaction pathways involving NO production in the lower thermosphere (see text).

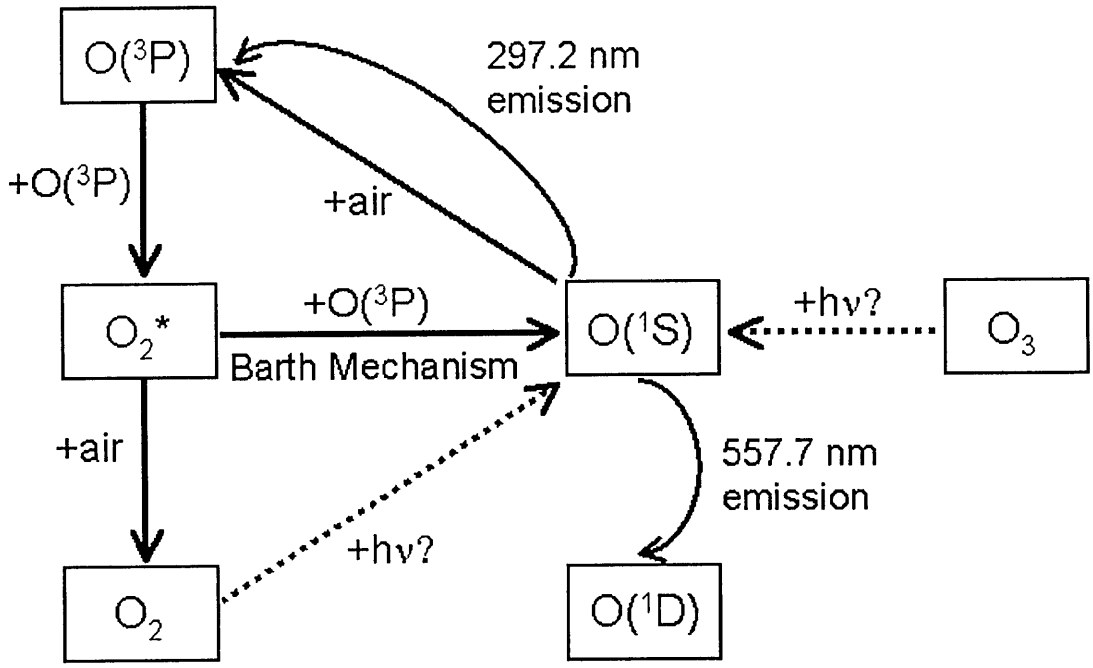

Figure 1.8. Schematics of the reaction pathways involving $O(^1S)$ production in the lower thermosphere (see text).

Table 1.1. Thermochemical threshold wavelengths for photodissociation pathways of O_3, in units of nm.

	$O_2(X^3\Sigma_g^-)$	$O_2(a^1\Delta_g)$	$O_2(b^1\Sigma_g^+)$	$O_2(A^3\Sigma_u^+)$	$O_2(B^3\Sigma_u^-)$	$2O(^3P)$
$O(^3P)$	1180	590	460	230	170	198
$O(^1D)$	410	310	260	167	150	
$O(^1S)$	234	196	179	129	108	

References for Chapter 1

[1] Wayne, R. P., *Chemistry of Atmospheres*, third edn., Oxford University Press, New York, 2000.

[2] Roble, R. G., Ridley, E. C., Dickinson, R. E., *J. Geophys. Res.*, **92**, 8745 (1987).

[3] Brasseur, G. P., Orlando, J .J., Tyndall, G. S., *Atmospheric Chemistry and Global Change*, Oxford University Press, New York, 1999.

[4] Chapman, S., *Mem. Roy. Meteorol. Soc.*, **3**, 103 (1930).

[5] Bate, D. R., Nicolet, M., *J. Geophys. Res.*, **55**, 301 (1950).

[6] Crutzen, P. J., *Q. J. R. Meteorol. Soc.*, **96**, 320 (1970).

[7] Johnston, H. S., *Science*, **173**, 517 (1971).

[8] Stolarski, R., Douglass, A. R., *J. Can. Chem.*, **52**, 1610 (1974).

[9] Molina, M. J., Rowland, F. S., *Nature*, **249**, 810 (1974).

[10] Rowland, F. S., Molina, M. J., *Rev. Geophys. Space Phys.*, **13**, 1 (1975).

[11] Sander, S. P., Friedl, R. R., Golden, D. M., Kurylo, M. J., Huie, R. E., Orkin, V. L., Moortgat, G. K., Ravishankara, A. R., Kolb, C. E.; Molina, M. J., Finlayson-Pitts, B. J., *Chemical Kinetics and Photochemical Data for use in Atmospheric Studies*, Evaluation No. 14, JPL Publication 02-25, 2003.

[12] Okabe, H., *Photochemistry of small molecules*, Wiley-Interscience, New York, 1978.

[13] Brasseur, G., Solomon, S., *Aeronomy of the middle atmosphere*, D. Reidel Publishing Company, Dordrecht, Holland, 1986.

[14] Conaway, R.R., Summers, M. E., Stevens, M. H., Cardon, J. G., Preusse, P., Offermann, D., *Geophys. Res. Lett.*, **27**, 2613 (2000).

[15] Malicet, J., Daumont, D., Charbonnier, J., Parisse, C., Chakir, A., Brion, J., *J. Atmos. Chem.* **1995**, *21*, 263.

[16] Atkinson, R., Baulch, D. L., Cox, R. A., Hampson Jr, R. F., Kerr, J. A., Rossi, M. J., Troe, J., *J. Phys. Chem. Ref. Data*, **27**, 1329 (1997).

[17] Matsumi, Y., Kawasaki, M., *Chem. Rev.*, **103**, 4767 (2003).

[18] Takahashi, K., Kashigami, M., Matsumi, Y., Kawasaki, M., OrrEwing, A., *J. Chem. Phys.*, **105**, 5290 (1996).

[19] Denzer, W., Hancock, G., Pinot de Moira, J. C., Tyley, P. L., *Chem. Phys.*, **231**,109 (1998).

[20] Barth, C. A., *J. Geophys. Res.*, **69**, 3301 (1964).

[21] Solomon, S., R. R Garcia, *Planet. Space. Sci.*, **32**, 399, (1984).

[22] Krishna Kumar, C., Swaminathan, P. K., Anderson, D. E., Yee, J. H., Gunson, M. R., Abrams, M. C., *J. Geophys. Res.*, **100**, 16,839 (1995).

[23] Suskind, D. E., Strickland, Meier, R. R., Tajeed, T., Fparvier, *J. Geophys. Res.*, **100**, 19,687 (1995).

[24] Solomon, S., *Planet. Space Sci.*, **31**, 135, (1983).

[25] Lie-Sevendsen, O., Rees, M., Stamnes, K, Whipple, E. C., *Planet. Space Sci.*, **39**, 929,

(1991).

[26] Gérard, J.C., Bisikalo, D. V., Shematovich, V. I., Duff, J. W., *J. Geophys. Res.*, **102**, 285, (1997).

[27] Swaminathan, P. K., Strobel, D. F., Kupperman, D. G., Krishna Kumar, C., Acton, L., DeMajistre, R., Yee, J. H., Paxton, L., Anderson, D. E., Strickland, D. J., Duff, J. W., *J. Geophys. Res.*, **103**, 11579 (1998).

[28] Balakrishnan, N., Sergueeva, E., Kharchenko, V., Dalgarno, A., *J. Geophys. Res.*, **105**, 18549 (2000).

[29] Schematovich, V. I., Bisikalo, D. V., Gérard, J. C., *Ann. Geophys.*, **10**, 792 (1992).

[30] Barth, C. A., *Ann. Phys.*, **5**, 329 (1964).

[31] McDade, I. C., Murtagh, D. P., Greer, R. G. H., Dickinson, P. H. G., Witt, G., Stegman, J., Llewellyn, E. J., Thomas, L., Jenkins, D. B., *Planet. Space Sci.* **34**, 789 (1986).

[32] Zhang, S. P., Roble, R. G., Shephered, G. G., *J. Geophys. Res.*, 106, 21,381 (2001).

[33] Shepherd, G. G., et al., *J. Geophys. Res.*, **98**, 10,725 (1993).

[34] Tyagi, S., Singh, V., *Ann. Geophys.*, **16**, 1599 (1998).

[35] Singh, V., McDade, I. C., Shepherd G. G., Solheim, B. H., Ward, W. E., *Ann. Geophysicae.*, **14**, 637 (1996).

[36] Shepherd, G. G., Siddiqi, N. J., Wiens, R. H., Zhang, S., *Adv. Space. Res.*, **20**, 2127 (1997).

[37] Sharma, R. M-., Shepherd, G. G., *J. Geophys. Res.*, **109**, A03303, doi:10.1029/2003JA010183 (2004).

Chapter 2

Experimental

2.1 Overview of the detection techniques of $N(^4S)$ and $O(^1S)$ atoms

2.1.1 Detection techniques of $N(^4S)$ atoms

There are three electronic states for the ground state configurations of N atom: $N(^4S_{3/2})$, $N(^2D_{5/2,\,3/2})$, and $N(^2P_{1/2,\,3/2})$ with their respective energies of 0, 2.38 and 3.58 eV. In the previous experimental studies, mass spectrometry technique [e.g. 1,2,3] and resonant fluorescence technique [e.g. 4,5,6] around 120 nm were used for detection of the electronic ground state $N(^4S)$ atoms. The experimental setup reported by Brunning and Clyne [3] is shown in Figure 2.1a. In their study, the $N(^4S)$ atoms generated in a microwave discharge of N_2 were monitored using a quadrupole mass spectrometer with a channel multiplier. The experimental setup reported by Anderson and co-workers [5,7] is shown in Figure 2.1b. In their study, the resonant fluorescence from the $N(2p^23s\ ^4P_{1/2,\,3/2,\,5/2} \rightarrow 2p^3\ ^4S_{2/3})$ transitions around 120 nm was detected using an atomic nitrogen lamp and a photomultiplier, in which, the $N(^4S)$ atoms were generated in a microwave discharge of N_2. The resonance absorption detections of $N(^4S)$ atoms at 119.9 nm with an atomic nitrogen lamp were also employed [8,9]. Recently, Adams et al. [10] demonstrated the two-photon LIF detection of $N(^4S)$ at 207 nm which is resonant to the two-photon $N(2p^23p\ ^4S_{3/2} \leftarrow 2p^3\ ^4S_{2/3})$ transition, in which the $N(^4S)$ atoms were produced by the photolysis of N_2O at 207 nm.

In this thesis, a new technique for high-sensitive detection technique of $N(^4S)$ using VUV- LIF spectroscopy at 120.07 nm which is resonant to the one-photon $N(2p^23s\ ^4P_{3/2} \leftarrow 2p^3\ ^4S_{2/3})$ transition has been developed.

2.1.2 Detection techniques of $O(^1S)$ atoms

There are three electronic states for the ground state configurations of O atom: $O(^3P_{0,\,1,\,2})$, $O(^1D_2)$, and $O(^1S_0)$ with their respective energies of 0-0.028, 1.97 and 4.19 eV. In contrast to the first electronic excited $O(^1D)$ atom [11,12], there is little information about the photochemical properties of $O(^1S)$ atom. One of the possible reasons for this situation is a difficulty to detect $O(^1S)$ atoms sensitively. In previous

laboratory studies on the photochemical reactions involving $O(^1S)$ atoms, detection of the visible emission at 557.7 nm corresponding to the ^1S - ^1D transition was used for monitoring $O(^1S)$ atoms [e.g. 13,14,15]. Due to the orbitally forbidden nature of the ^1S - ^1D transition, the sensitivity of the $O(^1S)$ emission detection method should be relatively low. The experimental setup reported by Young et al. [13,16] is shown in Figure 2.2. In their studies, the $O(^1S)$ atoms generated in the flush photolysis of N_2O at 147 nm (Xe lamp) were monitored using the $O(^1S \rightarrow {}^1D)$ emission at 557.7 nm.

In the present study, a new technique for high-sensitive detection technique of $O(^1S)$ using VUV- LIF spectroscopy at 121.76 nm which is resonant to the one-photon $O(2p^3 3s^1\ {}^1P_1 \leftarrow 2p^4\ {}^1S_0)$ transition has been developed. Thereby, photochemical reactions involving $O(^1S)$ atom have been examined.

2.2 VUV-LIF spectroscopy

2.2.1 Principle of LIF method

The LIF technique, first provided by Zare and co-workers [17], is a powerful tool for detection of trace amounts of atoms or molecules. The basic idea of LIF is as follows. Light from a tunable laser impinges on the sample to be investigated. As the frequency of the laser changes, atoms (molecules) within the irradiated portion of the sample will be exited to fluorescence whenever the spectral envelope of the laser overlaps an absorption line of the atom. The emission is detected by a photomultiplier, which "view" the excitation zone. The fluorescence intensity is recorded as a function of laser wavelength to produce what we call a fluorescence excitation spectrum. The intensities are then converted to relative populations of the various internal states, with the information of vibrational and rotational intensity factors.

In order for atom to be detectable by laser-induced fluorescence, there are three major requirement factors. First, the obvious one is that atom fluoresces. Moreover, it is preferable that the quantum yield for fluorescence process is unity so that the conversion of fluorescence intensities to populations is not complicated by other internal states. Second, the band system was spectroscopically analyzed so that quantum members could be assigned and intensity factors, such as line strength for the transition, could be obtained. Third, the atoms band system is accessible with available tunable laser light. Recent development of the techniques to generate tunable VUV laser light is helpful for this requirement.

2.2.2 Principle of VUV laser light generation

In the past few years, photochemical processes have been investigated in our laboratory using the coherent VUV radiation to detect atoms and radicals such as $H(^2S)$, $S(^1D)$, $S(^3P_j)$, $O(^1D)$, $O(^3P_j)$, $Cl(^2P_j)$, ClO, and CO [18,19,20]. The recent laser technology developed a new light source in the VUV wavelength region, which is tunable coherent radiation generated by frequency mixing in the gases and vapors. Since the earliest experiments by Ward and New [21], there has been much effort to develop new mixing schemes about third harmonic generation (THG) and two-photon resonant four-wave mixing process for extending the laser-based light range to the VUV and even to the near X-ray region. The four-wave mixing is classified into two categories, namely four-wave sum frequency mixing (SFM) and four-wave different frequency mixing (DFM). The wavenumbers of the generated VUV light (ω_{VUV}) for the SFM and DFM can be written in following form:

$$\omega_{VUV} = 2\omega_1 \pm \omega_2, \tag{2.1}$$

where ω_1 is the wavenumber of the first laser light (ω_1 laser), which tuned to the two-photon resonance level of the non-linear medium, and ω_2 is that of the second tunable laser light (ω_2 laser), whose variations are capable of obtaining frequency tunability in ω_{VUV}. While keeping the resonance condition by tuning the wavenumber of the ω_1 laser light, varying the wavenumber of the ω_2 laser light makes it possible to generate the frequency tunable VUV light. Theoretically, the generated power of VUV radiation, P_{VUV}, for the four-wave mixing is given by

$$P_{vuv} \propto N^2 \chi_{(3)}^2 P_1^2 P_2 F(b_1 \Delta k, b) \ , \tag{2.2}$$

where P_1 and P_2 are the input powers of ω_1 and ω_2 lasers, N is the atomic density of non-linear conversion medium, $\chi_{(3)}$ is the third order non-linear susceptibility per atom. F is the phase matching factor depending on $b_1\Delta k$ and $b = b_1/b_2$. Here, b_1 and b_2 are the confocal parameters of the laser beams, and Δk is the wave vector mismatch between the generated radiation and driving polarization [22]:

$$\Delta k = k_{vuv} - (2k_1 \pm k_2). \tag{2.3}$$

THG and four-wave mixing in inert gases (for example, Xe, Kr, Ar) have been well studied using a gas cell or supersonic rate gas jet for broadly tunable VUV radiation in the wavelength range (λ = 110 - 200 nm) [23,24,25]. In addition, metallic

vapors (for example, Sr [26], Mg [27], Zn [28], Hg [29,30]) are good candidates for generating VUV and near X-ray lights. In this thesis, the SFM in the Hg vapor and the DFM in the Kr gas were used to generate VUV light around 120.1 and 121.8 nm, respectively.

2.2.3 Principle of the Doppler profile measurement

The Doppler profile measurements of the photofragments have been widely used to investigate chemical reactions and photodissociation processes [e.g. 31,32]. Analysis of the Doppler profile provides the information about the kinetic energy of atoms. The shift in frequency of radiation ($\Delta\nu$) emitted by an atom moving with velocity (v) at angle $\theta = 0$ between the direction of the motion of atoms and line of sight of the observer is given by

$$\Delta\nu = \frac{\nu_0}{1+\nu/c}, \tag{2.4}$$

where c is the velocity of light, ν_0 is resonance center frequency of atomic transition. The frequency shifts of atoms away from line center of the excitation transition of the LIF process depend on the velocity components of atoms along the propagation direction of the probe laser [33]. The thermal Doppler shapes follow a Boltzman distribution of velocities. The Doppler shift ($\Delta\nu_T$) for given temperature (T) can be calculated by

$$\Delta\nu_T = \frac{2\nu_0}{c}\left(\frac{2k_BT}{m}\ln 2\right)^{1/2}, \tag{2.5}$$

where k_B is the Boltzman constant, m is the mass of the atom.

The observed Doppler profile is also broadened by the VUV probe laser line width. Assuming the Gaussian shape for probe laser, the VUV probe laser line width ($\Delta\nu_{laser}$) can be estimate from the observed Doppler shift ($\Delta\nu_{obs}$) of the thermalized atoms:

$$(\Delta\nu_{obs})^2 = (\Delta\nu_T)^2 + (\Delta\nu_{laser})^2. \tag{2.6}$$

2.3 Experimental setup

In the present study, the formation of $N(^4S)$ in the photolysis of N_2O, NO, and NO_2 at 193 nm and the reactions kinetics involving $N(^4S)$ have been investigated using

VUV-LIF detection technique of $N(^4S)$ atoms. The formation of $O(^1S)$ in the photolysis of O_3 at 193, 215, and 220 nm and reaction kinetics involving $O(^1S)$ have also been investigated using VUV-LIF detection technique of $O(^1S)$ atoms. Figure 2.3 and 2.4 show schematic diagrams of our experimental arrangements for detecting $N(^4S)$ and $O(^1S)$, respectively. The experimental arrangements include a reaction chamber, gas inlet system, photolysis and probe laser system, and a data acquisition system. The microwave (MW) discharge and titration system are also depicted in Fig. 2.3.

2.3.1 Reaction chamber and flow system

The reaction chamber was made of stainless steel with the size 80 × 80 × 80 mm, and was continuously evacuated by a rotary pump (Alcatel model 2021, 330 Liter / min.) through a liquid N_2 trap. The total gas pressure in the reaction chamber was measured by a capacitance manometer (MKS, Baratoron 122AA). Sample gases were supplied into the chamber through poly-tetrafluoroethylene tubing. The flow rates of sample gases were regulated by needle valves or mass flow controllers (MFC) (STEC, SEC-400MK3).

2.3.2 Photolysis lasers

The photolysis radiation at 193 nm was obtained from an ArF excimer laser (Lambda Physik, COMPex 102). The tunable photolysis radiation between 215 and 220 nm was obtained by an Nd:YAG laser pumped optical parametric oscillator (OPO) laser (Continuum, Powerlite 8010 and Panther OPO) and a subsequent frequency doubling in a β-BaB_2O_4 (BBO) crystal. The OPO laser wavelength was calibrated by introducing a part of the OPO signal light into a wavemeter (Burleigh, WA-4500). Dichroic mirrors were used to separate the fundamental and UV outputs. Typical pulse energies of the UV photolysis radiation were 10, 0.7, and 1.0 mJ at 193, 215, and 220 nm, respectively.

2.3.3 Tunable VUV laser for detection of $N(^4S)$ atoms

For detection of $N(^4S)$ atoms by the VUV-LIF method, the atomic line of the $N(2p^23s\ ^4P_{1/2} \leftarrow 2p^3\ ^4S_{2/3})$ transition at 120.07 nm was used. The probe VUV laser radiation was generated by two-photon resonant four-wave sum frequency mixing ($\omega_{VUV} = 2\omega_1 + \omega_2$) in Hg vapor [29]. Energy level diagram of the relevant atomic levels of Hg was shown in Figure 2.5a. Two dye lasers (Lambda Physik, Scanmate 2E

and FL3002E) were simultaneously pumped by a single XeCl excimer laser (Lambda Physik, COMPex 201). One dye laser operating with Rhodamin 101 dye in MeOH solvent generated 4 – 5 mJ/pulse around 625 nm. The visible output was frequency-doubled in a KH_2PO_4 (KD^*P) crystal to obtain 312.76 nm which is two-photon resonant with Hg electronic transition ($6s7s\ ^1S_0 \leftarrow 6s^2\ ^1S_0$). The output of other dye laser operating with Coumarin 307 dye in MeOH solvent produced 2 – 4 mJ pulse^{-1} around 517 nm. The two laser beams were carefully overlapped using a dichroic mirror and focused into the Hg vapor cell with a fused silica lens (f = 250 mm). The Rydberg transitions of $Hg(6s^1 15p^1\ ^1P_1 \leftarrow 6s^2\ ^1S_0)$ and $Hg(6s^1 15p^1\ ^3P_1 \leftarrow 6s^2\ ^1S_0)$ were used for the generation of the VUV radiation around 120.1 nm.

Figure 2.5b shows a schematic diagram of the Hg vapor cell used in this study to generate VUV laser light around 120.1 nm. A thin LIF window was used to separate the Hg vapor cell and reaction chamber. In order to prevent the deposition of Hg vapor on the windows, water flows were prepared between a heater and windows. The temperature in the Hg vapor cell was controlled around 450 – 470 K to obtain enough VUV probe laser power for experiments, which corresponds to the equilibrium Hg vapor pressure of 8 – 14 Torr [34]. Kr was added in the Hg vapor cell for phase matching and the optimum partial pressure was 6 – 8 Torr. Experimentally, Kr was added into the Hg cell prior to heating and sometimes refilled after cooling the cell down. The generated VUV laser light was introduced into a reaction chamber through a LiF window. A fraction of the incident VUV light passed through the reaction chamber was reflected by a thin LiF plate held in the end of the reaction chamber and led into a NO photoionization cell. The relative intensity of VUV laser light was monitored by measuring the photoionization current. Typical NO gas pressure was 2 – 3 Torr. The VUV laser line width was estimated to be 0.40 cm^{-1} full-width-at-half-maximum (FWHM) with a Gaussian shape, which was estimated from the Doppler profile of thermalized $N(^4S)$ atoms produced from 193-nm laser irradiation of NO_2 in the presence of 3.6 Torr of helium at a delay time of 5 μs between the photolysis and probe laser pulses. The $N(^4S)$ detection limit of the VUV-LIF system was estimated to be 2×10^9 atoms cm^{-3}.

2.3.4 Tunable VUV laser for detection of $O(^1S)$ atoms

For detection of $O(^1S)$ atoms by VUV-LIF method, the atomic line of the

$O(2p^3 3s^1\ ^1P_1 \leftarrow 2p^4\ ^1S_0)$ transition at 121.76 nm was used. The probe VUV laser radiation was generated by two-photon resonant four-wave difference frequency mixing ($\omega_{VUV} = 2\omega_1 - \omega_2$) in a gas mixture of Kr/Ar [25]. Energy level diagram of relevant atomic levels of Kr was shown in Figure 2.6a. Two dye lasers (Lambda Physik, Scanmate 2E and FL3002E) were simultaneously pumped by a single XeCl excimer laser (Lambda Physik, COMPex 201). The output from one dye laser operating with Bis-MSB dye in 1,4-dioxane solution was frequency-doubled by a BBO crystal to generate UV laser at 212.56 nm, which was two-photon resonant with Kr $5p[1/2]_0$. The output from the other dye laser operating with Styryl-9M dye in DMSO solution was around 840 nm. The typical pulse energies were 0.4 and 4 mJ for the UV and near-IR laser pulses, respectively. The laser beams were carefully overlapped using a dichroic mirror and focused into the Kr/Ar containing cell with a fused silica lens (f = 200 mm).

Figure 2.6b shows a schematic diagram of the frequency conversion cell including Kr/Ar gas mixture to generate VUV laser light. A thin LIF window was used to separate the cell and reaction chamber. Ar was added for phase matching and the optimum partial pressures of Kr and Ar were 15 – 20 and 100 – 120 Torr, respectively. The VUV laser line width was estimated to be 0.48 cm^{-1} (FWHM) with a Gaussian shape, which was estimated from the Doppler profile of thermalized $O(^1S)$ atoms produced from 193-nm laser irradiation of O_3 in the presence of 2 Torr of helium at a delay time of 3 μs between the photolysis and probe laser pulses. The $O(^1S)$ detection limit of the VUV-LIF system was estimated to be 3×10^8 atoms cm^{-3}.

2.3.5 Detection system and data acquisition

The repetition rate of the photolysis and probe laser system was 10 Hz. The time delay between the photolysis and probe laser pulses was controlled by a digital delay generator (Stanford Research Systems, DG535), and checked on the oscilloscope using two fast-response Silicon-photodiode detectors (Hamamatsu Photonics, S1722-02). The jitter of the delay time was less than 10 ns. The VUV-LIF signals from $N(^4S)$ and $O(^1S)$ atoms were detected using a solar-blind photomultiplier tube (PMT) (EMR, 542J-09-17), which had an MgF_2 window and KBr photo-cathode that was sensitive only between 118 and 150 nm. A band pass filter (Acton Research, model 122-VN, λ = 122 nm, $\Delta\lambda$ = 12 nm) was installed. The observation direction of the LIF was perpendicular to both VUV probe and photolysis laser light, and perpendicular to the electric vector of the VUV

probe laser. The output of the photomultiplier was pre-amplified and averaged over 10 laser pulses by a gated integrator (Stanford Research Systems, SR-250), and then stored on a personal computer. The output from the NO ionization cell was also pre-amplified and averaged over 10 laser pulses by another gated-integrator, and stored on the personal computer.

(a)

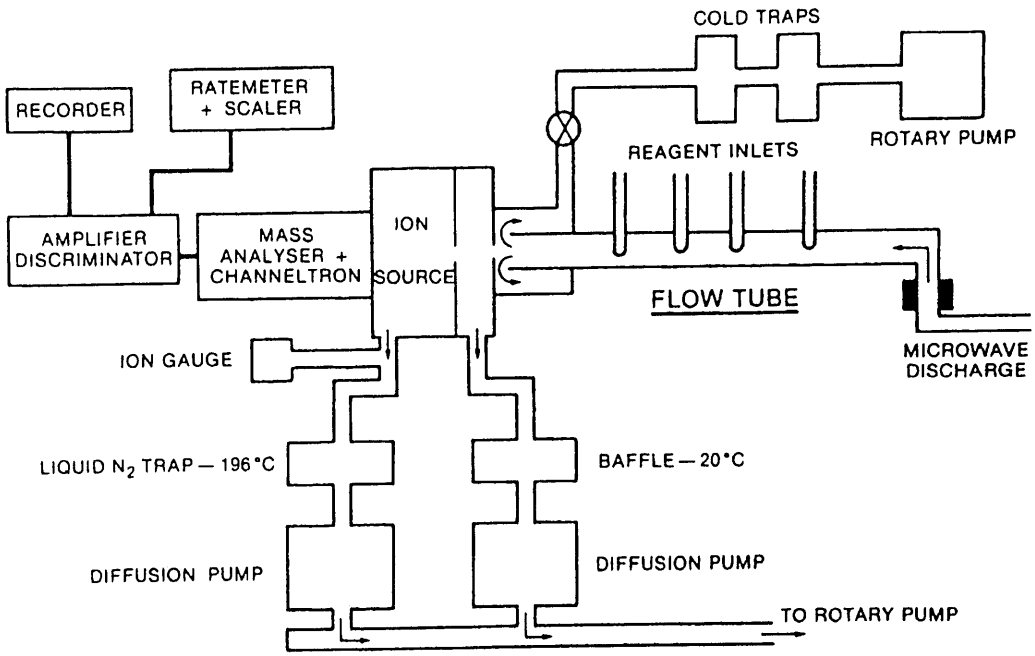

(b)

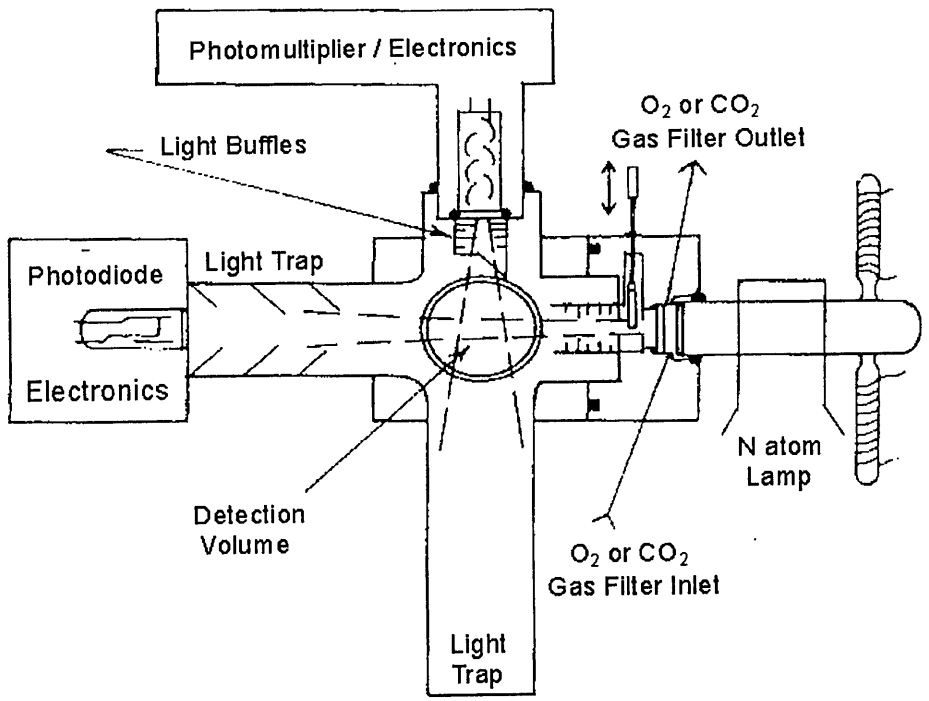

Figure 2.1. Schematic diagrams of the N(^{4}S) detection system using (a) the mass spectrometry [3] and (b) the resonant fluorescence technique [5,7].

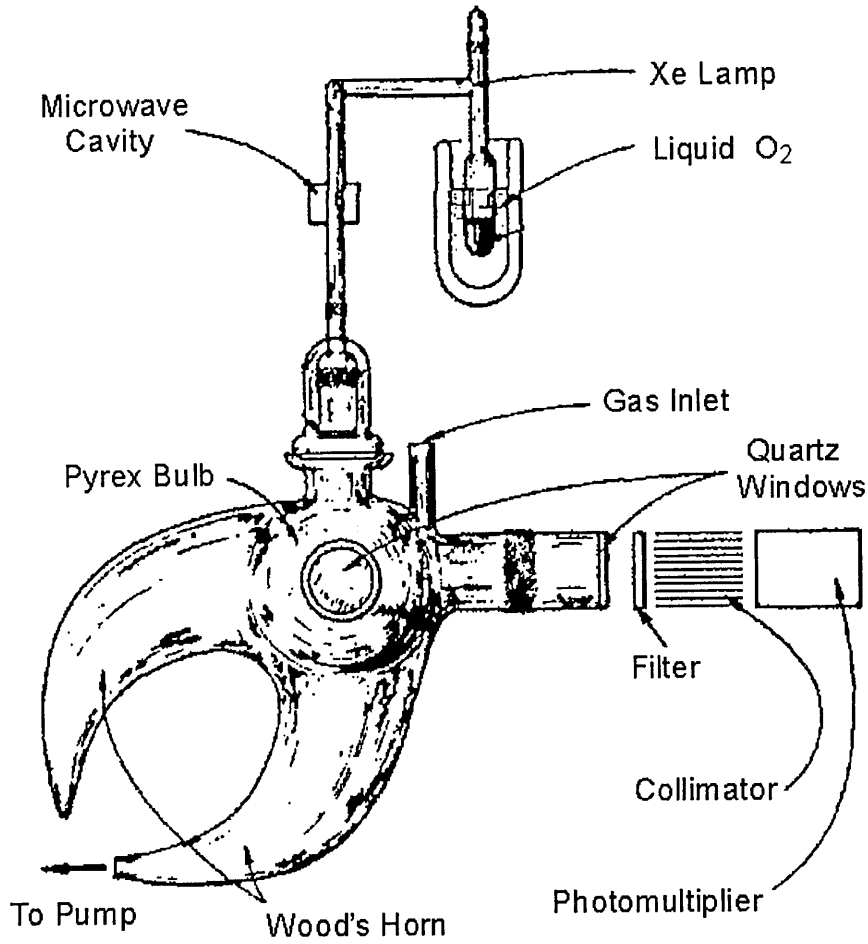

Figure 2.2. Schematic diagram of the $O(^1S)$ detection system using a $O(^1S \rightarrow {}^1D)$ emission at 557.7 nm [13,16].

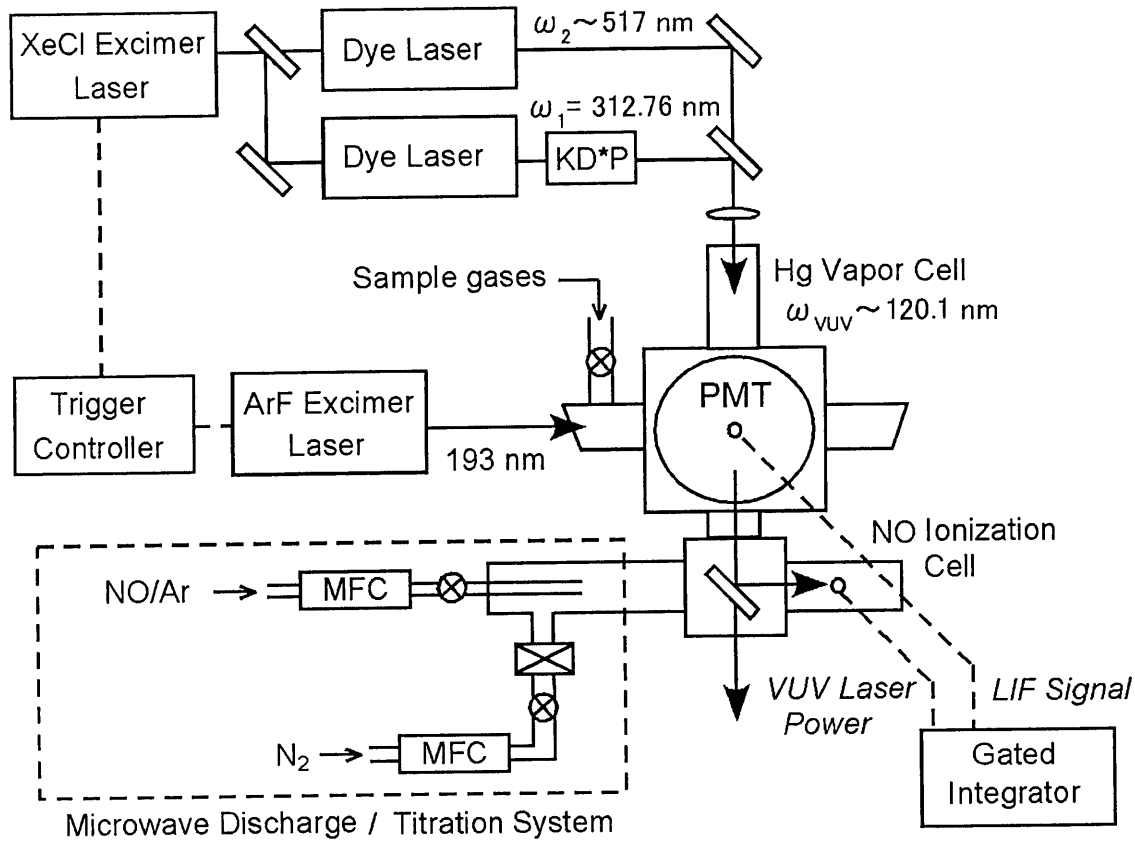

Figure 2.3. Schematic diagram of our experimental apparatus for detecting $N(^4S)$ atoms with the VUV-LIF technique. MFC, mass flow controller; PMT, photomultiplier tube; KD^*P, KH_2PO_4 crystal.

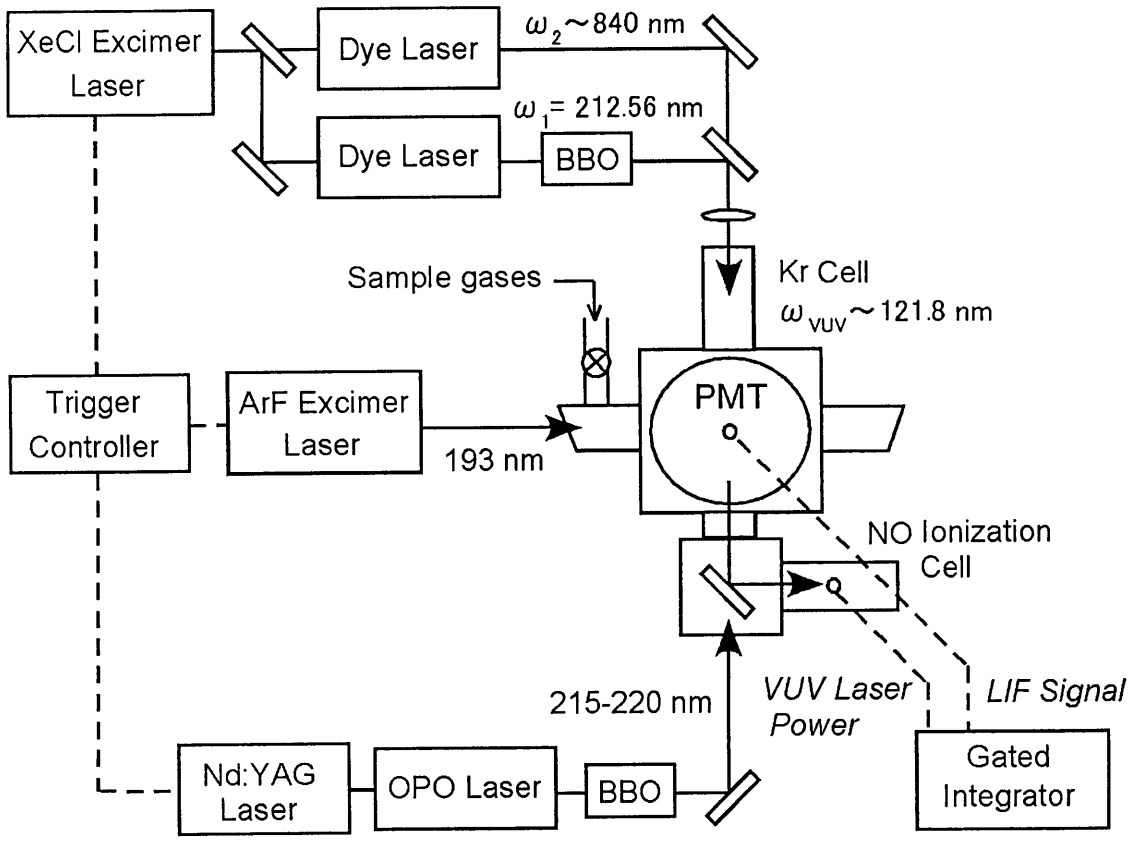

Figure 2.4. Schematic diagram of our experimental apparatus for detecting $O(^1S)$ atoms with the VUV-LIF technique. OPO, optical parametric oscillator; PMT, photomultiplier tube; BBO, β-BaB_2O_4 crystal.

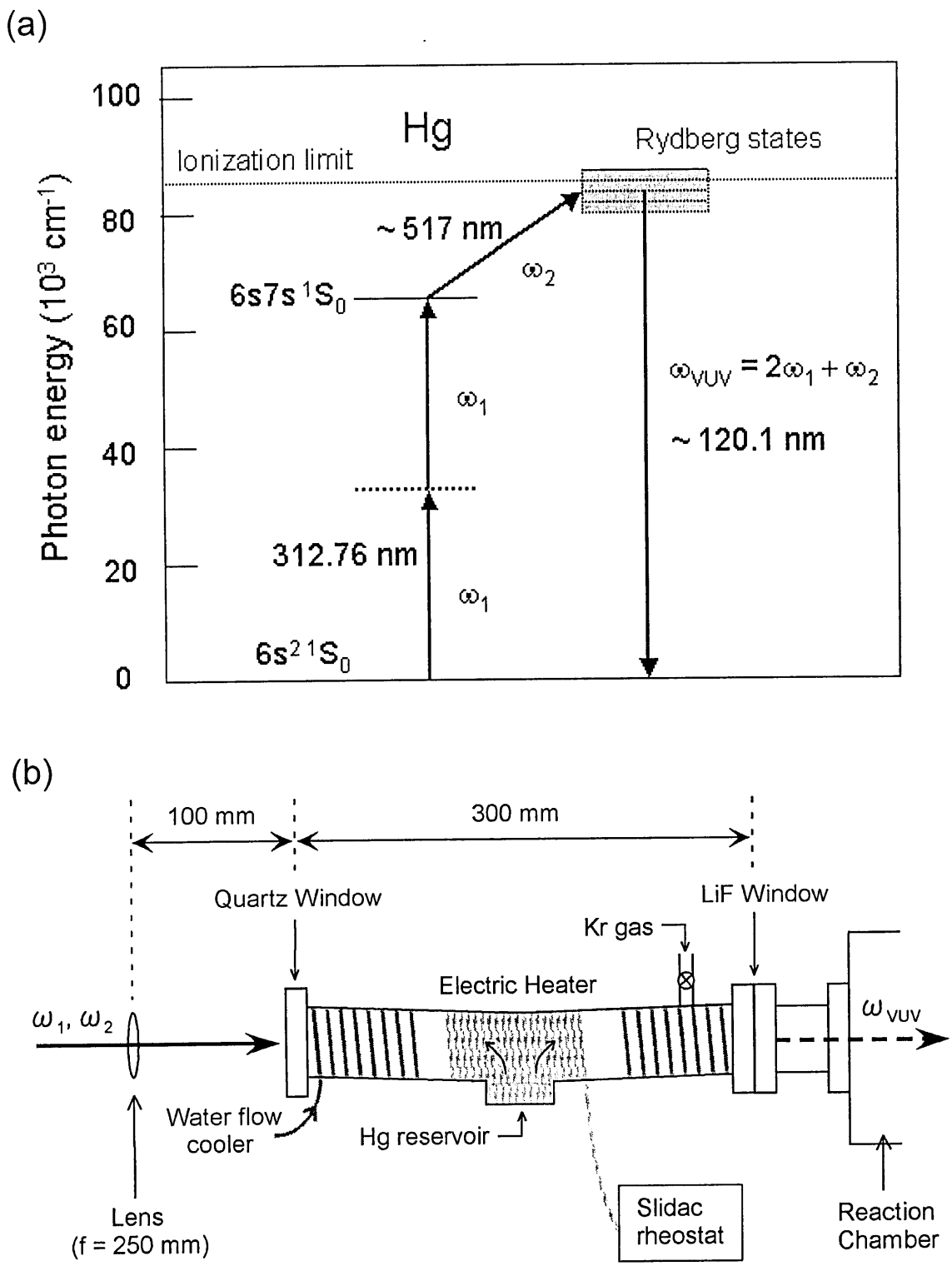

Figure 2.5. The generation scheme of VUV laser radiation by two-photon resonant four-wave sum frequency mixing in Hg vapor. (a) Energy level diagram of the relevant atomic levels in Hg for VUV generation around 120.1 nm. (b) Schematic diagram of Hg vapor cell (see text).

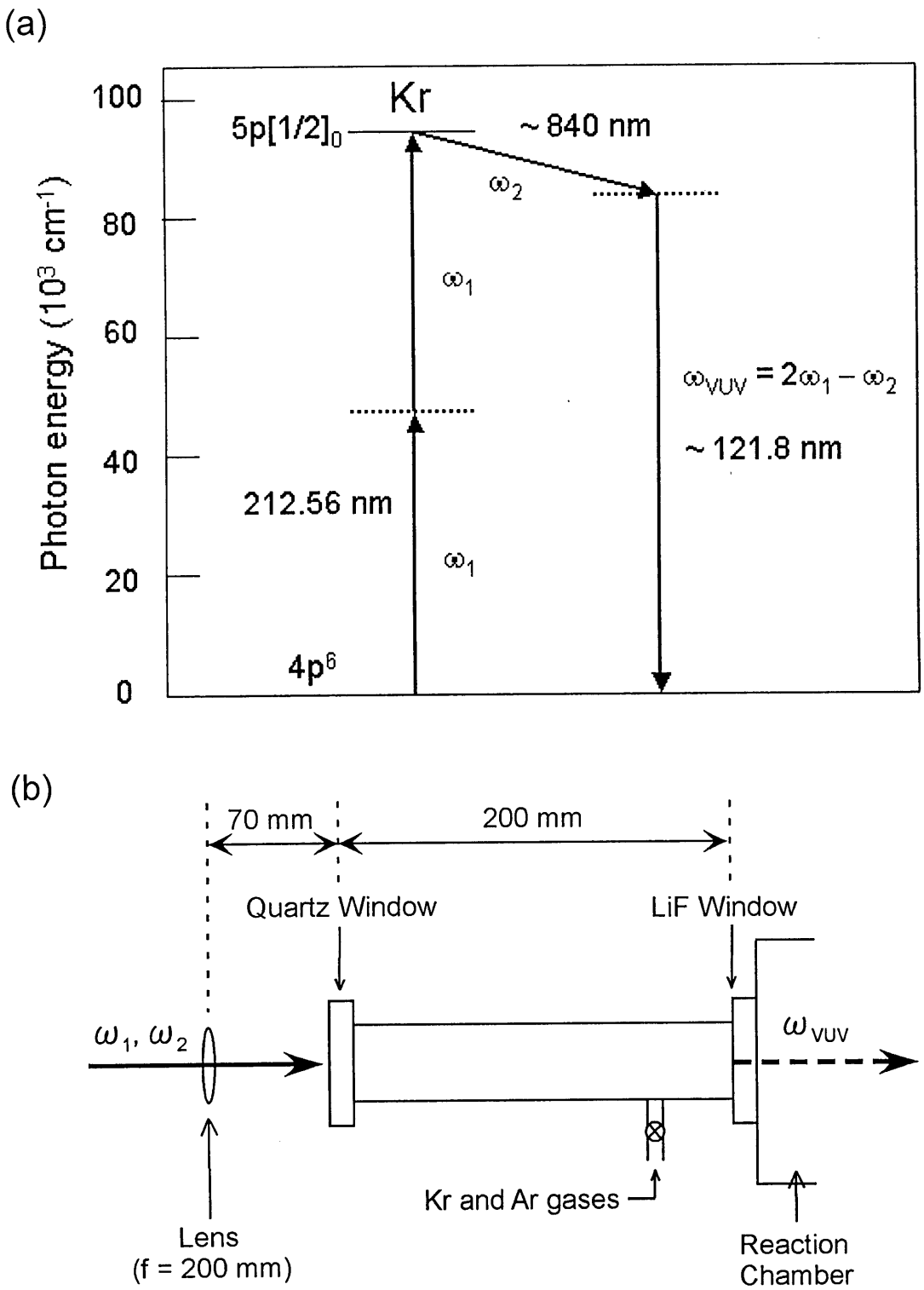

Figure 2.6. The generation scheme of VUV laser radiation by two-photon resonant four-wave different frequency mixing in a gas mixture of Kr/Ar. (a) Energy level diagram of the relevant atomic levels in Kr for VUV generation around 121.8 nm. (b) Schematic diagram of Kr cell (see text).

References for Chapter 2

[1] Phillips L. F., Schiff, H. I., *J. Chem. Phys.*, 36, 1509 (1962).

[2] Clyne, M. A. A., McDermid, I. S., *J. Chem. Soc. Faraday. Trans. 1*, **71**, 2189 (1975).

[3] Brunning, J., Clyne, M. A. A., *J. Chem. Soc. Faraday. Trans. 2*, **80**, 1001 (1984).

[4] Husain, D., Slater, N. K. H., *J. Chem. Soc. Faraday II*, **76**, 606 (1980).

[5] Wennberg, P. O., Anderson, J. G., Weisenstein, D. K., *J. Geophys. Res.*, **99**, 18839 (1994).

[6] Fernandez, A., Goumri, A., Fontijn, A., *J. Phys. Chem.*, **A102**, 168 (1998).

[7] Brune, W. H., Schwab, J. J., Anderson, J. G., *J. Phys. Chem.*, **87**, 4503 (1983).

[8] Davidson, D. F.; Hanson, R. K. *Int. J. Chem. Kinet.*, 22, 843 (1990).

[9] Koshi, M., Yoshimura, M., Fukuda, K., Matsui, H., Saito, K., Watanabe, M., Imamura, A., Chen, C., *J. Chem. Phys.*, **93**, 8703 (1990).

[10] Adams, S. F., DeJoseph Jr. C. A., Carter , C. C., Miller , T. A., Williamson, J. M., *J. Phys. Chem.*, **A105**, 5977 (2001).

[11] Okabe, H. *Photochemistry of small molecules*, Wiley-Interscience, New York, 1978.

[12] Sander, S. P., Friedl, R. R., Golden, D. M., Kurylo, M. J., Huie, R. E., Orkin, V. L., Moortgat, G. K., Ravishankara, A. R., Kolb, C. E., Molina, M. J., Finlayson-Pitts, B. J., *Chemical Kinetics and Photochemical Data for use in Atmospheric Studies*, Evaluation No. 14, JPL Publication 02-25, 2003.

[13] Young, R. A., Black, G., Slanger T. G., *J. Chem. Phys.*, **50**, 309 (1969).

[14] Rindley, B. A., Atkinson, R. A., Welge, K. H., *J. Chem. Phys.*, **58**, 3878 (1973).

[15] Capetanakis, F. P., Sondermann, F., Hoser, S., Stuhl, F., *J. Chem. Phys.*, **98,** 7883 (1993).

[16] Young, R. A., Black, G., Slanger T. G., *J. Chem. Phys.*, **50**, 303 (1969).

[17] Zare, R. N., Dagdian, P. J., *Science*, **185**, 739 (1974).

[18] Matsumi, Y., *Journal of the Spectroscopical Society of Japan*, **45**, 209 (1997).

[19] Takahashi, K., Takeuchi, Y., Matsumi, Y., *Chem. Phys. Lett.*, **410**, 196 (2005).

[20] Taketani, F., Takahashi, K., Matsumi, Y., Wallington, T. J., *J. Phys. Chem.*, **A105**, 3935 (2005).

[21] Ward, J. F., New, G. H. C., *Phys. Rev.*, **185**, 57 (1969).

[22] Hilber, G., Brink, D. J., Lago, A., Wallenstein, R., *Phys. Rev. A*, **38**, 6231 (1988).

[23] Hiber, G., Lago, A., Wallenstein, R., *J. Opt. Soc. Am. B*, **4**, 1753 (1987).

[24] Agullion, F., Lebehot, A., Rousseau, J., Campargue, R., *J. Chem. Phys.*, **86**, 5246 (1987).

[25] Marangos, J. P., Shen, N, Ma, H, Hutchinson, M. H. R., Connerade, J. P., *J. Opt. Soc. Am. B*, 7, 1254 (1990).

[26] Scheinberger, H., Puell, H., Vidal, R.C., *Phys. Rev. A*, **18**, 2585 (1987).

[27] Zkao, L., Nie, Y., Zhang, J., Li., Q., Yang, J., *Opt. Comm.*, **58**, 281 (1986).

[28] Janroz, W., La Rocque, P. E., Stoicheff, B. P., *Opt. Lett.*, 7, 617 (1982).

[29] Hibring, R., A., Wallenstein, R., *IEEE J. Quantum Electron.*, **QE-19**, 1759 (1983).

[30] Tomkins, F. C., Mahon, R., *Opt. Lett.*, 7, 304 (1982).

[31] Houston, P. L., *J. Phys. Chem.*, **91**, 5388 (1987).

[32] Matsumi, Y., Das, P. K., Kawasaki, M., *J. Chem. Phys.*, **92**, 1696 (1990).

[33] Zare, R. N., Herschback, D. R., *Proc. IEEE*, **51**, 173 (1963).

[34] Smith, A. V., Alford, W. J., *J. Opt. Soc. Am. B*, **4**, 1765 (1987).

Chapter 3

$N(^4S)$ formation in the UV photolysis of N_2O and its implications for stratospheric ozone chemistry

3.1 Introduction

N_2O is an important atmospheric minor constituent as the main source of NO_x in the stratosphere, since the NO_x species play a significant role in the middle atmospheric chemistry. Most of the N_2O transported through the planetary boundary layer and the free troposphere to the stratosphere is photolyzed at UV wavelengths to $O(^1D) + N_2$, while a small fraction of N_2O reacts with $O(^1D)$ atoms:

$$N_2O + h\nu \rightarrow N_2 + O(^1D) \qquad (\lambda < 341 \text{ nm}), \qquad (3.1a)$$

$$N_2O + O(^1D) \rightarrow 2NO \qquad (3.2a)$$

$$\rightarrow N_2 + O_2. \qquad (3.2b)$$

The N_2O photolysis around 200 nm is considered to proceed through channel (3.1a) with an almost unity quantum yield [1] and the other energetically available channels are very minor:

$$N_2O + h\nu \rightarrow N(^4S) + NO(X^2\Pi) \qquad (\lambda < 248 \text{ nm}) \qquad (3.1b)$$

$$\rightarrow N_2 + O(^3P) \qquad (\lambda < 742 \text{ nm}) \qquad (3.1c)$$

$$\rightarrow N_2 + O(^1S) \qquad (\lambda < 211 \text{ nm}). \qquad (3.1d)$$

Felder et al. [2] studied the dissociation dynamics of N_2O at 193 nm by photofragments translational spectroscopy and reported that channel (3.1b) was unimportant as the time-of-flight signal intensity at m/e = 30 was less than the detection limit. Greenblatt and Ravishankara [3] reported the upper limit value of the quantum yield for channel (3.1b) in the 193 nm photolysis of N_2O to be 8×10^{-3} through the chemiluminescent detection of NO products. Recently, Adams et al. [4] detected the $N(^4S)$ formation in the 207 nm photolysis of N_2O by means of two-photon absorption LIF technique (TALIF) using the same focused laser beam at 207 nm. They have not measured the quantum yield for $N(^4S)$ formation. It is difficult to estimate the quantum yield from the experiments using a one-color focused laser beam for both photolysis and probe.

Although the oxidation of N_2O by $O(^1D)$, channel (3.2a), is thought to be the dominant global source of NO in the stratosphere, the photodissociation reaction is a

major removal process of stratospheric N_2O and the $O(^1D)$ reaction is minor. A simple calculation can predict that a quantum yield of 1% for channel (3.1b) in N_2O photolysis would represent an approximate increase of 15% in the active nitrogen production rate in the upper stratosphere. Therefore, a precise determination of the channel (3.1b) quantum yield is essential for evaluating the stratospheric NO production rate.

In this Chapter, laboratory studies on the $N(^4S)$ atom formation from the photolysis of N_2O at 193 nm has been carried out using a technique of VUV-LIF. The quantum yield for $N(^4S)$ formation was determined to be $(2.1 \pm 0.9) \times 10^{-3}$. The atmospheric significance of channel (3.1b) as a new source of NO in the stratosphere is also discussed.

3.2 Experimental

The details of the apparatus used in the present study are shown in Chapter 2 and here only a description related to this chapter is given here. The $N(^4S)$ atoms produced from N_2O photolysis at 193 nm were probed by the VUV-LIF method at 120.07 nm, which is resonant with the electronic transition of $N(2p^23s\ ^4P_{1/2} \leftarrow 2p^3\ ^4S_{2/3})$. The $Cl(^2P_{1/2})$ atoms produced from HCl photolysis at 193 nm were detected by the VUV-LIF technique at 120.14 nm, which is associated with electric transition of $Cl(3p^44s\ ^2D_{3/2} \leftarrow 3p^5\ ^2P_{1/2})$. The tunable VUV laser radiation around 120.14 nm was also obtained with the same experimental setup for the VUV laser system with the Hg vapor cell and the fluorescence detection system.

N_2O (>99.9%, Takachiho Co.) or a gas mixture of HCl (> 99.9%, Sumitomo Seika) and Ar (> 99.999%, Nihon Sanso) (12.3% of HCl in Ar) was supplied into the reaction chamber through a needle valve. The typical pressure of N_2O and a gas mixture of HCl/Ar were 500 – 900 and 160 – 430 mTorr, respectively. While scanning the VUV laser wavelength for $N(^4S)$ and $Cl(^2P_{1/2})$ atom detections, the reactants pressure was kept to be constant. It should be noted that high sensitivity of the VUV-LIF technique make it possible to detect $N(^4S)$ atoms at low gas pressures and short pump-probe delay time (≤150 ns), and that chemical losses through secondary reactions, for example, $N + N_2O$, $N + NO$ and $N + O_2$, can be safely ignored.

In the titration experiments to calibrate the absolute sensitivity of the VUV-LIF system, $N(^4S)$ atoms were generated by the MW (2450 MHz) discharge of pure N_2 gas (>99.9%) in a flow tube (Pylex, 13.7 mm i.d.) as shown in Fig. 2.3. A coaxial flow

tube was connected between the N_2 discharge flow tube and the VUV-LIF chamber. NO/Ar gas mixture (0.0268% of NO in Ar) was introduced through the inner injection tube (Pylex, 3.8 mm i.d.), which can move along the outer flow tube. All experiments were performed at room temperature.

3.3 Results

Figure 3.1 shows the fluorescence excitation spectra for $N(^4S)$ atoms produced in the 193 nm photolysis of N_2O. The atomic line profiles of the $N(^4P_{1/2} \leftarrow {}^4S_{2/3})$ transition were directly observed by the VUV-LIF method around 120.07 nm. The dependence of the LIF signal intensity for the $N(^4S)$ atoms on the photolysis laser pulse is shown in Figure 3.2. We also checked that no $N(^4S)$ atoms signal was detected without 193 nm photolysis light. These results indicate that multiphoton absorption processes at 193 nm or dissociation of parent molecules by the probe laser beams (ω_{VUV}, ω_1 and ω_2) are safely ignored in this work. The quantum yield for $N(^4S)$ formation from N_2O at 193 nm photolysis was determined by calibrating the sensitivity of the VUV-LIF system. The two methods were used to estimate the absolute sensitivity of the detection system for $N(^4S)$ by the VUV-LIF method. One is the titration technique for the $N(^4S)$ atom concentration using chemical reaction with NO. The other is the comparison between the LIF intensities of the $N(^4S)$ atoms produced in the N_2O photolysis at 193 nm and $Cl(^2P_{1/2})$ atoms produced in the HCl photolysis at 193 nm. The $Cl(^2P_{1/2})$ quantum yield from the photolysis of HCl at 193 nm has already been reported [5].

3.3.1 Chemical titration method

The conventional titration technique for N atoms was used to calibrate the VUV-LIF system for detecting $N(^4S)$ atoms [6]. The $N(^4S)$ atoms were generated in a MW discharge of pure N_2 gas and were then introduced into the VUV-LIF chamber through the coaxial flow tube. While monitoring the VUV-LIF signal of $N(^4S)$ atoms at 120.07 nm, NO molecules diluted with Ar were injected into the flow system. The $N(^4S)$ atoms were consumed by the following reaction:

$$N(^4S) + NO \rightarrow N_2 + O \quad k_{3.3}^{298} = 3.0 \times 10^{-11}\ cm^3\ molecule^{-1}\ s^{-1}, \quad (3.3)$$

where $k_{3.3}^{298}$ shows is the rate constant (3.3) at 298 K [7]. By monitoring the LIF signal intensities as a function of the number density of NO molecules added, the

sensitivity of the VUV-LIF system for N atom detection was calibrated. A typical titration plot is shown in Figure 3.3, in which the mass flow rate of NO/Ar mixture was varied between 0.6 and 2.3 sccm while the total flow rate was kept constant (19 sccm). When all the N atoms produced by the MW discharge are consumed by reaction (3.3), the NO concentration corresponds to the initial N atom concentration. Thus, the absolute concentration of N atoms detected by the VUV-LIF method was obtained. The inner NO injection tube is movable so that the reaction time can be varied by changing the location of the addition of the NO molecules. To check the wall reactivity of $N(^4S)$, the titration experiments were carried out under different residence time conditions (0.2 – 0.5 s) by changing the location of the NO injection. No significant influence from the wall-loss of $N(^4S)$ atoms was observed, which is consistent with the very low wall reactivity reported by Wennberg et al. [8].

Fluorescence excitation spectra for $N(^4S)$ atoms produced in the N_2O photolysis at 193 nm and the MW discharge of N_2 were measured to determine the quantum yield for $N(^4S)$ formation in the N_2O photolysis. The $N(^4S)$ production quantum yield from the photolysis of N_2O is defined by the number density of $N(^4S)$ atoms produced from the photolysis divided by the number density of N_2O molecules exited by the photolysis laser light. The formation yield of $N(^4S)$ atoms, Φ_N, from the photolysis of N_2O at 193 nm is expressed as follows:

$$\Phi_N = \frac{(A_{Ph}/A_{MW})[N]_{MW}}{\sigma_{N2O}[N_2O]I_{Ph}} \times \frac{F_{MW}}{F_{Ph}} \quad (3.4)$$

A_{Ph} and A_{MW} are the areas of the resonance peaks of the fluorescence excitation spectra of $N(^4S)$ atoms produced in the photolysis of N_2O at 193 nm and in the MW discharge of N_2, respectively, under same conditions for the N atom detection. $[N]_{MW}$ is the concentration of N atom produced in the MW discharge of N_2, which calibrated by the titration technique. σ_{N2O} is the photoabsorption cross section of N_2O at 193 nm, 8.95×10^{-20} cm^2 molecule^{-1} [7]. $[N_2O]$ is the concentration of N_2O in the chamber. I_{Ph} is the photon density of the incident photolysis laser light, which was measured to be 8.4×10^{16} photons cm^{-2}. Intensity variation of the photolysis laser light was small (<5%) throughout the measurements. F_{Ph} and F_{MW} are the detection efficiencies of the fluorescence monitoring in the photolysis and MW discharge experiments, respectively, where the excitation volume by the probe laser in the chamber, the overlap region of the

193 nm photolysis laser with the probe laser, and the solid angle from the emitting region onto the photocathode of the PMT are take into account. The length of the volume excited by the probe laser in the viewing zone of the PMT was 15 mm, while that of the volume where the probe laser beam overlapped with the photolysis laser was 6 mm. Therefore, the value of F(MW)/F(ph) was estimated to be 2.5. Three sets of experiments were performed for the chemical titration method. Consequently, Φ_N was determined to be $(2.25 \pm 0.71) \times 10^{-3}$. The quoted error includes the 1σ-statistical and estimated systematic uncertainties for the VUV-LIF detection and the N atom concentration calibration.

3.3.2 Photolytic calibration method

Figure 3.4 shows the fluorescence excitation spectrum for $Cl(^2P_{1/2})$ atoms produced in the 193 nm photolysis of HCl. By comparing the relative intensities of LIF signals of $N(^4S)$ from N_2O and $Cl(^2P_{1/2})$ from HCl photolysis, the $N(^4S)$ quantum yield can be estimated. Experimentally, measurements of spectra for N and Cl atom were alternatively performed by changing both the reactants and laser wavelengths.

The quantum yield for $N(^4S)$ formation, Φ_N, from the photolysis of N_2O at 193 nm is obtained by the following equation:

$$\Phi_N = \frac{A_N}{A_{Cl}} \frac{I_{Cl}}{I_N} \frac{\sigma_{HCl}}{\sigma_{N2O}} \frac{[HCl]}{[N_2O]} \frac{f_{Cl}}{f_N} \frac{\varphi_{Cl}}{\varphi_N} \Phi_{Cl} \quad . \qquad (3.5)$$

A_N and A_{Cl} are the areas of resonance peaks in the fluorescence excitation spectra of $N(^4S)$ atoms in the photolysis of N_2O and $Cl(^2P_{1/2})$ atoms in the photolysis of HCl, respectively. I_N and I_{Cl} are the relative probe laser intensities for N and Cl atom detection which obtained as a photoionization current from the NO containing cell. The photoionization efficiencies of NO molecule used at 120.07 and 120.14 nm are also taken into account [9,10]. σ_{HCl} is the photoabsorption cross section of HCl at 193 nm, 8.69×10^{-20} $cm^2molecule^{-1}$ [7]. [HCl] is the concentration of HCl molecules in the chamber. f_N and f_{Cl} are the oscillator strength values for the $N(2p^23s\ ^4P_{1/2} \leftarrow 2p^3\ ^4S_{3/2})$ and $Cl(3p^44s\ ^2D_{3/2} \leftarrow 3p^5\ ^2P_{1/2})$ optical excitation. The values of f_N and f_{Cl} are taken from the database of *National Institute of Standard and Technology* (NIST) [11]. φ_N and φ_{Cl} indicate the detection efficiencies of the resonance fluorescence for N and Cl atoms, respectively. As for $Cl(^2P_{1/2})$ atom detection, the exited $Cl(^2D_{3/2})$ state

fluoresces at 120.14 and 118.88 nm, which are resonant to the $^2D_{3/2} \rightarrow {}^2P_{1/2}$ and $^2D_{3/2} \rightarrow {}^2P_{3/2}$ transition, respectively. The detection efficiencies of the PMT system among the wavelengths at 120.07, 120.14 and 118.88 nm for the $N(^4P_{1/2} \rightarrow {}^4S_{3/2})$, $Cl(^2D_{3/2} \rightarrow {}^2P_{1/2})$ and $Cl(^2D_{3/2} \rightarrow {}^2P_{3/2})$ emission lines, respectively, are assumed to be constant since those wavelength are very close to each other. The quantum yield of $Cl(^2P_{1/2})$ atoms in the photolysis of HCl at 193 nm photolysis, Φ_{Cl}, is reported to be 0.408 [6]. In this experiment, the collisional relaxation and the chemical reaction of $Cl(^2P_{1/2})$ could be ignored. The pressures of HCl and Ar buffer gas were 20 and 160 mTorr and the time delay between the photolysis and probe laser pulses was 130 ns, and the relaxation rate of $Cl(^2P_{1/2})$ by collision with HCl and Ar are 7.8×10^{-12} and $\leq 1.0 \times 10^{-14}$ cm^3 $molecule^{-1}$ s^{-1}, respectively [12,13] Twenty-three sets of experiments were performed for photolytic calibration method. Consequently, $\Phi_N = (1.70 \pm 1.21) \times 10^{-3}$ was obtained. The quoted error includes the 1σ-statistical and estimated systematic uncertainties.

The results obtained from the two different experiments of the chemical titration and photolytic calibration methods are in good agreement with each other within the experimental uncertainties. The quantum yield value for $N(^4S)$ formation in the 193 nm photolysis of N_2O is determined to be $\Phi_N = (2.1 \pm 0.9) \times 10^{-3}$ by combining the two experiments results form two methods, in which the majority of the error from each of the two methods are systematic uncertainties.

3.4 Discussion

3.4.1 Dissociation process of N_2O to produce $N(^4S)$ + NO

In the photolysis of N_2O around 200 nm, there are four energetically available dissociation pathways:

$$N_2O + h\upsilon \rightarrow N_2(X\,{}^1\Sigma^+_g) + O(^1D) \quad (3.1a)$$

$$\rightarrow N(^4S) + NO(X\,{}^2\Pi) \quad (3.1b)$$

$$\rightarrow N_2(X\,{}^1\Sigma^+_g) + O(^3P) \quad (3.1c)$$

$$\rightarrow N_2(X\,{}^1\Sigma^+_g) + O(^1S). \quad (3.1d)$$

In this work, we determined the quantum yield for $N(^4S)$ production in the photolysis of N_2O at 193 nm. Our result of $\Phi_N = (2.1 \pm 0.9) \times 10^{-3}$ is smaller than the upper-limit value presented by Greenblatt and Ravishankara [3]. They estimated the NO production yield (channel 3.1b) by observing the chemiluminescence of NO_2 that was formed by the reaction of O_3 and NO fragments produced from N_2O photolysis. A

quite small quantum yield value can be explained by a spin-forbidden nature for channel (3.1b).

Figure 3.5 shows the correlation diagram for the reactions of O + N_2 and NO + N, in which C_s symmetry is assumed for the reaction intermediate [14]. N_2O has 16 valence electrons and belongs to $C_{\infty v}$ symmetry group when it is in its electronic ground state X $^1\Sigma^+$ ($4\sigma^2 5\sigma^2 6\sigma^2 1\pi^4 7\sigma^2 2\pi^4$ configuration). The lowest electronically exited singlet states are the A $^1\Sigma^-$, the B $^1\Delta$, and the C $^1\Pi$ states. Upon bending the C_s symmetry group applies giving rise to the 1 ^{1}A′ ($^1\Sigma^+$) and the 1 ^{1}A″ ($^1\Sigma^-$) states. The Π and Δ states split into A′ and A″ components. The theoretical calculations by Hopper show that dissociation around 200 nm occurs via the 2 ^{1}A′ state, and that the nearby 1 ^{1}A″ state can also be involved in the dissociation process. While the 2 ^{1}A′ state is part of a Renner-Teller pair, the component of this pair has a linear equilibrium geometry and its energy increases rapidly as the molecule bends. Teule et al. [15] studied the photodissociation of N_2O around 203 nm by a technique of photofragment imaging, and showed that the parallel transition to the 2 ^{1}A′ state is dominant.

Previous studies showed that channel (3.1a) is dominant with almost unity quantum yield in the 193 nm photolysis of N_2O [1], which is rationalized by the fact that both the 2 ^{1}A′ and 1 ^{1}A″ states adiabatically correlate to the photoproducts of O(^{1}D) + N_2 (channel 3.1a). In the present study, the N(^{4}S) atom formation (channel 3.1b) is observed directly by the VUV-LIF method and the quantum yield is determined to be $(2.1 \pm 0.9) \times 10^{-3}$. The adiabatic correlation diagram shown in Fig. 3.5 suggests that the intersystem crossing from the exited singlet state to the triplet state or direct photoexcitation to the triplet states can account for the N(^{4}S) formation. A weak spin-orbit interaction between the singlet and triplet excited states or a small transition probability from the ground to the triplet states may results in the very small quantum yield for N(^{4}S) formation in N_2O photolysis at 193 nm.

3.4.2 Atmospheric implications

We have investigated the atmospheric importance of channel (3.1b). The stratospheric sink of N_2O is mainly due to UV photolysis in the atmospheric window region. The remaining sink of N_2O is reaction with O(^{1}D) which is produced by the ozone photolysis:

$$N_2O + O(^1D) \rightarrow 2NO \qquad k_{3.2a} = 6.7 \times 10^{-11}\ cm^3\ molecule^{-1}\ s^{-1} \qquad (3.2a)$$

$$\rightarrow N_2 + O_2 \quad k_{3.2b} = 4.9 \times 10^{-11} \text{ cm}^3 \text{ molecule}^{-1} \text{ s}^{-1}. \quad (3.2b)$$

About 60% of the $N_2O + O(^1D)$ reaction proceeds via reaction (3.2a) and about 40% via reaction (3.2b). Reaction (3.2a) is an important source of stratospheric NO. The photolysis of N_2O proceedings via photodissociation channel $N(^4S)$ + NO can also provide a stratospheric NO source.

The current NASA/JPL evaluations for stratospheric modeling recommend that the quantum yield for photodissociation of N_2O around 200 nm is unity, and the products are N_2 and $O(^1D)$ (channel 3.1a), in spite of referring that the yield of $N(^4S)$ and $NO(^2\Pi)$ is less than 1%. However, the $N(^4S)$ and $NO(^2\Pi)$ formation (channel 3.1b) can be a non-negligible direct source of stratospheric NO_x. The stratospheric O_3 abundance and its vertical profile are significantly affected by NO_x, because NO_x can catalytically destroy stratospheric O_3. In this study, we have investigated the atmospheric importance of channel (3.1b) in the photolysis of N_2O, by using a one-dimensional dynamical-photochemical model. All chemical schemes of the model are the same with that in the Garcia-Solomon two-dimensional (GS-2D) model [16,17]. The model calculations were performed including 40 chemical species and 120 chemical reactions with the chemical kinetics and photochemical data presented by the recent JPL recommendations [7]. We included channel (3.1b) quantum yield value of 2.1×10^{-3} in the model on the assumption that it is independent of the temperature and wavelength at the atmospheric window region.

Figure 3.6 shows the result of the photochemical model calculations for latitude of 40 degree in March, which indicates the change in the diurnally averaged concentrations of NO_x, HO_x, ClO_x and O_3 concentrations calculated with or without channel (3.1b) in the photolysis of N_2O. The steady-state NO_x concentration calculated by the model including channel (3.1b) increases up to ~3% around 25 km in comparison with that ignoring channel (3.1b), while the HO_x and ClO_x abundances decrease. The altitude-dependent change in the NO_x concentration should reflect the altitude-dependent solar flux at the atmospheric window wavelength region. The concentrations of HO_x and ClO_x may be attributable to the following reactions:

$$OH + NO_2 + M \rightarrow HNO_3 + M \quad (3.6)$$

$$ClO + NO_2 + M \rightarrow ClONO_2 + M \quad (3.7)$$

$$OH + HCl \rightarrow Cl + H_2O. \quad (3.8)$$

The concentration changes of HO_x and ClO_x are larger in the lower stratosphere as

shown in Fig. 3.6, because the contribution of three-body reactions (3.6) and (3.7) becomes more significant at lower stratospheric altitudes. Reaction (3.8) converts the chlorine reservoir HCl into active ClO_x. The decrease of the HO_x concentration may result in the decrease of ClO_x through reaction (3.8). The chemical reactions of NO_x, HO_x and ClO_x families play a crucial role in determining the stratospheric O_3 abundance, and thus the concentration changes of these species alter O_3 abundance. Inclusion of channel (3.1b) in the model affects the production rate of NO_x, which is followed by the decrease of O_3 abundance through the enhancement of the NO_x catalyzed O_3 destruction rate, as shown in Fig. 3.6.

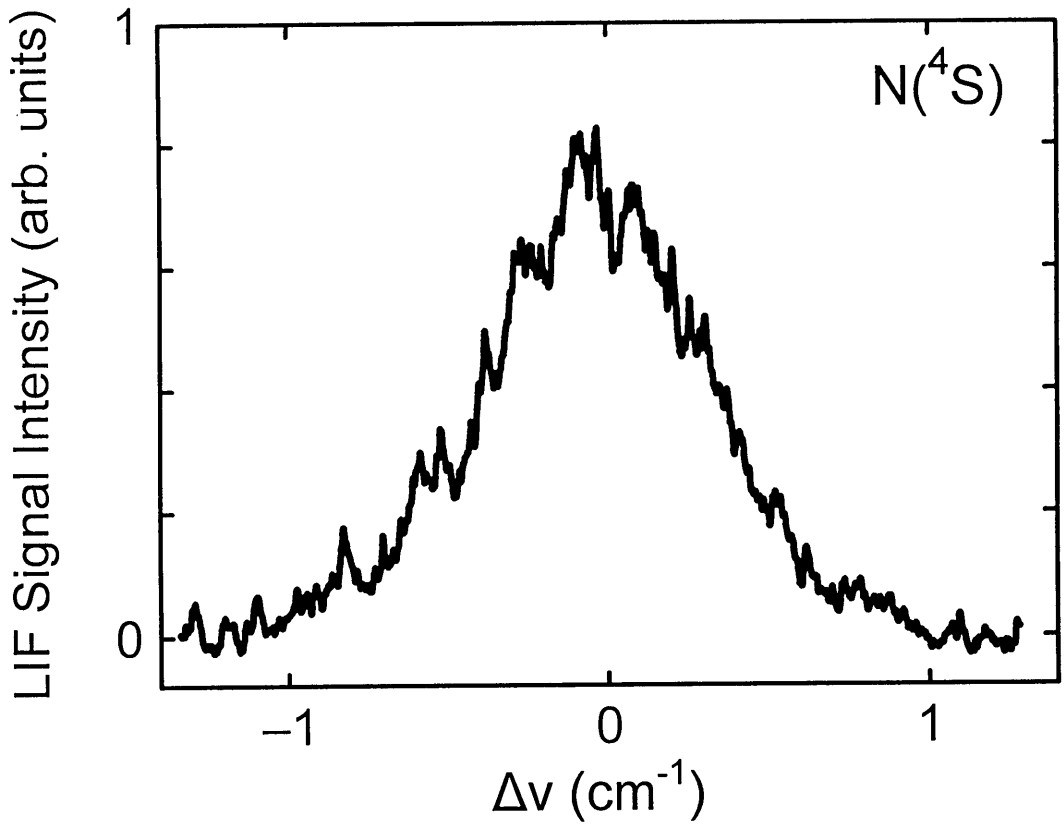

Figure 3.1. Fluorescence excitation spectra of $N(^4S)$ produced from the photolysis of N_2O at 193 nm. The horizontal scale indicates the wavenumber shift from the resonance line center of the $^4P_{1/2} \leftarrow {}^4S_{3/2}$ transition for N atom at 120.07 nm. The delay time between the photolysis and probe laser pulses was 130 ns. The pressure of N_2O was 700 mTorr.

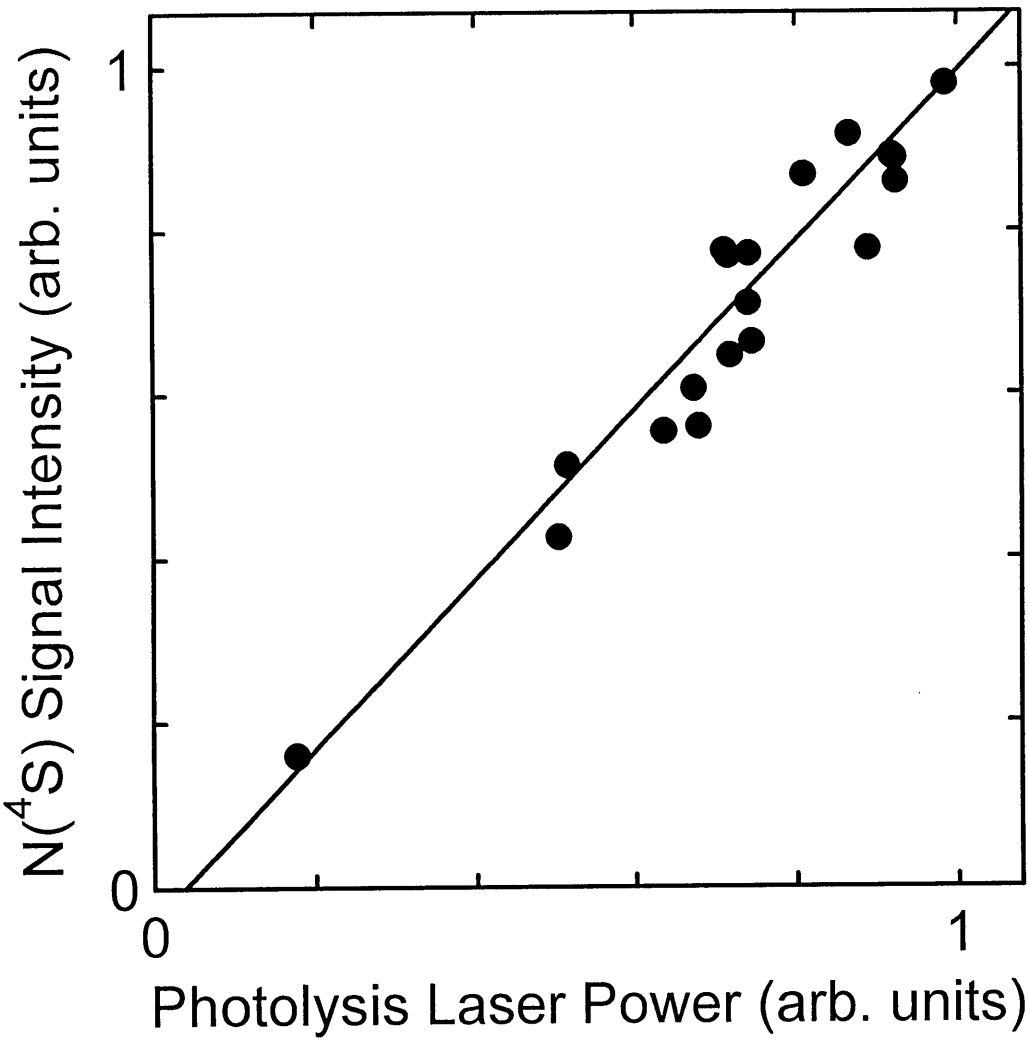

Figure 3.2. LIF signal intensity for N(^{4}S) versus the photolysis laser power. The photolysis laser power was changed while monitoring the N(^{4}S) LIF signal at 120.07 nm. The time delay between the photolysis and probe laser pulses was 150 ns and the pressure of N_2O in the reaction cell was 800 mTorr. Solid line is the results of linear weighted fit analysis of the experimental data.

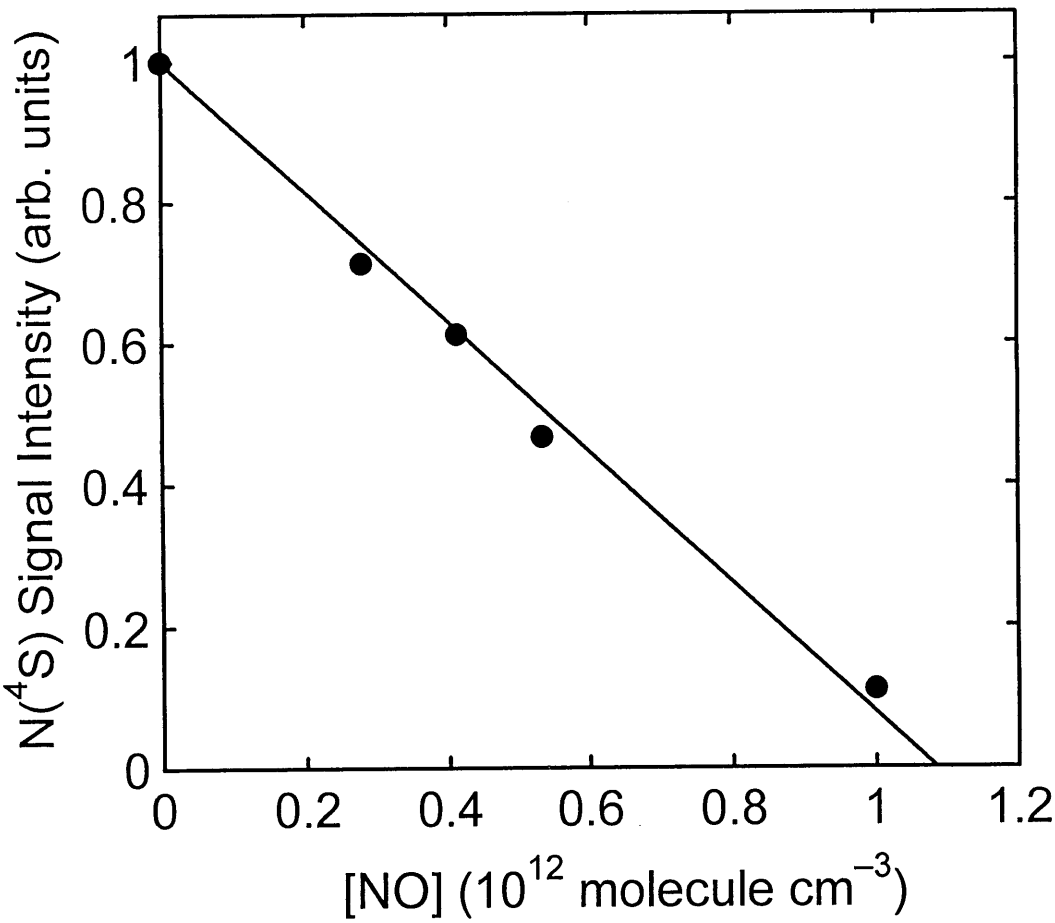

Figure 3.3. Plots of the titration for the N atoms produced by the microwave discharge of N_2. The horizontal axis is the NO concentration added downstream of the discharge. The vertical axis is the LIF intensity of $N(^4S)$. The solid line indicates the results of the 1st-order least square fitting.

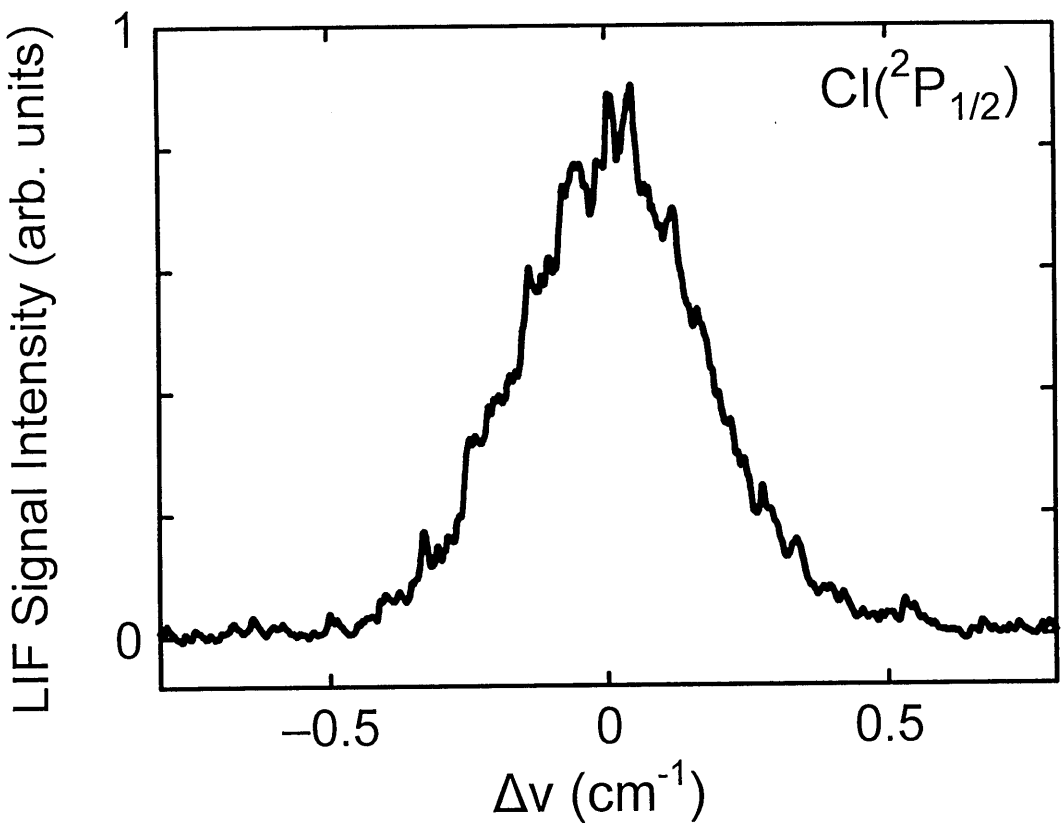

Figure 3.4. Fluorescence excitation spectrum of Cl($^2P_{1/2}$) atoms produced from the 193 nm photolysis of HCl. The horizontal scale indicates the wavenumber shift from the resonance line center of the $^2D_{3/2} \leftarrow {}^2P_{1/2}$ transition for Cl atom at 120.07 nm. The delay time between the photolysis and probe laser pulses was 130 ns. The partial pressure of HCl was 50 mTorr.

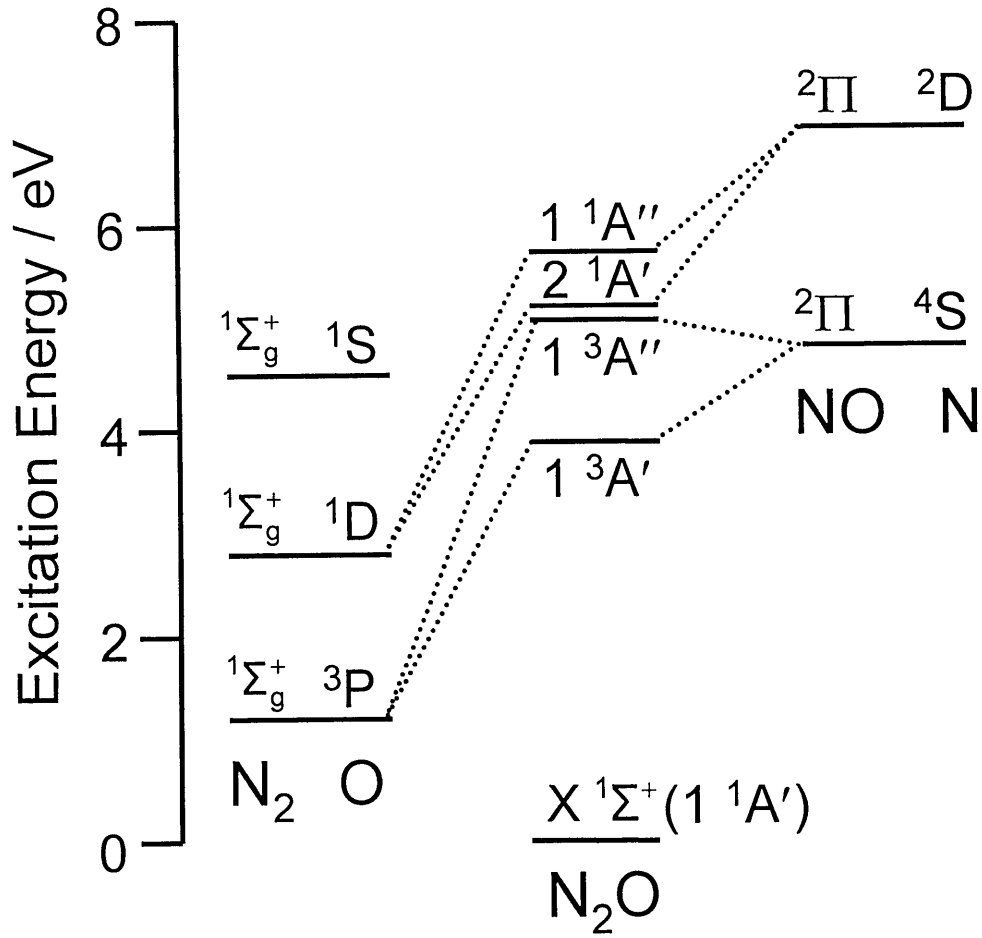

Figure 3.5. An adiabatic correlation diagram for N_2O (N-NO, N_2O, N_2-O) system assuming a C_s symmetry, which is taken from Hopper [14]. The energy levels are drawn to scale.

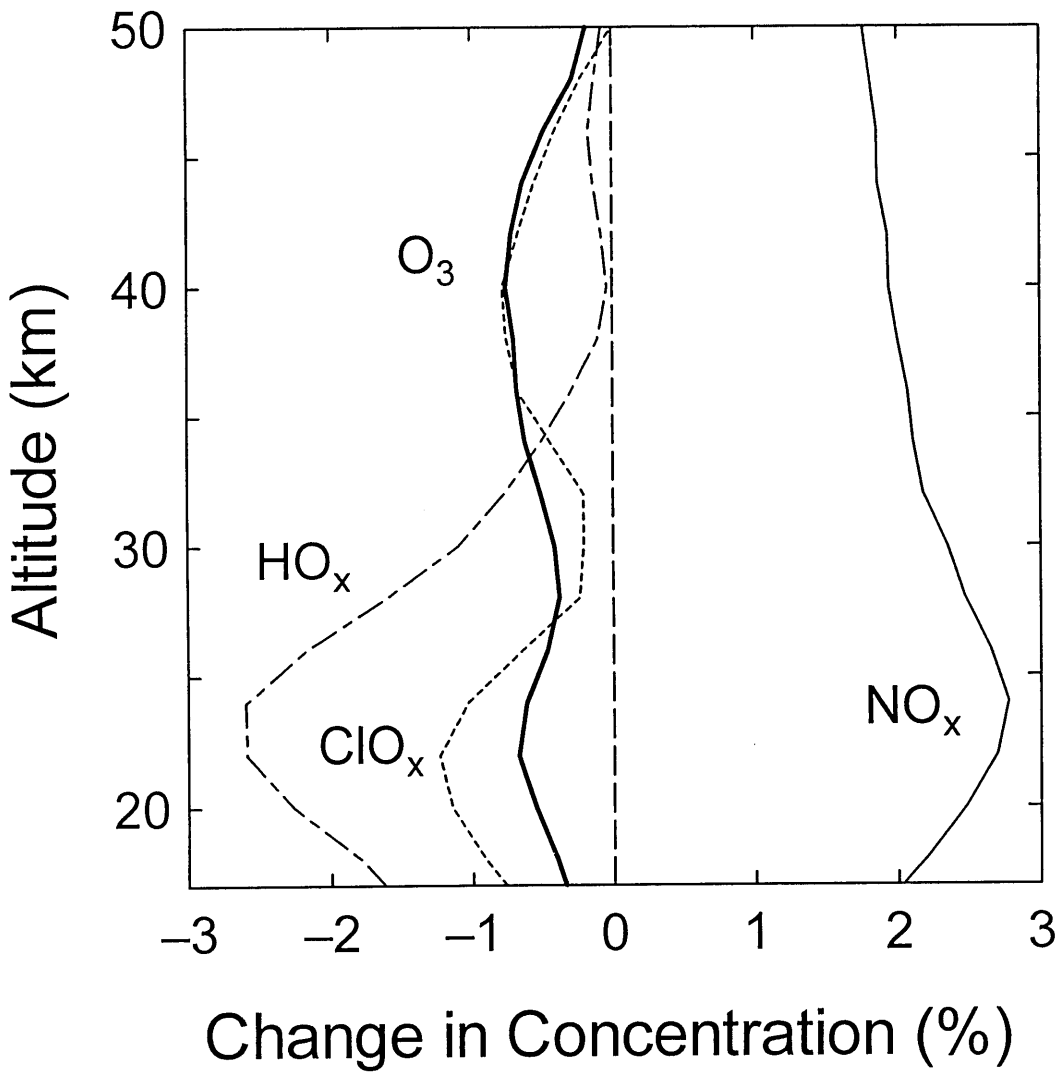

Figure 3.6. Calculated percentage changes in NO_x, HO_x, ClO_x, and O_3 concentrations with the $N(^4S)$ + NO dissociation channel from those calculated without the $N(^4S)$ + NO channel for latitude of 40° in March as a function of altitude.

References for Chapter 3

[1] Okabe, H., *Photochemistry of Small Molecules*, John Wiley & Sons, New York, 1978.

[2] Felder, P., Haas, B. –M., Huber, J. R., *Chem. Phys. Lett.*, **186**, 177 (1991).

[3] Greenblatt, G. D., Ravishankara, A. R., *J. Geophys. Res.*, **95**, 3539 (1990).

[4] Adams, S. F., DeJoseph Jr. C. A., Carter , C. C., Miller , T. A., Williamson, J. M., *J. Phys. Chem.*, **A105**, 5977 (2001).

[5] Zhang, J., Dulligan, M., Witting, C., *J. Chem. Phys.*, **107**, 1403 (1994).

[6] Boisse-Laporte, C., Chave-Normand, C., Marec, J., *Plasma Sources Sci. Technol.*, **6**, 70 (1997).

[7] Sander, S. P., Friedl, R. R., Golden, D. M., Kurylo, M. J., Huie, R. E., Orkin, V. L., Moortgat, G. K., Ravishankara, A. R., Kolb, C. E., Molina, M. J., Finlayson-Pitts, B. J., *Chemical Kinetics and Photochemical Data for use in Atmospheric Studies*, Evaluation No. 14, JPL Publication 02-25, 2003.

[8] Wennberg, P. O., Anderson, J. G., Weisenstein, D. K., *J. Geophys. Res.*, **99**, 18,839 (1994).

[9] Ono, Y., Lin, S. H., Prest, H. F., Ng, C. Y., *J. Chem. Phys.*, **73**, 4855 (1980).

[10] Erman, P., Karawajczyk, A., Rachlew-Källne, E., Strömholm, C., *J. Chem. Phys.*, **102**, 3064 (1995)

[11] Martin, W.C., et al., *NIST Atomic Spectra Database (version 2.0)*, National Institute of Standards and Technology, Gaithersburg, MD (http://physics.nist.gov/asd), 1999.

[12] Sotnichenko, S. A., Bokun, V. Ch., Nadkhin , A.I., *Chem. Phys. Lett.*, **153**, 560 (1988).

[13] Hitsuda, K., Takahashi, K., Matsumi, Y., Wallington, T.J., *J. Phys. Chem.*, **A105**, 5131 (2001).

[14] Hopper, D. G., *J. Chem. Phys.*, **80**, 4290 (1984).

[15] Teule, J. M., Groenenboom, G. C., Neyer, D. W., Chandler, D. W., Janssen, M. H. M., *Chem. Phys. Lett.*, **320**, 177 (2000).

[16] Solomon, S., R. Portmann, W., Garcia, R. R., Thomason, L. W., Poole, L. R., McCormick, M. P., *J. Geophys. Res.*, **101**, 6713 (1996).

[17] Taniguchi, N., Hayashida, S., Takahashi, K., Matsumi, Y., *Atoms. Chem. Phys.*, **3**, 1293 (2003).

Chapter 4

Kinetics of the atmospheric reactions of $N(^4S)$ atoms with NO and NO_2

4.1 Introduction

Photochemical processes involving the $N(^4S)$ atom and NO_x molecules play a crucial rule in the terrestrial and planetary atmospheres [1,2,3,4]. For instance, the reaction of $N(^4S)$ with nitric oxide:

$$N(^4S) + NO \rightarrow N_2 + O(^3P), \qquad (4.1)$$

has been thought to act as a sink of odd nitrogen in the middle and upper terrestrial atmosphere [1,2]. Possible significance of the reaction (4.1) in the Martian and Venusian atmosphere has also been suggested [2]. The reaction of $N(^4S)$ with nitrogen dioxide:

$$N(^4S) + NO_2 \rightarrow N_2O + O(^3P), \qquad (4.2)$$

plays a less significant role as a sink of odd nitrogen in the middle terrestrial atmosphere because of the small concentration of NO_2 [5]. A small amount of N_2O may be formed by reaction (4.2) in the Martian atmosphere [4]. For the $N + NO_2$ reaction, other channels forming 2NO, $N_2 + O_2$, and $N_2 + O + O$, are energetically possible. However, those channels are suggested to be of minor importance as related to products [5].

Although a number of kinetic studies of the reactions (4.1) and (4.2) have been reported at room temperature, as listed in Table 4.1, agreement among them is relatively poor. In previous kinetic studies, several techniques such as microwave discharge of N_2 [5,6,7,8,9,10,11,12,13,14], VUV flash photolysis of N_2O [10,15], and pulsed radiolysis of N_2 [16], were employed to generate the $N(^4S)$ atoms. For $N(^4S)$ detection, mass spectrometry techniques were used in several studies [6,7,8,9,13,14]. With nitrogen atom lamps, resonance fluorescence detection [5,10,11,12,15] and resonance absorption detection [16] of the $N(^4S)$ atoms were also used. In the present study, it is demonstrated that the laser flash photolysis/VUV-LIF detection technique is a powerful tool for the study of the kinetics of the reactions (4.1) and (4.2), in which the $N(^4S)$ formation following 193 nm ArF laser irradiation of NO and NO_2 has been utilized as a photolytic source of $N(^4S)$ atoms.

The $N(^4S)$ formation following 193 nm ArF laser irradiation of NO under shock-heated conditions (1400-3500 K) was reported by several groups [17,18], in which the $N(^4S)$ atoms were monitored by atomic resonance absorption spectroscopy at 119.9 nm:

$$NO + h\nu(193\ nm) \rightarrow N(^4S) + O(^3P). \qquad (4.3)$$

Three doublet states of NO $A^2\Sigma^+(v' = 3)$, $B^2\Pi(v' = 7)$, and $C^2\Pi(v' = 3)$ lie near the dissociation limit of NO, as shown in Figure 4.1. They suggested that N atoms are produced by direct excitation of vibrationally excited states of $NO(X^2\Pi, v \geq 1)$ to the $D^2\Sigma^+$ state, following conversion from the $D^2\Sigma^+$ state to the predissociating $C^2\Pi$ state. In the present study, the first observation of the $N(^4S)$ formation following 193 nm irradiation of NO at 295 K has been reported. Photoexcitation processes of NO giving rise to the $N(^4S)$ atom formation at 295 K have been discussed.

Photoexcitation processes of NO_2 in the UV region have been thoroughly investigated at a number of wavelengths other than 193 nm [19]. At 193 nm, there are only a limited number of experimental studies on the photoexcitation processes. The following two channels are thought to be dominant as photodissociation pathways at 193 nm,

$$NO_2 + h\nu(193\ nm) \rightarrow NO(X^2\Pi) + O(^3P) \qquad (4.4a)$$

$$\rightarrow NO(X^2\Pi) + O(^1D), \qquad (4.4b)$$

and the branching ratio for $O(^1D)$ and $O(^3P)$ productions was estimated to be $[O(^1D)]/([O(^1D)]+[O(^3P)]) = 0.55 \pm 0.03$ [20]. Gradd and Slanger [21] observed the vibrationally excited $NO(X^2\Pi, v=4\text{-}10)$ in the photodissociation of NO_2 at 193 nm. Gong et al. [22] reported that the nascent vibrational state populations of $NO(X^2\Pi, v=1\text{-}7)$ in the photodissociation of NO_2 at 193 nm have a maximum at $v = 5$. Tsuji et al. [23] studied the decomposition of NO_2 in N_2 atmosphere at 193 nm by ArF laser irradiation, and observed a lower NO yield than that predicted from simple NO_2 photolysis (reactions 4.4a and 4.4b) at a low NO_2 concentration of 200 ppm. They suggested that the lower NO yield was attributable to the photolytic loss of vibrationally excited NO which was primarily produced from NO_2 photolysis at 193 nm. The $N(^4S)$ and O_2 productions are energetically possible in the UV region below 272 nm:

$$NO_2 + h\nu \rightarrow N(^4S) + O_2. \qquad (4.4c)$$

Matsumi et al. [24] detected laser-induced fluorescence from the vibrationally excited O_2 molecules around 220-300 nm following the irradiation of focused visible

laser light (470-580 nm) on NO_2 gas, and suggested that the vibrationally excited O_2 molecules were directly produced from a multiphoton absorption process of NO_2. However, further experimental studies revealed that the O_2 molecules were produced from the reaction of O* + NO_2 where O* was generated from the multiphoton dissociation of NO_2 [25,26]. There has been no experimental observation of channel (4.4c) with the irradiation of ArF laser. In the present study, the first experimental observation of the N(^{4}S) production from NO_2 with high-power ArF laser irradiation at 193 nm has been reported. The photoexcitation processes of NO_2 giving rise to the N(^{4}S) formation have been discussed.

4.2 Experimental

The details of the apparatus used in the present study are shown in Chapter 2 and here only a description related to this chapter will be given. NO gas (>99%, Nihon Sanso) purchased was used after purification by passing it through a cold trap that was immersed in a methanol/liquid N_2 slush bath at 175 K. Helium gas (>99.99%, Iwatani Gas) was used without further purification in the kinetic experiments. Much attention was paid to the handling of NO_2 gas reagent in this study, since purified NO_2 gas is easy to degrade to NO mixture and the reaction rate constant of NO with N(^{4}S) has been reported to be about 5 times larger than that of NO_2 (Table 4.1). The NO_2 gas was synthesized by mixing the purified NO gas with excess O_2 (>99.99%, Nihon Sanso) in a glass vessel (2 L), and stored in the vessel for more than several days prior to use in the experiments. The total pressure of the NO_2/O_2 vessel was about 700 Torr with the mixing ratio $[NO_2] : [O_2] \approx 1 : 3$. For the NO_2 photolysis and kinetics experiments, the gas mixture of NO_2/O_2 was supplied to the reaction cell directly from the vessel through a mass flow controller. N_2O_4 equilibrates with NO_2 gas. The equilibrium between NO_2 and N_2O_4 in the reactant gas which was flowed into the reaction cell was estimated to be attained within 10^{-6} s [19] before the laser irradiation. When the partial pressure of NO_2 is 1×10^{16} molecule cm^{-3}, the partial pressure of N_2O_4 is about 1/400 of NO_2 at 298 K using the equilibrium constant presented by NASA/JPL [27].

The concentration of NO_2 in the reaction chamber was determined directly by absorption measurements. The collimated output of a tungsten lamp was passed through the reaction chamber and focused onto the entrance slit of a spectrograph with a 2048-element diode array detector (Oceans Optics, HR2000, f = 101 mm). A 10-μm

entrance slit was used for absorption measurements at a resolution of ~0.7 nm. The absorption features of the NO_2 spectrum recorded between 300 and 650 nm are in good agreement with previous measurements [28 , 29 , 30]. The wavelength of the spectrometer was calibrated at 404.66 and 435.84 nm using an Hg pen ray lamp. The concentration of NO_2 was determined by absorption measurements around 413.7 nm on the basis of the reported absorption cross-section [28,29,30]. The contribution of N_2O_4, if present, is minimized at this wavelength, as described by Gierczak et al.[30]. The uncertainty associated with the measurements of NO_2 concentration was estimated to be ~ 10%. All experiments were performed at 295 ± 2 K.

4.3. Results and discussion

4.3.1 $N(^4S)$ production following 193 nm laser irradiation of NO

Figure 4.2a shows a typical fluorescence excitation spectrum of the nascent $N(^4S)$ atoms produced following 193 nm laser irradiation of NO, which was obtained by scanning the probe laser wavelength across the $2p^23s\ ^4P_{1/2}$ - $2p^3\ ^4S_{3/2}$ transition at 120.07 nm. The spectrum was taken at 80 ns delay time with 145 mTorr of NO, and no buffer gas was added. It should be noted that the dissociation limit of rovibrationally cold NO giving rise to the $N(^4S)$ + $O(^3P)$ channel is 52397 ± 2 cm^{-1} [31], which is slightly larger than the photon energy of the ArF laser radiation (193.3 nm) of 51730 cm^{-1}. To reveal the photodissociation processes of NO producing the $N(^4S)$ atom, photolysis laser power dependence of the LIF signal was measured. As shown in Figure 4.3a, we found that the LIF intensity was linearly dependent on the photolysis laser power. When we turned the ArF excimer laser off, no obvious LIF signal was observed. This indicates that the $N(^4S)$ production from the NO photodissociation at 120 nm was negligible under our experimental conditions. These results suggest that the $N(^4S)$ formation observed in this study was attributable to the one-photon excitation process of NO:

$$NO + h\nu(193\ nm) \rightarrow N(^4S) + O(^3P). \qquad (4.3)$$

To check the interference in the measurements because of impurities, we recorded the fluorescence excitation spectra of the nascent $N(^4S)$ atoms produced from purified and nonpurified NO. No significant change was observed in the signal intensities and spectral shapes of $N(^4S)$.

Three doublet states of NO $A^2\Sigma^+(v = 3)$, $B^2\Pi(v = 7)$, and $C^2\Pi(v = 3)$ lie near

the dissociation limit of NO. Davidson and Hanson [17] and Koshi et al. [18] reported the $N(^4S)$ formation following 193 nm laser irradiation of NO under the shock-heated conditions. The $N(^4S)$ atom formation was attributed to direct excitation of vibrationally excited states of NO $X^2\Pi(v \geq 1)$ to the $D^2\Sigma^+$ state [17]. In our experiments which were performed at room temperature, it is unlikely that the direct photoexcitation from the NO $X^2\Pi(v = 1)$ to the $D^2\Sigma^+(v = 0)$ state is significantly responsible for $N(^4S)$ formation, because the population of vibrationally excited NO $X^2\Pi(v = 1)$ is negligibly small at room temperature.

Shibuya and Stuhl [32,33,34] investigated the excited-states dynamics of NO through the measurements of emission spectra and fluorescence lifetimes following 193 nm laser irradiation. They observed the fluorescence from $B^2\Pi(v = 7)$, $C^2\Pi(v = 0)$, and $A^2\Sigma(v = 3)$ states. The 193-nm laser light can be resonant with the absorption of the NO $B^2\Pi(v = 7) \leftarrow X^2\Pi(v = 0)$ and $A^2\Sigma(v = 3) \leftarrow X^2\Pi(v = 0)$ transitions. From the available spectroscopic data [35], NO $X^2\Pi$ $(v = 0)$ is expected to be excited to the $B^2\Pi(v = 7)$ state via the absorption lines $R_{11}(30.5\text{-}32.5)$, $P_{11}(27.5\text{-}29.5)$, $Q_{11}(28.5\text{-}31.5)$, $R_{22}(28.5\text{-}30.5)$, $P_{22}(25.5\text{-}27.5)$ and $Q_{22}(26.5\text{-}29.5)$. The $A^2\Sigma(v = 3)$ state can also be prepared via the absorption of $X^2\Pi(v = 0, J\sim50.5)$. The Boltzmann population of the $X^2\Pi(v = 0, J \sim50.5)$ state is much smaller than that of $X^2\Pi(v = 0, J \sim 28.5)$ at 295 K. Shibuya and Stuhl [32,33,34] suggested that the rotational levels of J = 21.5-34.5 for the F_1 component and J = 20.5-33.5 for the F_2 component of the $B^2\Pi(v = 7)$ state were prepared following 193 nm excitation at room temperature, and that the $C^2\Pi(v = 0)$, and $A^2\Sigma(v = 3)$ states were produced by the collisional relaxation from the $B^2\Pi(v = 7)$ state. They also indicated that the photoexcited levels of the $B^2\Pi(v = 7)$ state are predissociative and that the fluorescence quantum yield is about 0.15 and $< 6 \times 10^{-3}$ for J = 20.5 - 29.5 and J > 29.5, respectively. Therefore, it is likely that the $N(^4S)$ atom formation observed in the 193 nm laser irradiation of NO in this study is due to the photoexcitation to the high rotational levels of the $B^2\Pi(v = 7)$ state, which is followed by the predissociation to $N(^4S) + O(^3P)$.

The Doppler profile of the nascent $N(^4S)$ atoms produced from the 193 nm irradiation of NO (Fig. 4.2a) is slightly wider than that of the thermalized $N(^4S)$ atoms (broken curve in Fig. 4.2b). The kinetic energy release in channel (3) is estimated to be ~1000 cm^{-1} from the Doppler profile of the nascent $N(^4S)$ atoms. This is consistent with the fact that the high rotational levels (F_1 J = 21.5 - 34.5, F_2 J = 20.5 - 33.5) in the

$B^2\Pi(v = 7)$ state lie above the dissociation limit by 500 - 1100 cm^{-1}.

4.3.2 $N(^4S)$ production following 193 nm laser irradiation of NO_2

Figure 4.2b shows a typical example of the fluorescence excitation spectrum of the nascent $N(^4S)$ atoms produced from the 193 nm laser irradiation of NO_2, in which gas pressure in the chamber was 34 mTorr and 82 mTorr for NO_2 and O_2, respectively, without buffer gas. The spectrum was taken at 80 ns delay time. The FWHM of the spectrum was estimated to be 1.38 cm^{-1} with a Gaussian shape (Fig. 4.2b). Assuming the Maxwell-Boltzmann velocity distribution, the average translational energy of the nascent $N(^4S)$ atoms in the laboratory (LAB) frame was calculated to be ~7500 cm^{-1} (~21 kcal mol^{-1}).

Figure 4.3b shows a photolysis laser power dependence of the LIF signal intensity of $N(^4S)$ atoms produced from the 193 nm laser irradiation of NO_2. A quadratic photolysis laser power dependence of the $N(^4S)$ LIF signal intensity suggests that the $N(^4S)$ formation is attributable to the sequential two-photon dissociation process or the simultaneous absorption of two photons by NO_2.

For the sequential two-photon dissociation process, it is likely that the vibrationally excited $NO(X^2\Pi, v)$ is produced from the photolysis of NO_2 at 193 nm, and then $NO(X^2\Pi, v)$ is photolyzed to produce the $N(^4S)$ atom:

$$NO_2 + h\nu(193\ nm) \rightarrow NO(X^2\Pi, v) + O \qquad (4.4)$$

$$NO(X^2\Pi, v) + h\nu(193\ nm) \rightarrow N(^4S) + O. \qquad (4.5)$$

Gradd and Slanger [36] observed the vibrationally excited NO $X^2\Pi(v = 4\text{-}10)$ in the photodissociation of NO_2 at 193 nm. Gong et al. [22] reported that the nascent vibrational state populations of NO $X^2\Pi(v = 1\text{-}7)$ in the photodissociation of NO_2 at 193 nm have a maximum at v = 5. The average translational energy of $N(^4S)$ estimated in the present study (~21 kcal/mol in the laboratory frame) is consistent with the sequential two-photon dissociation process in which $NO(X^2\Pi, v = 7)$ is formed through channel (4.4).

For the simultaneous two-photon absorption mechanism, it involves the direct formation of $N(^4S)$ from an electronically excited state(s) of NO_2, where the following channels are available thermochemically:

$$NO_2 + 2h\nu(193\ nm) \rightarrow N(^4S) + 2O \qquad (4.6)$$

$$NO_2 + 2h\nu(193\ nm) \rightarrow NO^* + O \rightarrow N(^4S) + O + O \qquad (4.7)$$

$$NO_2 + 2h\nu(193\ nm) \rightarrow N(^4S) + O_2. \quad (4.8)$$

Haak and Stuhl [37] observed the NO emissions from its several excited states ($A^2\Sigma^+$, $D^2\Sigma^+$, and $E^2\Sigma^+$, and so on) following the multiphoton absorption of NO_2 at 193 nm. Further studies are required to elucidate the mechanism of the $N(^4S)$ formation following 193 nm irradiation of NO_2.

4.3.3 Reaction kinetics of $N(^4S)$ + NO and $N(^4S)$ + NO_2

The $N(^4S)$ formation following 193 nm irradiation of NO and NO_2 was applied to the kinetic studies of the reactions (4.1) and (4.2). The pulsed ArF laser light was used to irradiated 150-570 mTorr of NO in the presence of 1.8 Torr of He diluent and the chemical loss of $N(^4S)$ was measured to determine the rate coefficients for the $N(^4S)$ + NO reaction at 295 ± 2 K. Figure 4.4 shows a typical example of the temporal profile of the $N(^4S)$ LIF intensity following pulsed ArF laser irradiation of a mixture of 415 mTorr of NO and 1.8 Torr of He diluent, in which the VUV laser wavelength was fixed at the resonance center of the $N(2p^23s\ ^4P_{1/2} - 2p^3\ ^4S_{3/2})$ transition (120.07 nm). The time-resolved VUV-LIF signal of $N(^4S)$ atoms exhibits an initial jump due to photolytic formation of $N(^4S)$, followed by a slow decay due to its chemical removal in collisions with NO molecules. For the kinetic study of the $N(^4S)$ + NO_2 reaction, the time profiles of the $N(^4S)$ LIF were measured under the conditions of NO_2 60-570 mTorr, O_2 200-1700 mTorr, and He 3.0 Torr. As described in the previous section, the translationally hot $N(^4S)$ atoms are produced following 193 nm irradiation of NO and NO_2. The translationally hot $N(^4S)$ atoms are thermalized within 2 μs under our experimental conditions in collisions with helium, which was confirmed by measuring the Doppler profiles of $N(^4S)$ atoms. The chemical loss of $N(^4S)$ by reaction with O_2 can safely be ignored under our experimental conditions ($[O_2]$ = 200-1700 mTorr, delay time 0-20 μs) because of its small rate constant of 8.5×10^{-17} cm^3 $molecule^{-1}$ s^{-1} at 298 K [27]. For both the reaction systems (4.1) and (4.2), single-exponential decay was observed for temporal profiles of $N(^4S)$ as typically shown in Fig. 4.4:

$$[N(^4S)]_t = [N(^4S)]_0 \times \exp(-k't). \quad (4.9)$$

The pseudo-first-order rate constant k' for a particular reactant pressure was derived by a nonlinear least-squares fit analysis. The resultant dependences of the k' values on the number densities of NO and NO_2 for the $N(^4S)$ + NO and $N(^4S)$ + NO_2 reactions, respectively, are shown in Figure 4.5. Linear least-squares fit analysis of the data in

Fig. 4.5 yielded the bimolecular rate constants of $k_{NO} = (3.8 \pm 0.2) \times 10^{-11}$ and $k_{NO2} = (7.3 \pm 0.9) \times 10^{-12}$ cm^3 $molecule^{-1}$ s^{-1} at 295 ± 2 K. The quoted uncertainties of the rate constants include 2σ statistical uncertainties and estimated systematic errors.

The rate constants for reactions (4.1) and (4.2) at 295 ± 2 K determined in the present study are listed in Table 4.1 with available literature data. The k_{NO} value determined in this study is in excellent agreement with the latest data reported by Wennberg et al. [5] within the quoted uncertainties. Our result is also in good agreement with that of Cheah and Clyne [11] and one of the values reported by Lee et al. [10]. The latest NASA/JPL recommended k_{NO} value at 298 K [27] is smaller than both the values recently reported by Wennberg et al. [5] and obtained in the present study. For the reaction of $N(^4S)$ + NO, the ground potential energy surface (PES) $^3A''$ and the first excited PES $^3A'$ were theoretically investigated by means of complete active space second-order perturbation (CASPT2) method, and the variational transition state theory provided the temperature-dependent rate coefficients [38]. It was shown that the $^3A'$ PES was mainly responsible for the $N(^4S)$ + NO reaction over the temperature range of 200 - 5000 K and their k_{NO} value at 300 K was 4.68×10^{-11} $cm^3molecule^{-1}s^{-1}$. The theoretical value is larger than our experimental and previous determinations.

The k_{NO2} values reported previously range from 0.14 to 3.8×10^{-11} cm^3 $molecule^{-1}$ s^{-1} as listed in Table 4.1. The k_{NO2} value determined in this study is larger than the result of Clyne and Ono [12], and is smaller than that presented by Wennberg et al.[5]. The experimental technique of laser flash photolysis combined with VUV laser-induced fluorescence detection has been utilized for the first time in this study, while Clyne and Ono [12] and Wennberg et al. [5] used the technique of discharge flow and resonance fluorescence detection with a nitrogen lamp. Clyne and McDermid [9] and Clyne and Ono [12] reported that the measured rate constant k_{NO2} decrease as the ratio of $[NO_2]/[N(^4S)]_0$ increase at lower ratios of $[NO_2]/[N(^4S)]_0$ (<80). They argued that the change of the observed rate constant was due to catalytic interferences involving both $H(^2S)$ + NO_2 and $O(^3P)$ + NO_2 reactions, in which $H(^2S)$ and $O(^3P)$ atoms can be produced as impurities in the microwave discharge process and $O(^3P)$ atoms can also be produced through reaction (4.2). In the present study, $N(^4S)$ atoms were produced from the 193 nm pulsed laser irradiation of NO_2, and the ratio of $[NO_2]/[N(^4S)]_0$ was (5 - 20) × 10^5 as estimated by considering the $N(^4S)$ detection sensitivity (2×10^9 atoms cm^{-3}).

It should be noted that, in general, the literature data of the rate coefficients for $N(^4S)$ reactions with simple molecules are more scattered than those of other atmospheric reactions involving atoms such as $O(^1D)$ and $Cl(^2P_j)$ atoms. This might be attributable to the relatively low reactivity of $N(^4S)$ toward the simple molecules and the lack of applicable experimental technique. The newly presented technique for investigation of the $N(^4S)$ reactions with NO and NO_2 will be applicable to examine some other $N(^4S)$ reactions as a function of temperature and pressure. The pulsed laser photolysis/VUV-LIF technique has been utilized as a powerful tool to study the kinetics and dynamics of atmospheric reactions involving $O(^1D)$ and $Cl(^2P_j)$ atoms [39,40].

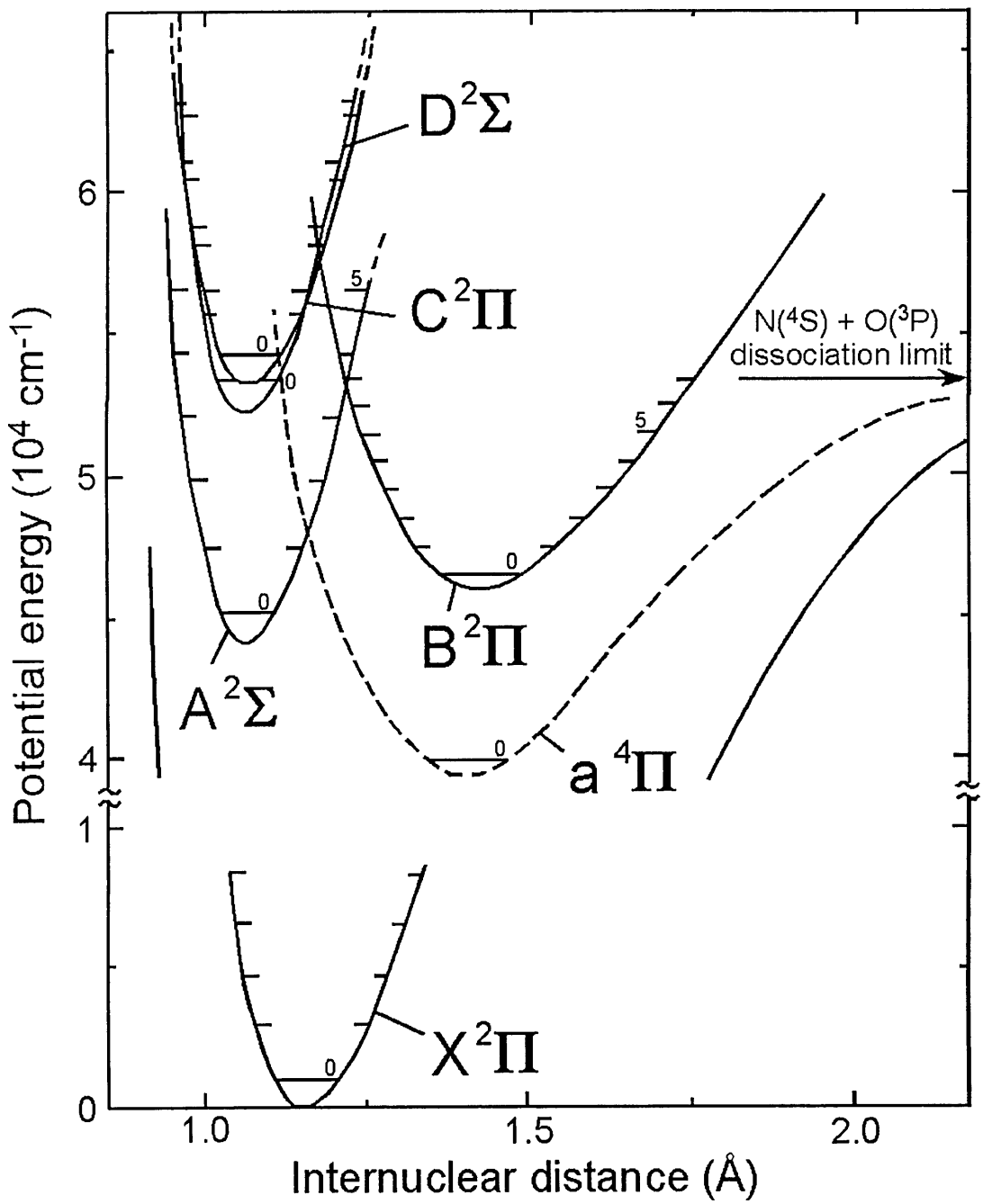

Figure 4.1. Potential energy curves of NO near the dissociation limit into the $N(^4S)$ + $O(^3P)$ products [41].

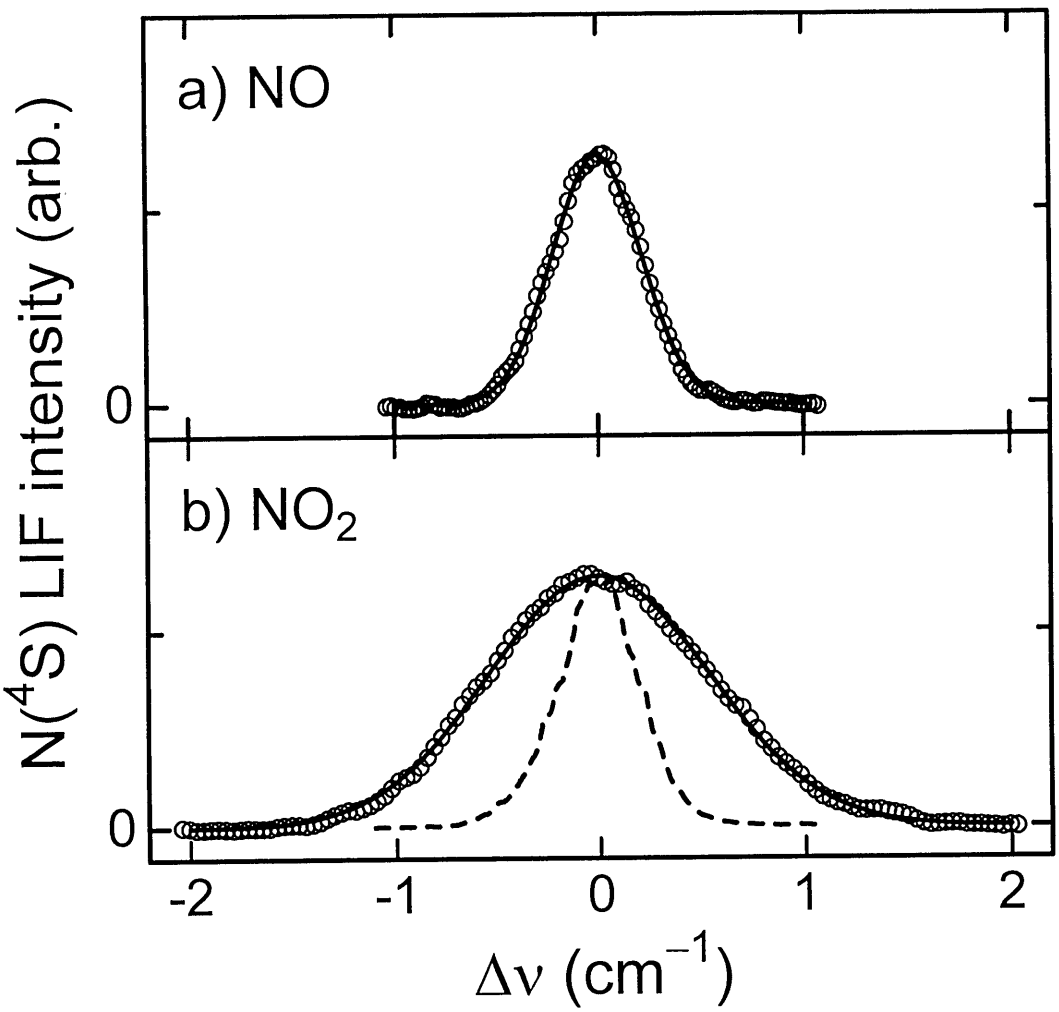

Figure 4.2. Fluorescence excitation spectra of $N(^4S)$ produced from the 193 nm laser irradiation of (a) NO and (b) NO_2, respectively, which were recorded by scanning the probe laser wavelength across the resonance center of the $^4P_{1/2}$ - $^4S_{3/2}$ transition for the $N(^4S)$ atom at 120.07 nm. The solid curves indicate Gaussian shapes that fit the observed spectrum. Spectrum (a) was measured at an 80 ns delay time between the photolysis and probe laser pulses at the pressure of NO 145 mTorr. Spectrum (b) was measured at an 80 ns delay time at the pressures of NO_2 34 mTorr and O_2 82 mTorr. The broken curve shows the fluorescence excitation spectrum of thermalized $N(^4S)$, in which the $N(^4S)$ atom was produced from 193 nm irradiation of NO_2 in the presence of 3.6 Torr of He. The delay time was 5 μs.

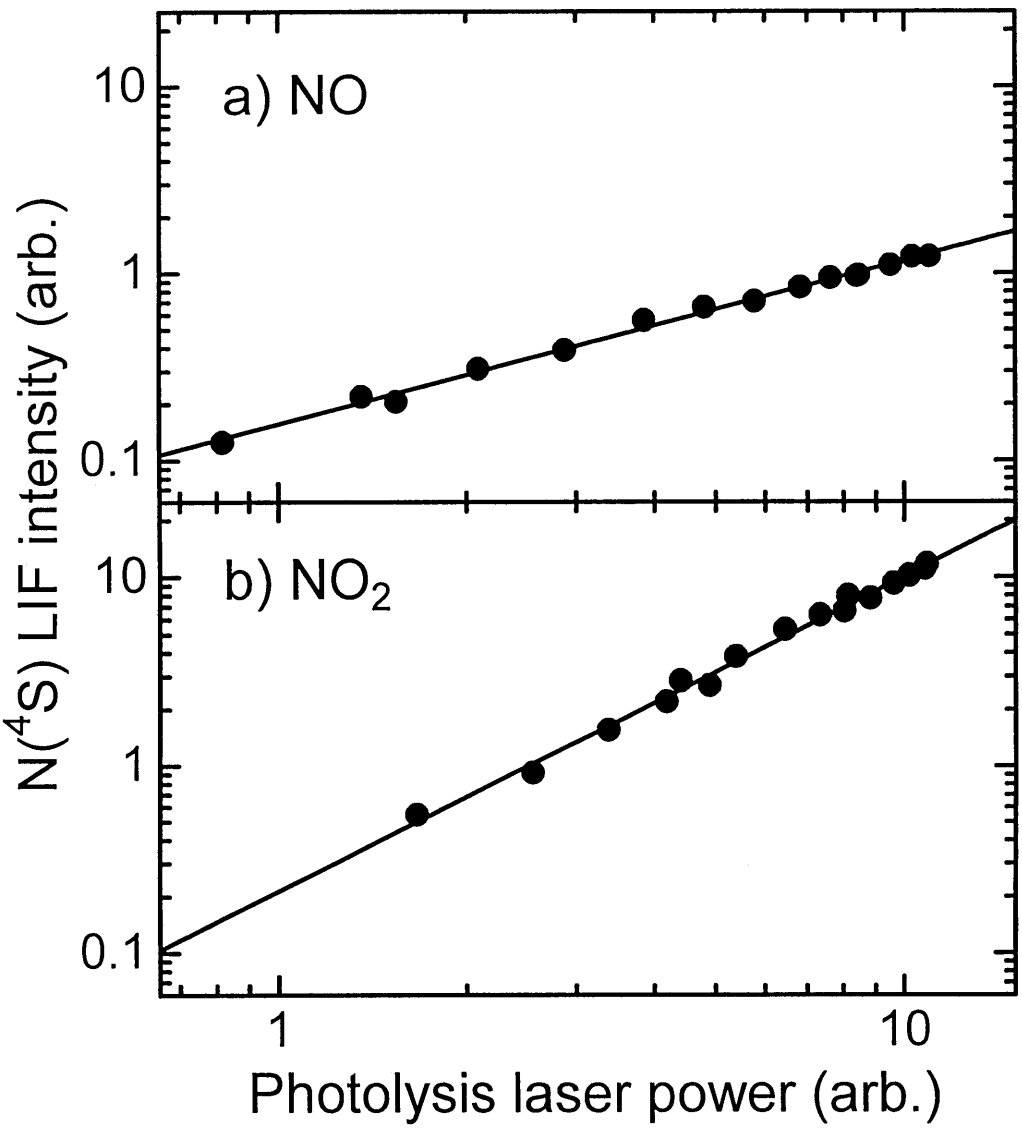

Figure 4.3. Plots of the photolysis laser power dependence of the LIF intensity of $N(^4S)$ produced following 193 nm laser irradiation of (a) NO and (b) NO_2, respectively. The photolysis laser power was varied while monitoring the $N(^4S)$ LIF signal at 120.07 nm. The probe laser power was kept constant during the measurements. Solid lines indicate the results of least-squares fit analysis in order to determine the order n of laser power dependence of the LIF signals. The values obtained for n are (a) 0.9 ± 0.1 and (b) 1.7 ± 0.2, respectively, which are described in the figure. The quoted uncertainties indicate the 2σ errors of the fit.

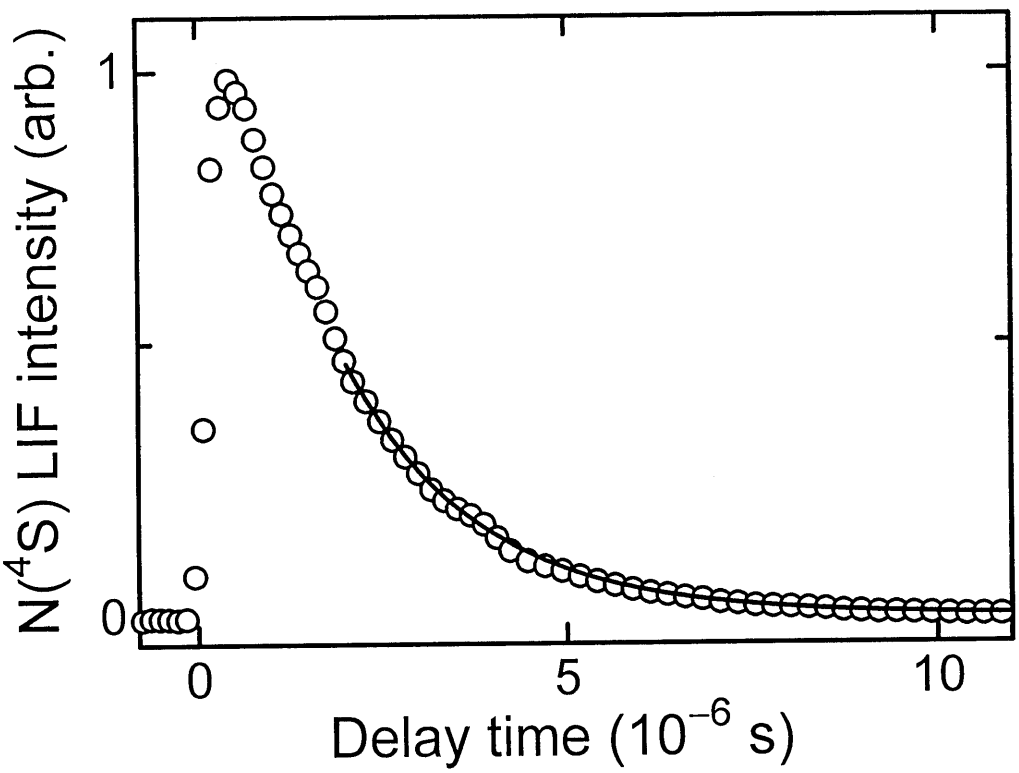

Figure 4.4. A typical example of the temporal decay curve of $N(^4S)$ LIF intensity following the 193-nm pulsed laser irradiation of the gas mixture containing 415 mTorr of NO and 1.8 Torr of He diluent at 295 ± 2 K. The solid curve is a first-order decay fit to the data in the time domain after 2 μs.

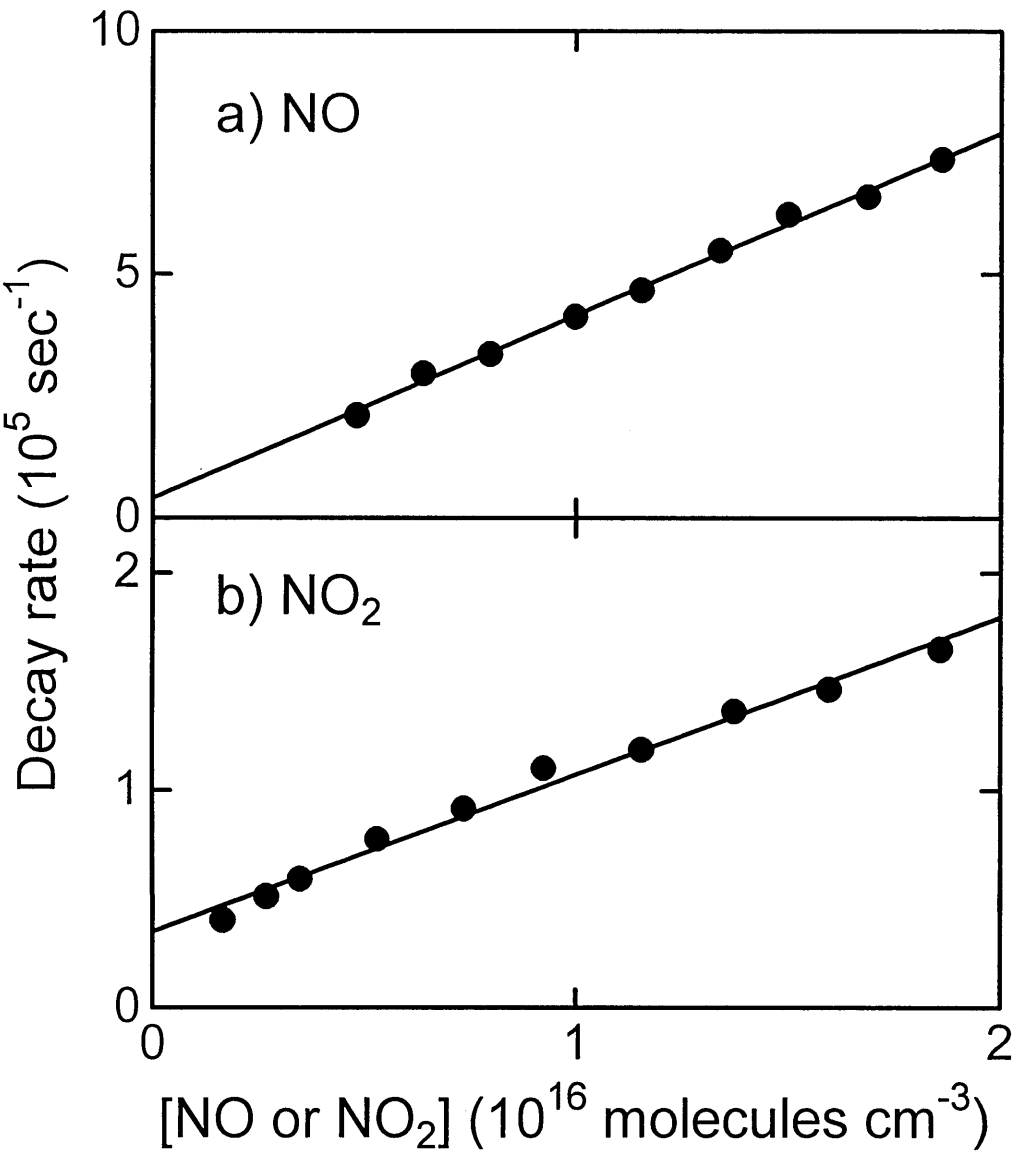

Figure 4.5. Plot of pseudo-first-order decay rates (k') versus the concentration of the reactants (a) NO and (b) NO_2. Results of the least-squares fit analysis of the data are drawn by straight lines, which yield the rate coefficients $(3.8 \pm 0.2) \times 10^{-11}$ and $(7.3 \pm 0.9) \times 10^{-12}$ cm^3 $molecule^{-1}$ s^{-1} at 295 ± 2 K for $N(^4S)$ reactions with NO and NO_2, respectively.

Table 4.1. Summary of the present and previous studies on the reaction kinetics of $N(^4S)$ with NO and NO_2 at room temperature.

Reactant	Rate coefficient [a]	Method [e]	Refs.
NO	1.7 ± 0.8 [b]	DF/MS	Herron (1961) [6]
	2.2 ± 0.6	DF/MS	Philips and Schiff (1962) [7]
	2.2 ± 0.2	DF/MS	Clyne and McDermid (1975) [9]
	2.7 ± 0.4 [c]	DF/RF	Lee et al. (1978) [10]
	4.0 ± 0.2 [c]	FP/RF	Lee et al. (1978) [10]
	1.9 ± 0.2	PR/RA	Sugawara et al. (1980) [16]
	3.4 ± 0.3 [c]	DF/RF	Cheah and Clyne (1980) [11]
	4.5 ± 0.2	FP/RF	Husain and Slater (1980) [15]
	2.77 ± 0.04 [c]	DF/RF	Clyne and Ono (1982) [12]
	2.03 ± 0.17 [c]	DF/MS	Brunning and Clyne (1984) [13]
	2.4 ± 0.2	DF/MS	Jeoung et al. (1991) [14]
	3.6 ± 0.4 [d]	DF/RF	Wennberg et al. (1994) [5]
	3.0	-	NASA/JPL (2003) [27]
	3.8 ± 0.2 [d]	LP/VUV-LIF	This work
NO_2	1.85 ± 0.22 [c]	DF/MS	Philips and Schiff (1965) [8]
	0.14 ± 0.02	DF/MS	Clyne and McDermid (1975) [9]
	3.8 ± 0.1	FP/RF	Husain and Slater (1980) [15]
	0.301 ± 0.033 [c]	DF/RF	Clyne and Ono (1982) [12]
	1.2 ± 0.1 [d]	DF/RF	Wennberg et al. (1994) [5]
	1.2	-	NASA/JPL (2003) [27]
	0.73 ± 0.09 [d]	LP/VUV-LIF	This work

a. In units of 10^{-11} cm^3 $molecule^{-1}$ s^{-1}.

b. The error limits are estimates of 3σ.

c. The error limits are estimates of 1σ.

d. The error limits are estimates of 2σ.

e. Experimental techniques. DF: discharge flow, MS: mass spectrometry. KS: kinetic spectroscopy, RF: resonance fluorescence, FP: flash photolysis, PR: pulsed radiolysis, RA: resonance absorption, LP: laser photolysis, VUV-LIF: vacuum ultraviolet laser-induced fluorescence.

References for Chapter 4

[1] Siskind, D. E; Rusch, D. W., *J. Geophys. Res.*, **97**, 3209 (1992).

[2] Gerard, J. -C., *Planet. Space Sci.*, **40**, 337 (1992).

[3] Nelvison, C. D.; Solomon, S.; Garcia, R. R. *Geophys. Res. Lett.* **1997**, *24*, 803.

[4] Yung, Y. L; DeMore, W. B., *Photochemistry of Planetary Atmosphere*, Oxford University Press, New York, 1999.

[5] Wennberg, P. O., Anderson, J. G., Weisenstein, D. K., *J. Geophys. Res.*, **99**, 18839 (1994).

[6] Herron, J. T., *J. Chem. Phys.*, **35**, 1138 (1961).

[7] Philips, L. F., Schiff, H. I., *J. Chem. Phys.*, **36**, 1509 (1962).

[8] Philips, L. F., Schiff, H. I., *J. Chem. Phys.*, **42**, 3171 (1965).

[9] Clyne, M. A. A., McDermid, I. S., *J. Chem. Faraday. Trans. 1*, **71**, 2189 (1975).

[10] Lee, J. H., Michael, J. V., Payne, W. A., Steif, L. J., *J. Chem. Phys.*, **69**, 3069 (1978).

[11] Cheah, C. T., Clyne, M. A. A., *J. Chem. Soc., Faraday Trans. 2*, **76**, 1543 (1980).

[12] Clyne, M. A. A., Ono, Y., *Chem. Phys.*, **69**, 381 (1982).

[13] Brunning, J., Clyne, M. A. A., *J. Chem. Soc., Faraday. Trans. 2*, **80**, 1001 (1984).

[14] Jeoung, S. C., Choo, K. Y., Benson, S. W., *J. Phys. Chem.*, **95**, 7282 (1991).

[15] Husain, D., Slater, N. K. H., *J. Chem. Soc. Faraday. Trans. 2*, **76**, 606 (1980).

[16] Sugawara, K., Ishikawa, Y., Sato, S., *Bull. Chem. Soc. Jpn.*, **53**, 3159 (1980).

[17] Davidson, D. F., Hanson, R. K., *Int. J. Chem. Kinet*, **22**, 843 (1990).

[18] Koshi, M., Yoshimura, M., Fukuda, K., Matsui, H., Saito, K., Watanabe, M., Imamura, A., Chen, C., *J. Chem. Phys.*, **93**, 8703 (1990).

[19] Atkinson, R., Baulch, D. L., Cox, R. A., Crowley, J. N., Hampson, R. F., Hynes, R. G., Jenkin, M. E., Rossi, M. J., and Troe, J., *Atmos. Chem. Phys.*, **4**, 1461 (2004).

[20] Sun, F.; Glass, G. P.; Curl, R. F. *Chem. Phys. Lett.*, **337**, 72 (2001).

[21] Gradd, G. E.; Slanger, T. G., *J. Chem. Phys.*, **92**, 2194 (1990).

[22] Gong, V. C., Chen, X. R., Weiner, B. R., *5th International Conference on Chemical Kinetics*, National Institute of Standards and Technology, Gaithersburg, MD, USA 2001.

[23] Tsuji, M., Noda, K., Sato, H., Hamagami, T., Tsuji, T., *Chem. Lett.*, **34**, 496 (2005).

[24] Matsumi, Y., Murasawa, Y., Obi, K., Tanaka, I., *Laser Chem.*, **1**, 113 (1983).

[25] Jusinski, L. E., Sharpless, R. L., Slanger, T. G., *J. Chem. Phys.*, **86**, 5509 (1987).

[26] Nagai, H., Kusumoto, T., Shibuya, K., Obi, K., Tanaka, I., *J. Phys. Chem.*, **92**, 5432 (1988).

[27] Sander, S. P., Friedl, R. R., Golden, D. M., Kurylo, M. J., Huie, R. E., Orkin, V. L., Moortgat, G. K., Ravishankara, A. R., Kolb, C. E., Molina, M. J., Finlayson-Pitts, B. J., *Chemical Kinetics and Photochemical Data for use in Atmospheric Studies*, Evaluation No. 14, JPL Publication 02-25, 2003.

[28] Harder, J. W., Brault, J. W., Johnston, P. V., Mount, G. H., *J. Geophys. Res.*, **102**, 3861 (1997).

[29] Vandaele, A. C., Hermans, C., Simon, P. C., Carleer, M., Colin, R., Fally, S., Merienne, M.

F., Jenouvrier, A., Coquart, B., *J. Quant. Spectrosc. Radiat. Trans.*, **59**, 171 (1998).

[30] Gierczak, T., Burkholder, J. B., Ravishankara, A. R., *J. Phys. Chem.*, **A103**, 877 (1999).

[31] Rottke, H., Zacharias, H., *J. Chem. Phys.*, **83**, 4831 (1985).

[32] Shibuya, K., Stuhl, F., *J. Chem. Phys.*, **76**, 1184 (1982).

[33] Shibuya, K., Stuhl, F., *Chem. Phys.*, **79**, 367 (1983).

[34] Shibuya, K., Stuhl, F., *Chem. Phys.*, **94**, 167 (1985).

[35] Gilmore, F. R., *J. Quant. Spectrosc. Radiat. Transfer*, **5**, 369 (1965).

[36] Gradd, G. E., Slanger, T. G., *J. Chem. Phys.*, **92**, 2194 (1990).

[37] Haak, H. K, Stuhl, F., *J. Photochem.*, **17**, 69 (1981).

[38] Gamallo, P., Gonzalez, M., Sayos, R. *J. Chem. Phys.*, **119**, 2545 (2003).

[39] Takahashi, K., Takeuchi, Y., Matsumi, Y., *Chem. Phys. Lett.*, **410**, 196 (2005), and references therein.

[40] Taketani, F., Takahashi, K., Matsumi, Y., Wallington, T. J., *J. Phys. Chem.*, **A105**, 3935 (2005), and references therein.

[41] Tsukiyama, K., Munakata, T., Tsukakoshi, M., Kasuya, T., *Chem. Phys.*, **121**, 55 (1988).

Chapter 5

Translational relaxation of suprathermal $N(^4S)$ atoms in the upper atmosphere

5.1 Introduction

Observations of NO density in the thermosphere have lead to a need to reevaluate the production processes of NO in the thermosphere, because significant discrepancy between the observed abundance and modeled estimation for NO has been identified [1,2,3]. In 1983, Solomon [4] proposed that chemical reaction of translationally hot $N(^4S)$ atoms with O_2 molecules could be a new source of lower thermospheric NO:

$$\text{fast } N(^4S) + O_2 \rightarrow NO + O. \qquad (5.1)$$

The $N(^4S) + O_2$ reaction has a large activation energy of ~0.24 eV (= 5.5 kcal mol^{-1}) [5] which results in a negligibly small rate coefficient at typical temperatures encountered in the lower thermosphere. The suprathermal $N(^4S)$ atoms produced in the lower thermosphere may react with O_2 to form NO at an energy dependent rate which is considerably lager than that at thermal equilibrium for ambient temperatures [e.g. 4].

Since then, model calculations have extensively been performed to evaluate the translational energy distributions of $N(^4S)$ and the formation efficiency of NO through reaction (5.1) under suprathermal collisions in the thermosphere [4,5,6,7,8,9,10]. The suprathermal nitrogen atoms in the thermosphere can be produced by a number of processes including dissociative recombination of NO^+, collisional quenching of electronically excited $N(^2D)$ atoms and photodissociation and photoelectron impact dissociation of N_2. Then, those hot atoms are relaxed by collisions with N_2 and O_2 molecules in the ambient air. In the model calculations of the steady-state translational energy distributions of $N(^4S)$ atoms in the thermosphere [4,5,6,7,8,9,10,11,12,13,14], the thermalization rates in collisions with N_2 and O_2 molecules are crucial. However, no laboratory study determining experimentally the thermalization cross sections of suprathermal $N(^4S)$ atoms in collisions with ambient gases has been reported.

$$\text{fast } N(^4S) + N_2 \rightarrow \text{slow } N(^4S) + N_2 \qquad (5.2)$$

$$\text{fast } N(^4S) + O_2 \rightarrow \text{slow } N(^4S) + O_2 \qquad (5.3)$$

In the model calculations, the cross section that estimated from diffusion studies of $N(^4S)$ in N_2 [4,11,12,15] or that computed using quantum mechanical (QM) and classical trajectory (QCT) methods [8,9,13,14] have been utilized. The lack of precision in the thermalization cross sections results in a significant uncertainty in the model calculations for the formation rate of NO through reaction (5.1).

In the present study, the first experimental determination of the collisional relaxation rates of suprathermal $N(^4S)$ in collisions with N_2, O_2, He and Ar has been reported. A small amount of NO_2 diluted in an excess amount of bath gases (N_2, O_2, He and Ar) is photolyzed at 193 nm, and the suprathermal $N(^4S)$ atoms produced are detected by a technique of VUV-LIF. Measurements of time-resolved Doppler profiles of the suprathermal $N(^4S)$ atoms enable us to evaluate the time-dependent translational energy distributions of the $N(^4S)$ atoms in bath gas. From the experimental results and Monte-Carlo calculations based on an elastic hard-sphere model, the collision radii between $N(^4S)$ and the bath gas molecules are determined.

5.2 Experimental

The details of the apparatus used in the present study are shown in Chapter 2 and here only a description related to this chapter will be given. All the experiments were performed under bulb conditions at 295 ± 3 K, in which gas mixtures of a small amount of NO_2 diluted in bath gas (N_2, O_2, He or Ar) were slowly introduced into a reaction chamber. The translationally hot $N(^4S)$ atoms were produced by 193 nm pulsed ArF laser photolysis of NO_2 (see Chapter 4). The density of the hot $N(^4S)$ atoms produced by the laser photolysis was 10^9-10^{10} atoms cm^{-3}, which was much smaller than that of bath gas (10^{16} molecules cm^{-3}). The time widths of the photolysis laser and probe laser pulses were ~15 ns and ~10 ns, respectively. The delay time between the photolysis and probe laser pulses was set to 30 ns - 5 μs, which was controlled by a digital delay generator (Stanford Research, DG535).

5.3 Experimental results

The Doppler profiles of $N(^4S)$ atoms were recorded by scanning the probe laser wavelength across the resonance center at various delay times between the photolysis ArF laser and probe VUV laser pulses. The Doppler profiles reflect the distribution of the velocity component of $N(^4S)$ atoms along the propagation direction of the probe

VUV laser [16]. We first recorded the Doppler profiles at 50 ns delay time with 11 mTorr of NO_2 without any bath gas under two geometrical laser beam conditions of $k_p//E_d$ and $k_p \perp E_d$, where k_p and E_d are the propagation direction vector of the probe VUV laser and the polarization vector of the photolysis laser, respectively. The profiles provide the nascent translational energy of $N(^4S)$ produced from NO_2 photolysis, because the relaxation is negligible under those conditions. We did not observe any difference in the Doppler line shapes between two configurations, which indicates the direction of the recoil velocities in the NO_2 photolysis is isotropic.

Figure 5.1 shows typical Doppler profiles of $N(^4S)$ atoms at various delay times in each bath gas of N_2 and O_2. The Doppler width becomes narrower at longer delay times due to relaxation of the fast translational speed of $N(^4S)$ atoms by collisions with the buffer gas, as shown in Fig. 5.1. After the delay time of 1 μs, no significant change in the Doppler profiles was observed. This indicates that the translational distribution of $N(^4S)$ was entirely thermalized to that at ambient temperature (295 K). The VUV laser linewidth was estimated to be 0.40 cm^{-1} (FWHM) with a Gaussian shape from the Doppler profiles of entirely thermalized $N(^4S)$ atoms. It was found that all the profiles at any delay times were well reproduced by Gaussian shapes. A Gaussian line shape corresponds to an isotropic Maxwellian distribution of velocities. The average translational energy of $N(^4S)$ atoms in the LAB flame, $\langle E_t \rangle$, was calculated from the Gaussian Doppler shape, using the following expression [16]:

$$\langle E_t \rangle = \frac{3}{16 \ln 2} \left(\frac{\Delta \nu}{\nu_0} \right)^2 mc^2, \qquad (5.2)$$

where $\Delta\nu$ is the FWHM of the Gaussian shape fitted to the Doppler profile, ν_0 is the resonance center frequency, m is the mass of nitrogen atom, c is the speed of light. The initial $\langle E_t \rangle$ value at $t = 0$ was 0.93 ± 0.10 eV (21.4 ± 2.2 kcal mol^{-1}), which was calculated from the $N(^4S)$ Doppler profile recorded at 50 ns delay time without bath gas.

Figure 5.2a shows the average translational energy of $N(^4S)$ atoms in the LAB frame, $\langle E_t \rangle$, as a function of delay time, when the bath gas was 1.0 Torr of O_2. The relative concentrations of $N(^4S)$ as a function of delay time were also revealed by integrating the peak area of Doppler profile. The $N(^4S)$ concentration at each delay time was normalized with that at delay time of 400 ns. The time-dependent relative concentration of $N(^4S)$ atoms in 1.0 Torr of O_2 thus obtained is plotted in Fig. 5.2b

(open circles). For comparison, the time-dependent concentration of $N(^4S)$ atoms in 1.0 Torr of Ar is also plotted in Fig. 5.2b (open triangles).

The center-of-mass collision energy between hot $N(^4S)$ and O_2 bath gas molecule is roughly calculated to be 32/46 E_t, where E_t is the translational energy of $N(^4S)$ atoms in the LAB frame. In the delay times range shorter than 100 ns, about one-third of collisions between $N(^4S)$ and O_2 are estimated to have center-of-mass collision energies higher than the activation energy for reaction (5.1), ~0.24 eV (= 5.5 kcal mol^{-1}). However, as shown in Fig. 5.2b, no notable decrease was observed for $N(^4S)$ concentrations in O_2 gas even in the short delay time range, compared with the concentration of $N(^4S)$ atoms in Ar gas. This may be due to much smaller cross sections for reaction (5.1) at the center-of-mass collision energies of about 0.24 - 0.6 eV than the translational relaxation cross section.

5.4 Model calculations for hard sphere collision radii

The collisional relaxation of suprathermal $N(^4S)$ atoms was simulated using an elastic hard-sphere collision model with a Monte Carlo method. Using this model calculation method, we previously studied the collisional relaxation of suprathermal $O(^1D)$ [17,18]. The experimental results for translational relaxation of suprathermal $O(^1D)$ in collisions with bath gases of N_2 and O_2 molecules and rare gas atoms were successfully reproduced by the simulation. Detail of the simulation was described in our previous paper [19]. Therefore, the simulation procedure is only briefly explained here. The velocity of $N(^4S)$ atoms at $t = 0$ for each trajectory is generated randomly so that it has the nascent distribution obtained from the Doppler profile. The velocity of the bath gases is generated randomly for every collision so that it has a Maxwellian distribution at 295 K. The maximum impact parameter, b_{max}, is equal to the hard-sphere radius, $d=r(N)+r(\text{bath gas})$, which has been taken as a parameter to fit the simulation to the experimental values of $<E_t>$. The impact parameters, azimuthal angles, and collision interval time for every collision are also generated randomly with their respective appropriate weight functions. The velocity of $N(^4S)$ after every collision with those randomly generated conditions is calculated. The trajectory of each $N(^4S)$ atom is calculated for sequential collisions until the time exceeds 1000 ns under the condition of 1.0 Torr of bath gases, that is, 1000 ns·Torr. After calculations of up to 50000 trajectories, the translational energy distribution of $N(^4S)$ in the LAB

frame was obtained at each delay time up to 1000 ns·Torr.

Figure 5.3 shows a comparison between the experimental results and model calculations for the $\ln[(\langle E_t(t)\rangle - \langle E_t^{th}\rangle) / (\langle E_t(0)\rangle - \langle E_t^{th}\rangle)]$ values as a function of delay time, where $\langle E_t(t)\rangle$ is the average translational energy of $N(^4S)$ in the LAB frame at delay time t, $\langle E_t(0)\rangle$ is the average nascent translational energy of $N(^4S)$ formed in the photolysis of NO_2 at 193 nm and $\langle E_t^{th}\rangle$ is the average thermal energy at 295K. Open circles are results of the Doppler profile measurements. Solid curves are simulated ones with the hard sphere collision model. The best-fit values for hard-sphere collision radii were (3.2 ± 0.2), (3.0 ± 0.2), (2.4 ± 0.1), and (2.7 ± 0.1) Å for $N(^4S) + N_2$, O_2, He and Ar, respectively. The thermalization cross section values (πd^2) were determined to be (3.2 ± 0.4), (2.8 ± 0.4), (1.8 ± 0.2) and (2.3 ± 0.2) in units of 10^{-15} cm^2 for the bath gas of N_2, O_2, He and Ar, respectively. In these model calculations only elastic collisions were taken into account, although the relaxation process can include energy transfer to the internal degrees of freedom when the collision partner is the molecule (N_2 and O_2). Therefore, the obtained hard-sphere radii for these molecules are effective values. The value obtained in the present study for $N(^4S) + N_2$ collision is slightly smaller than that estimated from molecular diffusion coefficients (3.5×10^{-15} cm^2) [15]. Kharchenko et al. [13] compared the energy distribution functions of $N(^4S)$ atoms calculated using the thermalization cross sections obtained from the QM calculation and hard sphere approximation for $N(^4S) + O(^3P)$. They suggested that usage of the hard sphere collision cross section of 6×10^{-15} cm^2 provided an excellent approximation to reproduce the energy distribution function calculated using the QM cross section. This value is larger than those obtained in the present study for collisions with N_2, O_2, Ar and He.

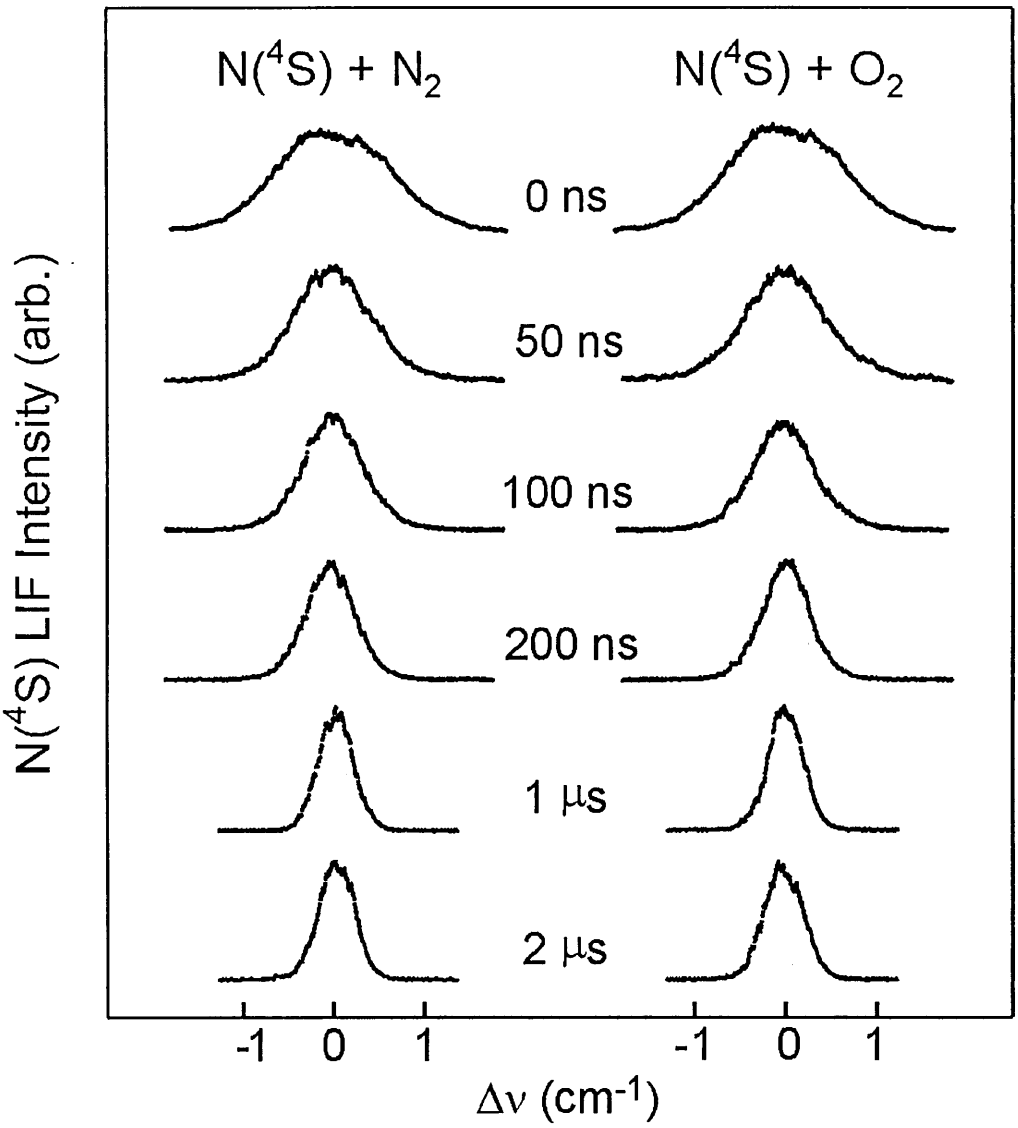

Figure 5.1. Doppler profiles of $N(^4S)$ atoms at various delay times between the NO_2 photolysis and $N(^4S)$ detection laser pulses. The peak heights of the profiles are normalized. The relaxation agents are N_2 and O_2. Pressures of NO_2 and N_2 (or O_2) in the chamber were 11 mTorr and 1.0 Torr, respectively. The Doppler profile at delay time $t = 0$ was actually recorded at $t = 50$ ns without bath gas.

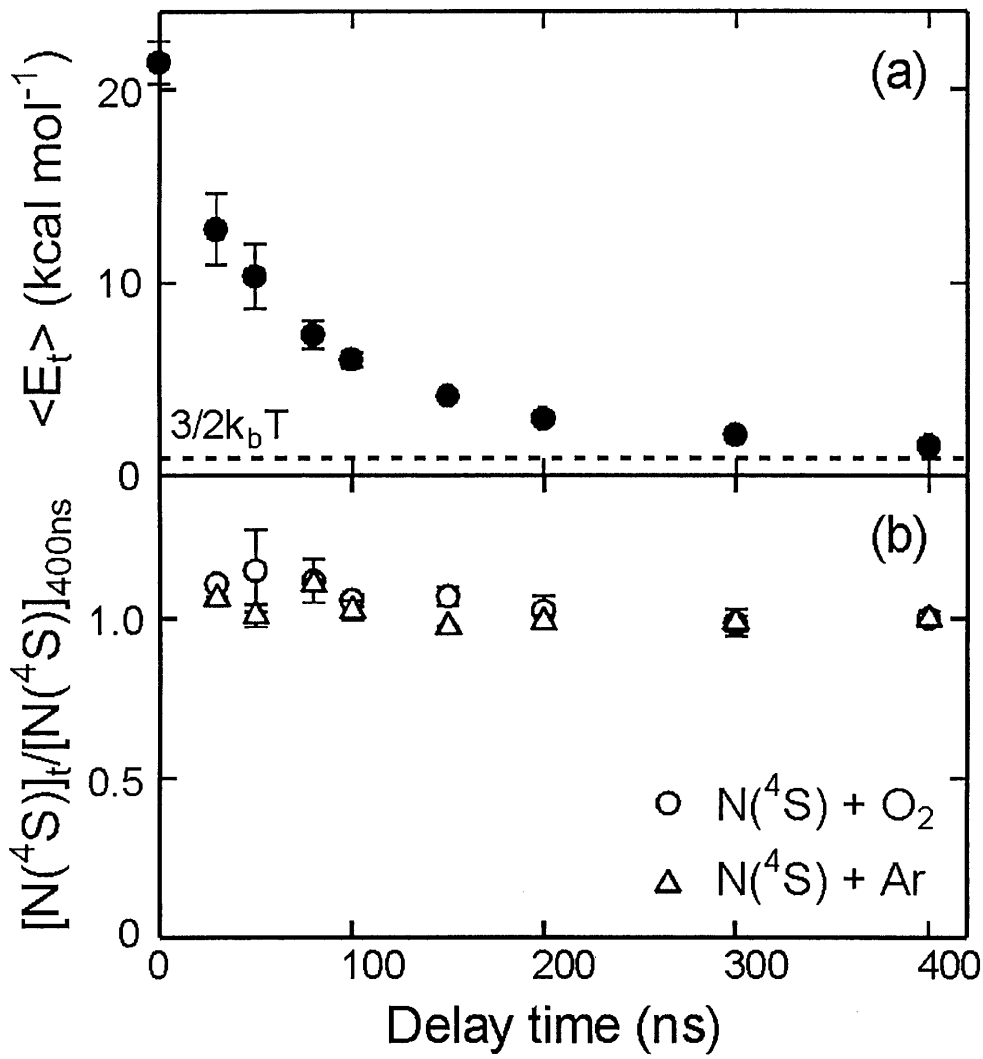

Figure 5.2. (a): Time evolution of the average translational energy, $\langle E \rangle_t$, in the LAB frame for the N(^{4}S) atoms produced from the photolysis of NO_2 at 193 nm. The value of $\langle E_t \rangle$ at each delay time was obtained from the analysis of the Doppler profiles, which were taken under the conditions of 11 mTorr of NO_2 and 1.0 Torr of O_2. Filled circles are the results of the Doppler profile measurements. The broken line indicates the thermal translational energy at 295 K, that is, $(3/2)k_BT$ = 0.89 kcal mol^{-1}. (b): Time evolution of the concentration for the N(^{4}S) atoms when the bath gas is 1.0 Torr of O_2 (open circles) and 1.0 Torr of Ar (open triangles). The vertical scale is normalized by the N(^{4}S) concentration at delay time of 400 ns. Error bars indicate 1σ values of the measurements.

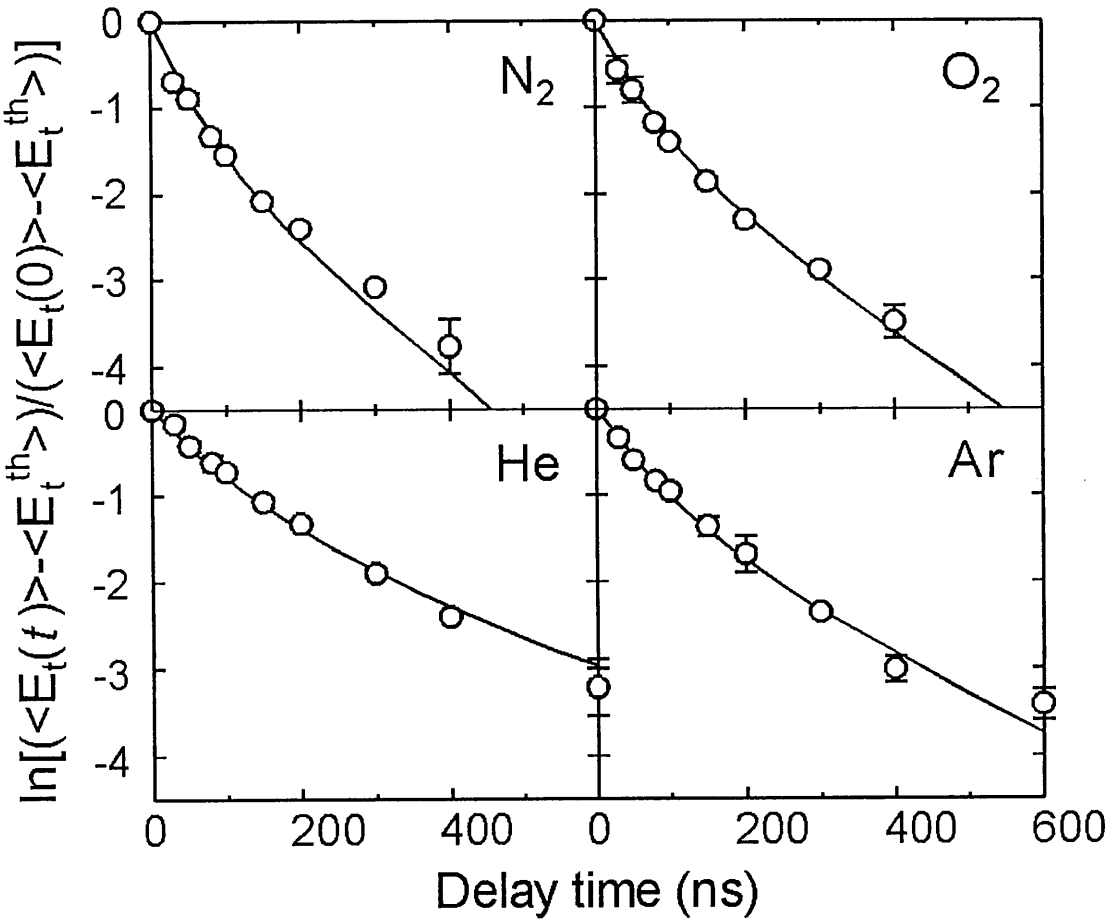

Figure 5.3. Semi-logarithmic plots of the translational energy ratios, $\ln[(\langle E_t(t)\rangle - \langle E_t^{th}\rangle) / (\langle E_t(0)\rangle - \langle E_t^{th}\rangle)]$, versus delay time between the NO_2 photolysis and $N(^4S)$ detection, where $\langle E_t(t)\rangle$ is the average translational energy of $N(^4S)$ at delay time t, $\langle E_t(0)\rangle$ is the average nascent translational energy in the photolysis of NO_2 at 193 nm and $\langle E_t^{th}\rangle$ is the average thermal energy at 295 K. Open circles are the results of the Doppler profile measurements. Solid curves are simulated ones using the hard sphere collision model with best-fit hard-sphere collision radii (see text). The pressure of each bath gas was 1.0 Torr. Error bars indicate 1σ values of the measurements.

References for Chapter 5

[1] Clancy R. T., Rusch D. W., Muhlmann, *Geophys. Res. Lett.*, **19**, 261 (1992).

[2] Suskind, D. E., Strickland, D. J., Meier, R. R., Tajeed, T., Eparvier, F. G., *J. Geophys. Res.*, **100**, 19,687 (1995).

[3] Barth, C. A., Farmer, C. B., Suskind, D. E., Perich, J. P., *J. Geophys. Res.*, **101**, 12489 (1996).

[4] Solomon, S., *Planet. Space Sci.*, **31**, 135, (1983).

[5] Lie-Sevendsen, O., Rees, M., Stamnes, K, Whipple, E. C., *Planet. Space Sci.*, **39**, 929, (1991).

[6] Schematovich, V. I., Bisikalo, D. V., Gérard, J. C., *Geophys. Res. Lett.*, **18**, 1691 (1991).

[7] Gérard, J.C., Bisikalo, D. V., Shematovich, V. I., Duff, J. W., *J. Geophys. Res.*, **102**, 285, (1997).

[8] Dothe, H., Sharma, R. D., Duff, J. W., *Geophys. Res. Lett.*, **24**, 3233 (1997).

[9] Swaminathan, P. K., Strobel, D. F., Kupperman, D. G., Krishna Kumar, C., Acton, L., DeMajistre, R., Yee, J. H., Paxton, L., Anderson, D. E., Strickland, D. J., Duff, J. W., *J. Geophys. Res.*, **103**, 11579 (1998).

[10] Balakrishnan, N., Sergueeva, E., Kharchenko, V., Dalgarno, A., *J. Geophys. Res.*, **105**, 18549 (2000).

[11] Schematovich, V. I., Bisikalo, D. V., Gérard, J. C., *Ann. Geophys.*, **10**, 792 (1992).

[12] Sharma, R. D., Kharchenko, V., Sun, Y., Dalgarno, A., *J. Geophys. Res.*, **101**, 275 (1996).

[13] Kharchenko, V., Tharamel, J., Dalgarno, A., *J. Atmos. Solar. Terr. Phys.*, **59**, 107 (1997).

[14] Kharchenko, V., Balakrishnan, N., Dalgarno, A., *J. Atmos. Solar. Terr. Phys.*, **60**, 95 (1998).

[15] Morgan, J. E., Schiff, H. J., *Can. J. Chem.*, **47**, 2300 (1964).

[16] Zare, R. N., Herschback, D. R., *Proc. IEEE*, **51**, 173 (1963).

[17] Matsumi, Y., Chowdhury, A. M. S., *J. Chem. Phys.*, **104**, 7036 (1996).

[18] Taniguchi, N., Hirai, K., Takahashi, K., Matsumi, Y., *J. Phys. Chem.*, **A104**, 3894 (2000).

[19] Matsumi, Y., Shamsuddin, S. M., Sato, Y., Kawasaki, M., *J. Chem. Phys.*, **101**, 9610 (1994).

Chapter 6

Photochemical reaction processes of $O(^1S)$ and their implications for OH productions and airglow

6.1 Introduction

The photochemical processes of $O(^1S)$ atom play an important role in chemical physics and atmospheric chemistry [1]. For instance, production of the $O(^1S)$ atoms and their chemical reactions in the upper terrestrial atmosphere have known to be related to airglow phenomena [2,3,4].

There are two energetically possible pathways for $O(^1S)$ formation from O_3 photoysis around 200 nm:

$$O_3 + h\nu \rightarrow O(^1S) + O_2(X^3\Sigma_g^-) \qquad (\lambda < 234 \text{ nm}) \qquad (6.1a)$$

$$\rightarrow O(^1S) + O_2(a^1\Delta_g) \qquad (\lambda < 196 \text{ nm}). \qquad (6.1b)$$

Channel (6.1a) is a spin-forbidden process, while channel (6.1b) is a spin-allowed one. Experimental studies have shown that $O(^1D)$ and $O(^3P)$ atoms are the major atomic oxygen products and that $O(^1S)$ is the minor one in the UV photolysis of O_3 around 200 nm [5,6,7,8,9]. Nishida *et al.* [9] have recently determined the $O(^1D)$ quantum yield from O_3 photolysis as a function of photolysis wavelength between 193 and 225 nm, and reported a monotonic decrease in the $O(^1D)$ quantum yield values from 225 nm to 193 nm. No information is available on the photolysis wavelength dependence of the quantum yield of $O(^1S)$ formation from UV photolysis of O_3 around 200 nm. Lee *et al.* [5] photolyzed O_3 molecules at 170 - 240 nm using the synchrotron radiation and tried to detect the $O(^1S)$ atoms by observation of the 557.7-nm emission. They observed no discernible emission, and reported an upper limit value of the quantum yield for $O(^1S)$ formation (≤ 0.1 %).

The $O(^1S)$ formation from N_2O photolysis at 193 nm is energetically possible through the pathway:

$$N_2O + h\nu \rightarrow O(^1S) + N_2 \qquad (\lambda < 211 \text{ nm}). \qquad (6.2)$$

Photodissociation products from N_2O around 200 nm have been studied in detail, and the quantum yields for $O(^1D)$, $O(^3P)$, and $N(^4S)$ productions are >0.95, $(5 \pm 2) \times 10^{-3}$, $(2.1 \pm 0.9) \times 10^{-3}$ [1,10,11,12,13,14], respectively. Felder *et al.* [11] reported an upper

limit value of the quantum yield for $O(^1S)$ formation from 193 nm photolysis of N_2O molecular beam to be ≤ 0.04.

The $O(^1S)$ formation from H_2O_2 photolysis at 193 nm is energetically possible through the pathway:

$$H_2O_2 + h\nu \rightarrow O(^1S) + H_2O \qquad (\lambda < 213 \text{ nm}). \qquad (6.3)$$

The IUPAC subcommittee on gas kinetics data evaluation reviewed the available literature data [15,16,17] on the photodissociation processes of H_2O_2 at 193 nm and recommends the quantum yields 1.70 and 0.15 for OH radical and H atom formation, respectively [18]. An upper limit value for $O(^1S)$ formation was reported to be <0.02 based on the kinetic measurements [16].

Kinetic studies on the reactions of $O(^1S)$ with small molecules such as H_2, O_2, CO, CO_2, N_2O, O_3, H_2O, SF_6, hydrocarbons, and chlorofluoromethanes, have been performed by several groups [19,20,21,22,23,24,25,26,27,28,29,30,31,32,33,34,35,36] and reviewed by Schofield [37]. In previous studies, $O(^1S)$ atoms were generated from VUV photolysis of N_2O or CO_2 using a pulsed atomic resonance lamp and time resolved kinetic measurements were achieved by detecting the emission of the $O(^1S - ^1D)$ transition at 557.7 nm. High pressure of rare gas (mostly Ar) was sometimes added in the reaction system to intensify the green emission through the exciplex formation between the rare gas and $O(^1S)$ atom. Electron-beam irradiation of a gas mixture of O_2 in high-pressure Ar was also utilized as a source of $O(^1S)$ to study the reaction of $O(^1S)$ with H_2O, in which the 557.7 nm emission was monitored to detect $O(^1S)$ [30].

In the present study, the formation of $O(^1S)$ in the photolysis of O_3 at 193, 215 and 220 nm and that for N_2O and H_2O_2 at 193 nm have been investigated, using the VUV-LIF spectroscopy technique. The quantum yields of $O(^1S)$ in the photolysis of O_3 at 193, 215 and 220 nm have been determined. The quantum yield measurements have been made by comparing the VUV-LIF signal intensity of $O(^1S)$ with the that of $H(^2S)$ atom produced in the 193 nm photolysis of HCl, in which the H atom fluorescence has been detected by the same VUV-LIF method at 121.56 nm. The upper limits of the formation yields of $O(^1S)$ from the photolysis of N_2O and H_2O_2 at 193 nm have also been reported. The room-temperature rate constants for the reactions $O(^1S) + O_2$, CO_2, H_2O, O_3, and HCl have been determined by applying the pulsed laser photolysis / VUV-LIF detection technique. The atmospheric implications

of those experimental results on the OH radical production and terrestrial airglow emission have been discussed.

6.2 Experimental

The details of the apparatus used in the present study are shown in Chapter 2 and here only a description related to this chapter will be given. The $O(^1S)$ atoms produced from O_3 photolysis at 193, 215 and 220 nm were probed by the VUV-LIF method at 121.76 nm, which is resonant with the electronic transition of $O(3s\ ^1P_1 \leftarrow 2p\ ^1S_0)$. The $H(^2S)$ atoms produced from HCl photolysis at 193, 215 and 220 nm were detected by the VUV-LIF technique at 121.56 nm (Lyman-α), which is associated with electric transition of $H(2p\ ^2P_j \leftarrow 1s\ ^2S)$. The tunable VUV laser radiation around 121.56 nm was also obtained with the same experimental setup for the VUV laser system with the Kr/Ar cell and the fluorescence detection system.

The O_3 molecules were prepared by passing the ultra-pure O_2 molecules (>99.9995%, Nagoya Kosan) through a commercial ozonizer. The number density of O_3 molecules in the reaction chamber was determined by absorption spectrometry at 253.7 nm using a mercury penray lamp. Commercially obtained N_2O (> 99.9%, Takachiho Co.) gas was used in the experiments without further purification. Aqueous hydrogen peroxide solution (30 % w/v, Wako) was gently distilled under vacuum and stored in a glass bulb. The concentration of H_2O_2 was estimated to be > 97 % from the absorption measurements at 193 and 210 nm based on the reported absorption cross-sections [12].

For the kinetic reaction experiments, gas mixtures of O_3 and reactants were introduced slowly into the reaction chamber which was continuously evacuated by a rotary pump through a liquid N_2 trap. $O(^1S)$ atoms were generated by O_3 photolysis at 193 nm (channel 6.1). We estimate the initial concentration of $O(^1S)$ produced photolytically to be in the range of $(2 - 12) \times 10^{10}$ atoms cm^{-3}, which was estimated from the reported absorption cross section of O_3 (4.34×10^{-19} $cm^2 molecule^{-1}$) [34], the $O(^1S)$ quantum yield from O_3 photolysis at 193 nm ($(2.5 \pm 1.1) \times 10^{-3}$) [33], the photolysis laser fluence (9.6×10^{16} photons cm^{-2}), and the O_3 concentration (7-36 mTorr). The partial pressures of reactant gases were 4 - 32 Torr (O_2), 7 - 36 Torr (CO_2), 5 - 48 mTorr (H_2O), 2 - 12 mTorr (O_3), and 3 - 54 mTorr (HCl). The HCl (> 99.9%, Sumitomo Seika) and CO_2 (> 99.99%, Showa Tansan) gases were obtained

commercially and were used without further purification. The distilled water was used after freeze-pump-thaw cycles. All experiments were performed at 295 ± 2 K.

6.3 Results and discussion

6.3.1 Quantum yields for $O(^1S)$ formation from O_3 photolysis at 193, 215, and 220 nm

Figure 6.1 shows the fluorescence excitation spectra for $O(^1S)$ and $H(^2S)$ atoms produced in the 193 nm photolysis of O_3 and HCl, respectively. The atomic line profiles of the $O(3s^1P_1 \leftarrow 2p^1S_0)$ transition were directly detected by VUV-LIF method around 121.76 nm, while those of the $H(2p^2P_j \leftarrow 1s^2S)$ transition were detected at 121.56 nm. Checks were made to ensure that the $O(^1S)$ LIF signal intensity was linearly dependent on the photolysis laser power as shown in Figure 6.2. We also confirmed that neither $O(^1S)$ nor H atoms' signal was observed without 193 nm photolysis light. Figure 6.3 shows the fluorescence excitation spectrum for the $O(^1S)$ atoms produced in the photolysis of O_3 at 215 and 220 nm. The quantum yields for $O(^1S)$ formation in the O_3 photolysis at wavelength λ, $\Phi_{O1S}^{O3}(\lambda)$, have been determined by comparing the VUV-LIF intensities for $O(^1S)$ and H atoms produced in the photolysis of O_3 and HCl, respectively. Since the photolysis of HCl at 193, 215, and 220 nm provides H atoms with a quantum yield of unity [12], the absolute quantum yields for $O(^1S)$ formation, Φ_{O1S}^{O3}(193 nm), Φ_{O1S}^{O3}(215 nm), and Φ_{O1S}^{O3}(220 nm), were obtained by the following equation:

$$\Phi_{O(1S)}^{O3}(\lambda) = \frac{S_{O(1S)}(\lambda) I_H f_H \sigma_{HCl}(\lambda) [HCl] \phi_H}{S_H(\lambda) I_{O(1S)} f_{O(1S)} \sigma_{O3}(\lambda) [O_3] \phi_{O(1S)}} \times 1,$$

(at λ = 193, 215, and 220 nm) (6.4)

where $S_{O(1S)}(\lambda)$ and $S_H(\lambda)$ are the peak areas of the fluorescence excitation spectra of the $O(^1S)$ and H atoms in the photolysis of O_3 and HCl, respectively. $I_{O(1S)}$ and I_H are the probe laser intensities at the resonance wavelengths of $O(^1S)$ (121.76 nm) and H atoms (121.56 nm), respectively. $f_{O(1S)}$ and f_H are the transition probabilities for $O(3s^1P_1 \leftarrow 2p^1S_0)$ and $H(2p^2P_j \leftarrow 1s^2S)$ optical excitation, respectively. $\sigma_{O3}(\lambda)$ and $\sigma_{HCl}(\lambda)$ are the photoabsorption cross- sections of O_3 and HCl at photolysis wavelength of λ, respectively. $\phi_{O(1S)}$ and ϕ_H indicate the detection efficiencies of the resonance fluorescence from the excited states, $O(3s^1P_1)$ and $H(2p^2P_j)$, respectively, which are prepared by the VUV laser irradiation. The values of f_H and $f_{O(1S)}$ were taken from the

NIST atomic spectra database [38]. The values of $\sigma_{O3}(\lambda)$ and $\sigma_{HCl}(\lambda)$ were taken from Molina and Molina [39] and Sander *et al.* [12], respectively. The values of $S_{O(1S)}(\lambda)$ and $S_H(\lambda)$ were obtained by integrating the atomic line shapes in the fluorescence excitation spectra for the $O(^1S)$ and H atoms, respectively. Under our experimental conditions, the quenching of the excited O and H atoms by the gases is negligible. Because the total pressures in the chamber were less than 1.2 Torr and the radiative decay lifetimes of the excited states are less than several nanoseconds. The detection efficiency of the PMT system is assumed to be constant between the resonance fluorescence wavelengths of $O(3s^1P_1 - 2p^1S_0)$ and $H(2p^2P_j - 1s^2S)$ at 121.76 and 121.56 nm, respectively, since the difference of the wavelengths is very small. The electronic state $O(3s^1P_1)$, which is prepared by the VUV laser excitation at 121.76 nm, emits the two transition lines, $3p^1P_1 \rightarrow 2p^1S_0$ at 121.76 nm and $3p^1P_1 \rightarrow 2p^1D_2$ at 99.50 nm. The latter transition is not detected by the photomultiplier through the LiF window. The A-value for the $O(3p^1P_1 \rightarrow 2p^1S_0)$ transition is $A_1 = 2.06 \times 10^8$ sec^{-1} and that for the $O(3p^1P_1 \rightarrow 2p^1D_2)$ is $A_2 = 5.06 \times 10^8$ sec^{-1}. We used the relative values of the detection efficiencies as $\phi_{O(1S)} = A_1 / (A_1 + A_2)$ and $\phi_H = 1$.

The values of $\Phi_{O1S}^{O3}(193\text{ nm}) = (2.5 \pm 1.1) \times 10^{-3}$, $\Phi_{O1S}^{O3}(215\text{ nm}) = (1.4 \pm 0.4) \times 10^{-4}$, and $\Phi_{O1S}^{O3}(220\text{ nm}) = (5 \pm 3) \times 10^{-5}$ were thus determined, where the quoted errors were the 2σ statistical uncertainty of the experimental data. There are two energetically possible channels (6.1a) and (6.1b) for $O(^1S)$ formation in the UV photolysis of O_3. Observation of the $O(^1S)$ formation at both 215 and 220 nm is a clear evidence that the spin-forbidden channel (6.1a) is responsible for $O(^1S)$ formation from O_3 photolysis at those wavelengths. Intersystem crossing from the excited singlet state to a triplet state correlating to the channel (6.1a) products or direct photoexcitation onto the triplet state(s) can account for the $O(^1S)$ formation. A weak spin-obit interaction between the singlet and triplet excited states or small transition probability from the ground to the triplet state(s) may result in the very small quantum yield for $O(^1S)$ formation. Other spin-forbidden dissociation processes of $O(^1D) + O_2(X^3\Sigma_g^-)$, $O(^3P) + O_2(a^1\Delta_g)$, $O(^3P) + O_2(b^1\Sigma_g^+)$ in the photolysis of ozone have been reported at longer wavelengths (~ 325 nm) with the quantum yields of 0.08 – 0.10 [40].

6.3.2 Doppler profile of $O(^1S)$ produced from the photolysis of O_3 at 193 nm

Doppler profile of $O(^1S)$ was analyzed to investigate the $O(^1S)$ production

process in the photolysis of O_3 at 193 nm. Figure 6.4 shows the fluorescence excitation spectrum of the translationally thermalized $O(^1S)$ atoms and that of the nascent $O(^1S)$ atoms from the photolysis of O_3 at 193 nm. The thermalized $O(^1S)$ spectrum shown in Fig. 6.4a was measured with 17 mTorr of O_3 in 2 Torr of He buffer gas, at the time delay of 3 μs between photolysis and probe laser pulses. The nascent $O(^1S)$ spectrum shown in Fig. 6.4b was taken with 3 mTorr of O_3 and 150 mTorr of O_2, at the delay time of 70 ns. The FWHM of the spectral profile of the thermalized $O(^1S)$ atoms was 0.54 cm^{-1} with a Gaussian shape (Fig 6.4a). Assuming the Maxwell-Boltzman velocity distributions for the thermalized $O(^1S)$ at room temperature, the probe laser line width is calculated to be 0.48 cm^{-1}. Figure 6.4 shows that the spectrum of the nascent $O(^1S)$ has a broader feature than that of the thermalized $O(^1S)$. This is due to Doppler effects of the $O(^1S)$ fragment velocity components along the propagation direction of the probe laser [41]. We have examined the Doppler profiles for the maximum translational energy of the $O(^1S)$ atoms produced in the 193 nm photolysis of O_3. For the $O(^1S) + O_2(X^3\Sigma_g^-)$ process (channel 6.1a), the maximum possible Doppler shift is calculated to be 0.89 cm^{-1}. On the other hand, for the $O(^1S) + O_2(a^1\Delta_g)$ process (channel 6.1b), the maximum Doppler shift is calculated to be 0.23 cm^{-1}, which corresponds to the case that the whole available energy is released into the translational freedom in the 193 nm photolysis of O_3. Two solid and two dashed curves in Fig. 6.4b indicate the expected maximum spectral shifts convoluted with the probe laser linewidth for the $O(^1S) + O_2(a^1\Delta_g)$ (channel 6.1b) and $O(^1S) + O_2(X^3\Sigma_g^-)$ (channel 6.1a) processes, respectively. The experimentally obtained spectrum clearly indicates that the relatively fast components of the $O(^1S)$ cannot be explained by channel (6.1b). This suggests that channel (6.1a) should be responsible for $O(^1S)$ formation in the photolysis of O_3 at 193 nm, although the contribution of channel (6.1b) cannot be ruled out. Observation of the spin-forbidden channel (6.1a) in the photolysis of O_3 at 193 nm is reinforced with a small but non-negligible formation yield of $O(^1S)$ through channel (6.1a) at longer photolysis wavelengths of 215 and 220 nm as described in the previous section.

6.3.3 Quantum yields for $O(^1S)$ formation from N_2O and H_2O_2 photolysis at 193 nm

The $O(^1S)$ formation from the photodissociation of N_2O and H_2O_2 at 193 nm was also studied in this work. The partial pressures of N_2O and H_2O_2 in the chamber were

230 and 110 mTorr, corresponding to 7.4×10^{15} and 3.6×10^{15} molecules cm^{-3}, respectively. These samples were photolyzed at 193 nm (~10 mJ $pulse^{-1}$). Using the same experimental setup, the $O(^1S)$ formation from O_3 photolysis at 193 nm was probed just before the N_2O and H_2O_2 experiments were performed. The O_3 concentration in the chamber was 3.8×10^{14} molecules cm^{-3} as estimated by the absorption spectrometry. The $O(^1S)$ atoms are produced in the 193 nm photolysis with the quantum yield of $\Phi_{O1S}^{O3}(193\ nm) = (2.5 \pm 1.1) \times 10^{-3}$. We estimated the minimum detectable limit for $O(^1S)$ to be 3×10^8 atoms cm^{-3} for signal-to-noise ratio of 1.

No discernible LIF signal of $O(^1S)$ was observed from N_2O and H_2O_2 photolysis at 193 nm while significant LIF signal of $O(^1S)$ formation was observed from O_3 photolysis under the same experimental conditions. Considering the available absorption cross-sections of O_3 [39], N_2O [12], and H_2O_2 [12] at 193 nm, we have determined the upper limit values of the quantum yields for $O(^1S)$ formation in the 193 nm photolysis of N_2O and H_2O_2 to be $\Phi_{O1S}^{N2O}(193\ nm) \leq 8 \times 10^{-5}$ and $\Phi_{O1S}^{H2O2}(193\ nm) \leq 3 \times 10^{-5}$, respectively. In this study, the H atoms produced from H_2O_2 photolysis at 193 nm were also detected by the VUV-LIF method at 121.56 nm. The quantum yield measurement was made by comparing the VUV-LIF signal intensity of $H(^2S)$ atom produced in the 193 nm photolysis of H_2O_2 with that produced in the 193 nm photolysis of HCl. The H atom quantum yield was determined to be 0.20 ± 0.03, where the quoted errors were the 2σ statistical uncertainty of the experimental data.

The product channels and their branching ratios in the photodissociation of N_2O and H_2O_2 at 193 nm are summarized in Tables 6.1 and 6.2, respectively. In the photolysis of N_2O at 193 nm, $O(^1D) + N_2$ product channel is a dominant process with the branching ratio which is close to unity and other channels are minor (Table 6.1). The theoretical and experimental studies [42,43,44,45, etc.] have shown that dissociation of N_2O around 200 nm occurs mainly via the $2\ ^1A'$ state, and that the nearby $1\ ^1A''$ state may be involved in the dissociation process. An adiabatic correlation diagram for N_2O (N-NO, N_2O, N_2-O) system assuming a C_s symmetry suggests that the $O(^1S)$ formation is not favorable from both states [42]. In the photolysis of H_2O_2 at 193 nm, the sum of the quantum yield for OH + OH and H + HO_2 product channels can account for a H_2O_2 loss quantum yield of 1.0 with the uncertainties as shown in Table 6.2 [16,17].

6.3.4 Reaction kinetics of $O(^1S)$ with atmospheric molecules

A typical example of the temporal profile of VUV-LIF intensity of $O(^1S)$ following the 193-nm laser irradiation of a gas mixture of O_3 and O_2 is shown in Figure 6.5. The partial pressures of O_3 and O_2 were 15 mTorr and 750 mTorr, respectively. The temporal VUV-LIF signal of $O(^1S)$ exhibits an initial jump due to photolytic formation of $O(^1S)$ followed by a slow decay due to its removal. The translationally hot $O(^1S)$ atoms produced from reaction (6.1) are thermalized within 1 μs under our experimental conditions, as observed by measurements of the spectral broadening of the resonance line of $O(^1S)$ at 121.76 nm. In the reactions of $O(^1S)$ with the reactants (X), the temporal behavior of $O(^1S)$ atoms in the long time domain (t > 1 μs) is governed by the following processes:

$$O(^1S) + \text{reactants} \rightarrow \text{products} \qquad k_X \qquad (6.5)$$

$$O(^1S) \rightarrow \text{loss (by diffusion and gas mixture flow)} \qquad k_d. \qquad (6.6)$$

The $O(^1S)$ concentration as a function of reaction time, $[O(^1S)]_t$, can be expressed as follows:

$$[O(^1S)]_t = [O(^1S)]_0 \times \exp(-k't) \qquad (6.7)$$

$$k' = k_X[X] + k_{O2}[O_2] + k_{O3}[O_3] + k_d. \qquad (6.8)$$

$[O(^1S)]_t$ and $[O(^1S)]$ are the concentrations of $O(^1S)$ at delay time t and 0, respectively. [X] is the concentration of reactant X in the chamber. k' is the decay rate observed for the $O(^1S)$ concentration. The non-zero intercept k_d at zero reactant pressure results from the escape of $O(^1S)$ atoms from the probing zone. Single-exponential decay curves were obtained for temporal profiles of $O(^1S)$ as shown in Fig.6.5. The pseudo-first-order rate constant k' for a particular reactant pressure was derived by a nonlinear least-squares fit analysis. The resultant dependence of the decay rates, $k' - (k_{O3}[O_3] + k_d)$, on the number density of O_2 for $O(^1S) + O_2$ reaction is shown in Figure 6.6. Linear least-squares fit analysis of the data in Fig. 6.6 yielded the bimolecular rate constant of $k_{O2} = (2.85 \pm 0.31) \times 10^{-13}$ cm^3 molecule^{-1} s^{-1}. We studied the reaction kinetics of $O(^1S) + O_2$, CO_2, H_2O, O_3, and HCl to determine the bimolecular rate constants k_{O2}, k_{CO2}, k_{H2O}, k_{O3} and k_{HCl} at 295 ± 2 K. Plots of the decay rates versus the densities of the reactants are shown in Figs. 6.6 and 6.7. The bimolecular rate constants, $k_{CO2} = (3.09 \pm 0.29) \times 10^{-13}$, $k_{H2O} = (6.38 \pm 0.38) \times 10^{-10}$, $k_{O3} = (4.63 \pm 0.45) \times 10^{-10}$ and $k_{HCl} = (5.47 \pm 0.27) \times 10^{-10}$ cm^3 molecule^{-1} s^{-1}, were obtained from the slope of the best-fit straight lines. The quoted uncertainties of the results are the

2σ-statistical errors.

Table 6.3 lists the room-temperature bimolecular rate constants of the $O(^1S)$ reactions, in which both the results from the present study and previous studies are included for comparison. Reaction processes of the metastable $O(^1S)$ atoms have not been extensively investigated. While $O(^1D)$ atoms which have less energy than $O(^1S)$ react with small molecules very efficiently in almost every collision, the kinetics of $O(^1S)$ appears to be highly dependent on the nature of the collision partner [37].

The rate constant determined in this study at 295 ± 2 K for $O(^1S) + O_2$ is in agreement with the results of Atkinson and Welge [26] and Capetanakis et al. [34] within the uncertainties associated as listed in Table 6.3. The result obtained in the present study is also close to the value reported by Sondermann and Stuhl [33]. The branching ratios for the production of $O(^1D)$ and $O(^3P)$ from $O(^1S) + O_2$ were reported to be 0.31 ± 0.07 and 0.69 ± 0.07, respectively [27], while the electronic states of the product O_2 molecule are unknown. In the present study, the rate constant value for the $O(^1S) + O_2$ reaction has been provided using the novel experimental method which is different from the mothods used in the previous studies.

The rate constant k_{CO2} determined in this study for $O(^1S) + CO_2$ is consistent with the values of Black et al. [21], Filseth et al. [23], Atkinson and Welge [26], and Black et al. [29] within the uncertainties. Slanger and Black [31] studied the product channels in the reaction of $O(^1S) + CO_2$ and reported the branching ratios for $O(^3P)$ and $O(^1D)$ productions to be 0.37 ± 0.05 and 0.63 ± 0.05, respectively. In comparison with $O(^1S)$, the quenching of $O(^1D)$ by CO_2 is known to be extremely efficient with the room-temperature rate constant of 1.1×10^{-10} cm^3 $molecule^{-1}$ s^{-1} with no or little activation energy [12]. Those observations are indicative that the deactivation mechanism for $O(^1S) + CO_2$ is different from that for $O(^1D) + CO_2$.

We have determined the rate constant k_{H2O} for $O(^1S) + H_2O$. This is the first report of the reaction rate constant with definitive error limits for $O(^1S) + H_2O$. As listed in Table 6.3, the k_{H2O} values in the previous studies ranged from 7×10^{-11} to 5×10^{-10} cm^3 $molecule^{-1}$ s^{-1}. The result obtained in the present study is close to the report of Slanger and Black [31]. A very large rate constant for this reaction is indicative that reactive scattering as well as physical quenching is included in the removal process of $O(^1S)$ in collisions with H_2O. Slanger and Black [31] suggested the branching ratios of 0.30 ± 0.06, 0.09 ± 0.06 and 0.61 ± 0.06 for product channels $O(^1D) + H_2O$, $O(^3P)$ +

H_2O, and OH + OH, respectively.

The rate constant k_{O3} determined in this study for $O(^1S) + O_3$ is consistent with the former measurements by London et al. [24] and Koroleva and Khvorostovskaya [28] within the uncertainties. Since the rate constant for $O(^1S) + O_3$ is as large as the gas kinetic collision limit, it is likely that the reactive processes to produce $O + O + O_2$ play an important role in this reaction as well as $O(^1D)/O(^3P)$ formation through the physical quenching of $O(^1S)$.

For $O(^1S)$ + HCl reaction, the rate constant has not been reported before, and the present study provides a first determination of $k_{HCl} = (5.47 \pm 0.27) \times 10^{-10}$ cm^3 molecule^{-1} s^{-1}. On the analogy of the very fast $O(^1S) + O_3$ and $O(^1S) + H_2O$ reactions, it is probable that reactive scattering as well as physical quenching is included in the removal process of $O(^1S)$ in collisions with HCl. Both Cl + OH and ClO + H productions are energetically feasible as product channels in the reactive scattering process.

6.4 Atmospheric implications

6.4.1 OH production in the stratosphere and mesosphere

In the stratosphere and mesosphere below about 60 km, production of $O(^1D)$ from UV photolysis of O_3 is followed by generation of chemically active species such as OH radicals through the reaction of $O(^1D)$ with H_2O, while most of $O(^1D)$ is quenched to $O(^3P)$ by collisions with air (N_2 and O_2) [46]:

$$O(^1D) + H_2O \rightarrow 2OH \quad (6.9)$$

$$O(^1D) + N_2 \rightarrow O(^3P) + N_2 \quad (6.10)$$

$$O(^1D) + O_2 \rightarrow O(^3P) + O_2. \quad (6.11)$$

The $O(^1S)$ atoms produced from O_3 photolysis might generate OH radicals through the reaction of $O(^1S)$ with H_2O in the stratosphere and mesosphere. The reaction rate of $O(^1S)$ with H_2O is very fast while the quenching rate of $O(^1S)$ with N_2 an O_2 are rather slow (Table 6.4):

$$O(^1S) + H_2O \rightarrow \text{products} \quad (6.12)$$

$$O(^1S) + N_2 \rightarrow O(^1D \text{ or } ^3P) + N_2 \quad (6.13)$$

$$O(^1S) + O_2 \rightarrow O(^1D \text{ or } ^3P) + O_2. \quad (6.14)$$

The branching for OH formation channel in reaction (6.12) was reported to be 0.61 [31]. The atmospheric OH production rates from $O(^1D)$ and $O(^1S)$ reactions with H_2O as a

function of the altitude between 20 and 60 km, R_{OH}^{1D} and R_{OH}^{1S}, have been estimated using the following expressions, respectively;

$$R_{OH}^{1D} = \frac{k_{6.9}[H_2O]Y_{OH}^{1D}}{k_{6.9}[H_2O]+k_{6.10}[N_2]+k_{6.11}[O_2]} \times [O_3]\int F(\lambda)\,\sigma_{O3}(\lambda)\,\Phi_{O(1D)}^{O3}(\lambda)\,d\lambda \quad (6.15)$$

$$R_{OH}^{1S} = \frac{k_{6.12}[H_2O]Y_{OH}^{1S}}{k_{6.12}[H_2O]+k_{6.13}[N_2]+k_{6.14}[O_2]} \times [O_3]\int F(\lambda)\,\sigma_{O3}(\lambda)\,\Phi_{O(1S)}^{O3}(\lambda)\,d\lambda, \quad (6.16)$$

where λ is wavelength, $F(\lambda)$ is the solar flux, $\sigma_{O3}(\lambda)$ is the absorption cross section of ozone, $\Phi_{O1D}{}^{O3}(\lambda)$ and $\Phi_{O1S}{}^{O3}(\lambda)$ are the quantum yields of $O(^1S)$ and $O(^1D)$ from the photolysis of ozone at λ, respectively, $k_{6.9}$, $k_{6.10}$, $k_{6.11}$, $k_{6.12}$, $k_{6.13}$, and $k_{6.14}$ are the reaction rate constants for reactions (6.9), (6.10), (6.11), (6.12), (6.13), and (6.14), respectively. The rate constants adapted are listed in Table 6.4. The $k_{6.12}$ value determined in the present study was used. The temperature-dependent rate constants $k_{6.14}$ for $O(^1S)$ [34] and $k_{6.10}$ and $k_{6.11}$ for $O(^1D)$ [12] reactions were taken into account. $Y_{OH}{}^{1D}$ and $Y_{OH}{}^{1S}$ are molar yields for OH formation from $O(^1D) + H_2O$ reaction ($Y_{OH}{}^{1D} = 2$) [18] and $O(^1S) + H_2O$ reaction ($Y_{OH}{}^{1S} = 1.22$) [31]. For the $O(^1S)$ quantum yields, it was assumed that the yields follow linear functions in the ranges 193 - 215 nm and 215 - 220 nm. Below 193 nm, the yield was assumed to be 2.5×10^{-3}. Above 220 nm, monotonic decrease of the yield from 5×10^{-5} at 220 nm to zero at 234 nm was assumed. The values of $F(\lambda)$ are calculated using the program presented by Kylling *et al.* [47]. The values of temperature-dependent $\sigma_{O3}(\lambda)$ are taken from the data presented by Molina and Molina [39]. The loss of $O(^1S)$ is dominant by reaction (6.14) at all altitudes between 20 and 60 km. Radiative decay and the reaction with O atom are unimportant as the loss processes of $O(^1S)$ in the altitude range of 20-60 km.

Figure 6.8 shows the percentage fraction of the OH production from $O(^1S) + H_2O$ relative to $O(^1D) + H_2O$, $R_{OH}{}^{1S}/ R_{OH}{}^{1D} \times 100$, as a function of altitude between 20 and 60 km at mid-latitudes at noon (SZA=50°), where $R_{OH}{}^{1S}$ is the OH production rate from $O(^1S) + H_2O$ reaction while $R_{OH}{}^{1D}$ is that from $O(^1D) + H_2O$ reaction. It has been found that the maximum contribution of $O(^1S) + H_2O$ reaction in the OH production rates appears at 30 km altitude, and the fraction relative to $O(^1D) + H_2O$ reaction is about 2.5 %.

The solar actinic flux distribution and photoabsorption cross-sections of N_2O

and H_2O_2 result in the photodissociation of those molecules around 200 nm in the stratosphere [12]. Therefore, we roughly have estimated the upper limits of the $O(^1S)$ production rate from N_2O and H_2O_2 relative to that from O_3 photolysis, assuming the wavelength-independent constant values of the $O(^1S)$ quantum yield below threshold wavelengths for channels (6.2) and (6.3), 8×10^{-5} and 3×10^{-5}, respectively. The $O(^1S)$ productions from N_2O and H_2O_2 relative to that from O_3 are estimated to be $< 10^{-3}$ and $< 10^{-5}$, respectively, at all altitudes between 20 and 60 km, using the cross-sections [12], actinic flux [47], and natural abundances [46]. The natural abundances of N_2O and H_2O_2 range from 1.1 to 270 ppbv and from 0.44 to 110 pptv, respectively, in the altitude range of 20-60 km [46]. The $O(^1S)$ formation from N_2O and H_2O_2 photolysis, even if it occurs, is not significant as the OH source in the stratosphere and mesosphere.

6.4.2 Dayglow emission in the mesosphere and lower thermosphere

The optical emission of the atomic transition of $O(^1S - {}^1D)$ at 557.7 nm is known as a green component in dayglow, nightglow, and aurora spectra. The available database on the greenline dayglow emission has recently been greatly expanded as a result of observations made with the WINDII on board the UARS [48]. The VER has been obtained over the altitude range 80 to 300 km from the WINDII observation. The WINDII data showed that the peak VER around 90 - 100 km altitude was larger by a factor of three or more in the daytime than at night [48,49,50,51]. The observation indicates that further excitation processes should be involved in addition to the three-body recombination process of atomic oxygen (Barth mechanism). The Barth mechanism is known to be the dominant excitation process of the nightglow emission peak around 100 km [52], that is,

$$O(^3P) + O(^3P) + M \rightarrow O_2^* + M \qquad (6.17)$$

$$O_2^* + O(^3P) \rightarrow O_2(X^3\Sigma^-_g) + O(^1S), \qquad (6.18)$$

where O_2^* is electronically excited state(s) of oxygen molecule. Shepherd and co-workers [49,50,51] have proposed that photodissociation of O_2 by the solar radiation between 100 and 130 nm, especially at Lyman-β(102.6 nm), is primary source of $O(^1S)$ for this emission peak in the daytime.

We have estimated the impact of the direct formation of $O(^1S)$ from the UV photolysis of O_3 on the greenline dayglow emission. The VER is obtained by taking into account the following processes in addition to reactions (6.12) and (6.14) at the

altitude above 50 km:

$$O(^1S) \rightarrow O(^1D) + h\nu\ (557.7\ nm) \quad (6.19)$$

$$O(^1S) \rightarrow O(^3P) + h\nu\ (297.2\ nm) \quad (6.20)$$

$$O(^1S) + O(^3P) \rightarrow O(^1D \text{ or } ^3P) + O(^3P) \quad (6.21)$$

$$O(^1S) + O_2(a^1\Delta_g) \rightarrow \text{products.} \quad (6.22)$$

Assuming the photochemical steady-state conditions, the VER of $O(^1S)$ from O_3 photolysis, $\eta(O_3)$, can be calculated as a function of altitude between 50 - 100 km using the following expression:

$$\eta(O_3) = \frac{A_{6.19}}{A_{6.19} + A_{6.20} + k_{6.12}[H_2O] + k_{6.14}[O_2] + k_{6.21}[O] + k_{6.22}[O_2(a^1\Delta_g)]} \times [O_3] \int F(\lambda)\sigma_{O3}(\lambda)\Phi_{O1S}^{O3}(\lambda)d\lambda \quad , \quad (6.23)$$

where A_{19} and A_{20} are the Einstein coefficients for channels (6.19) and (6.20), respectively, $k_{6.12}$, $k_{6.14}$, $k_{6.21}$, and $k_{6.22}$ are the rate constants for reactions (6.12), (6.14), (6.21), and (6.22), respectively, and $\Phi_{O1S}^{O3}(\lambda)$ is the quantum yield of $O(^1S)$ from O_3 photolysis at λ. The Einstein coefficients and rate constants used in the calculations are listed in Table 6.4. The solar flux spectra $F(\lambda)$ were taken from Shimazaki [53] and Kylling *et al.* [47]. The atmospheric densities and temperatures of the neutral were taken from the MSISE-90 model atmosphere [54]. The densities of O_3 were calculated on the assumption of the photochemical steady-state between O_3 and $O(^3P)$. The densities of $O_2(a^1\Delta_g)$ were calculated using the VER profile of the dayglow $O_2(a^1\Delta_g - X^3\Sigma_g^-)$ (0 - 0) band reported by Evans *et al.* [55]. Figure 6.9 shows the estimated VER profile for $O(^1S)$ from O_3 photolysis as a function of altitude. The daytime VER profile observed by WINDII and the VER profile for $O(^1S)$ produced from the Barth mechanism (6.17) - (6.18) are also plotted in Fig. 6.9 for comparison. The WINDII emission profile, which was analyzed by Shepherd *et al.* [50], was obtained at a SZA of 47.9° and the local time of 10.5 hr. The VER profile of $O(^1S)$ produced from the Barth mechanism was calculated using the parameters of McDade *et al.* [52], which were obtained from the rocket measurements of both the $O(^1S)$ nightglow emission rates and atomic oxygen densities. In Figure 6.9, two distinct peaks have been identified in the VER profile of $O(^1S)$ produced from the UV photolysis of O_3, one is around 90 km altitude and the other is below 50 km. The peaks probably correspond to two peaks in the number density profile of O_3, one is around 85 km and the other is around 30 km

[56,57]. The peak value of VER for $O(^1S)$ produced from the O_3 photolysis around 90 km is ~1 photon cm^{-3} s^{-1}, while that of the observed profile is ~700 photons cm^{-3} s^{-1}. This result indicates that the $O(^1S)$ formation in the UV photolysis of O_3 is not significant as an excitation process of greenline dayglow around 90 km altitude.

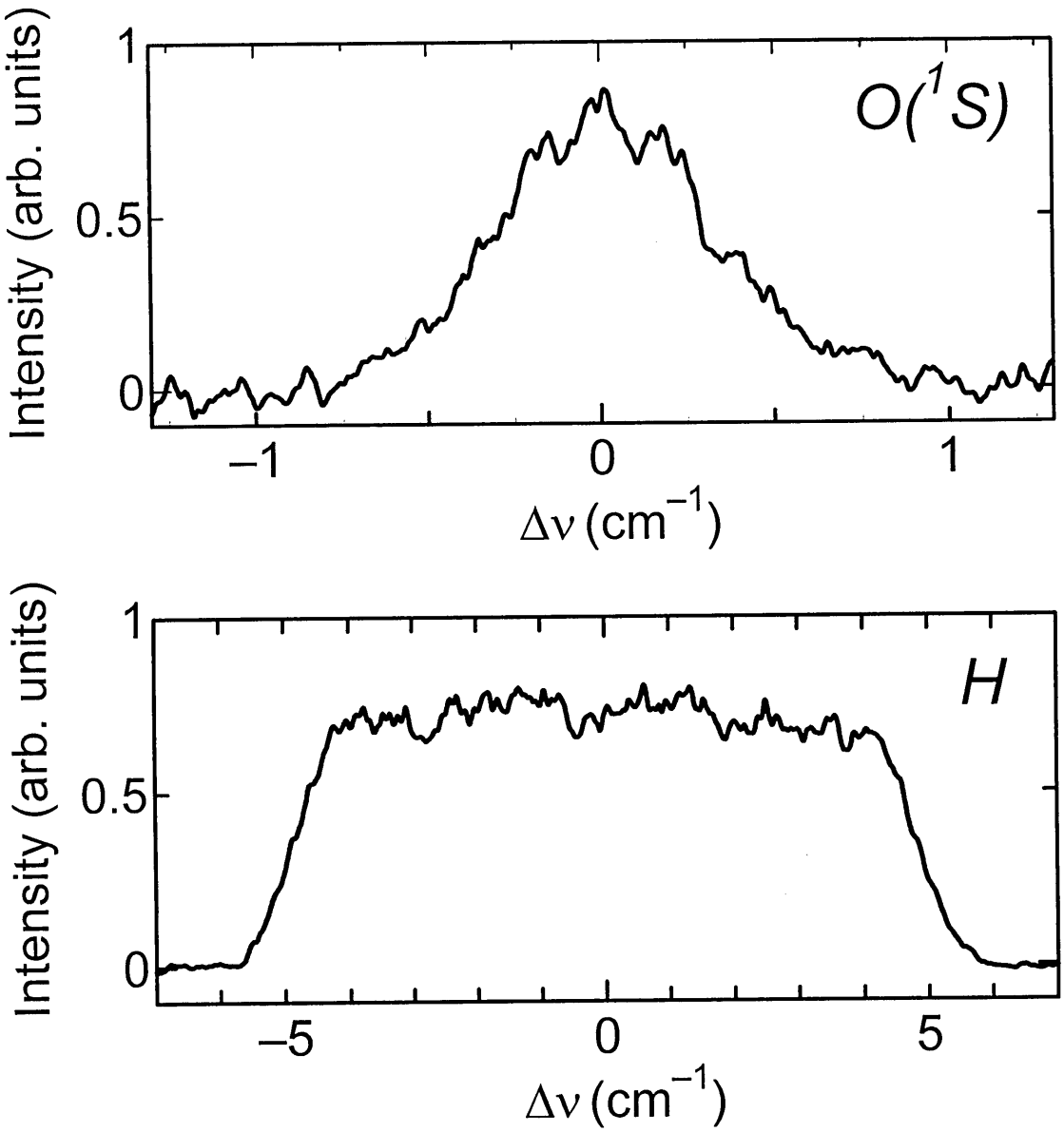

Figure 6.1. The fluorescence excitation spectra of $O(^1S)$ produced from the photolysis of O_3 at 193 nm and H atoms from HCl at 193 nm, in which the VUV probe laser wavelength was scanned over the Doppler profiles of each fragments. The delay time between the photolysis and probe laser pulses was 150 ns. The partial pressures of O_3 and HCl in the reaction cell were 20 and 4 mTorr, respectively.

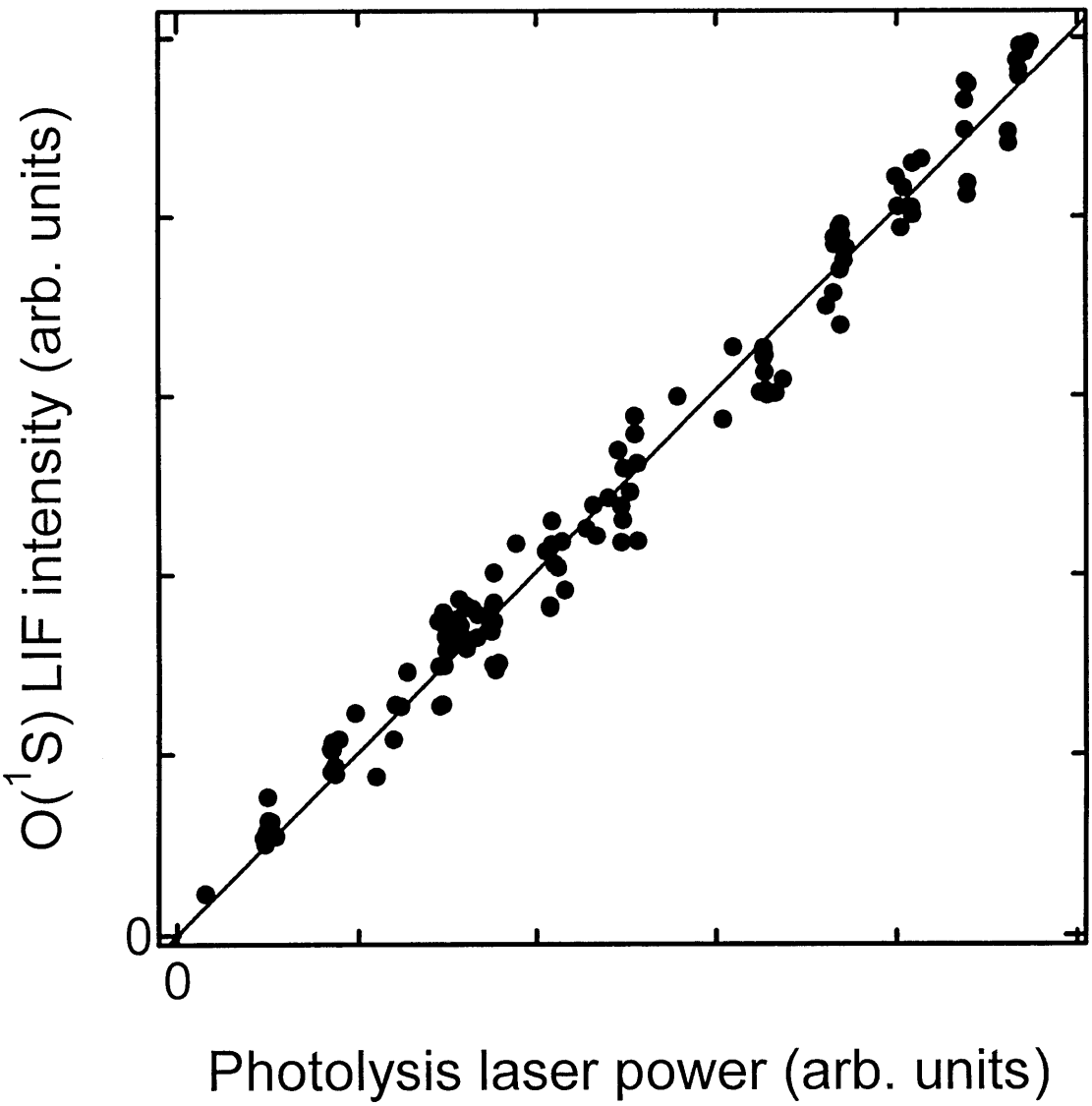

Figure 6.2. LIF signal intensity for $O(^1S)$ versus the photolysis laser power. The photolysis laser power was changed while monitoring the $O(^1S)$ LIF signal at 121.76 nm. The time delay between the photolysis and probe laser pulses was 150 ns and the pressure of O_3 in the reaction cell was 20 mTorr. Solid line is the results of linear weighted fit analysis of the experimental data.

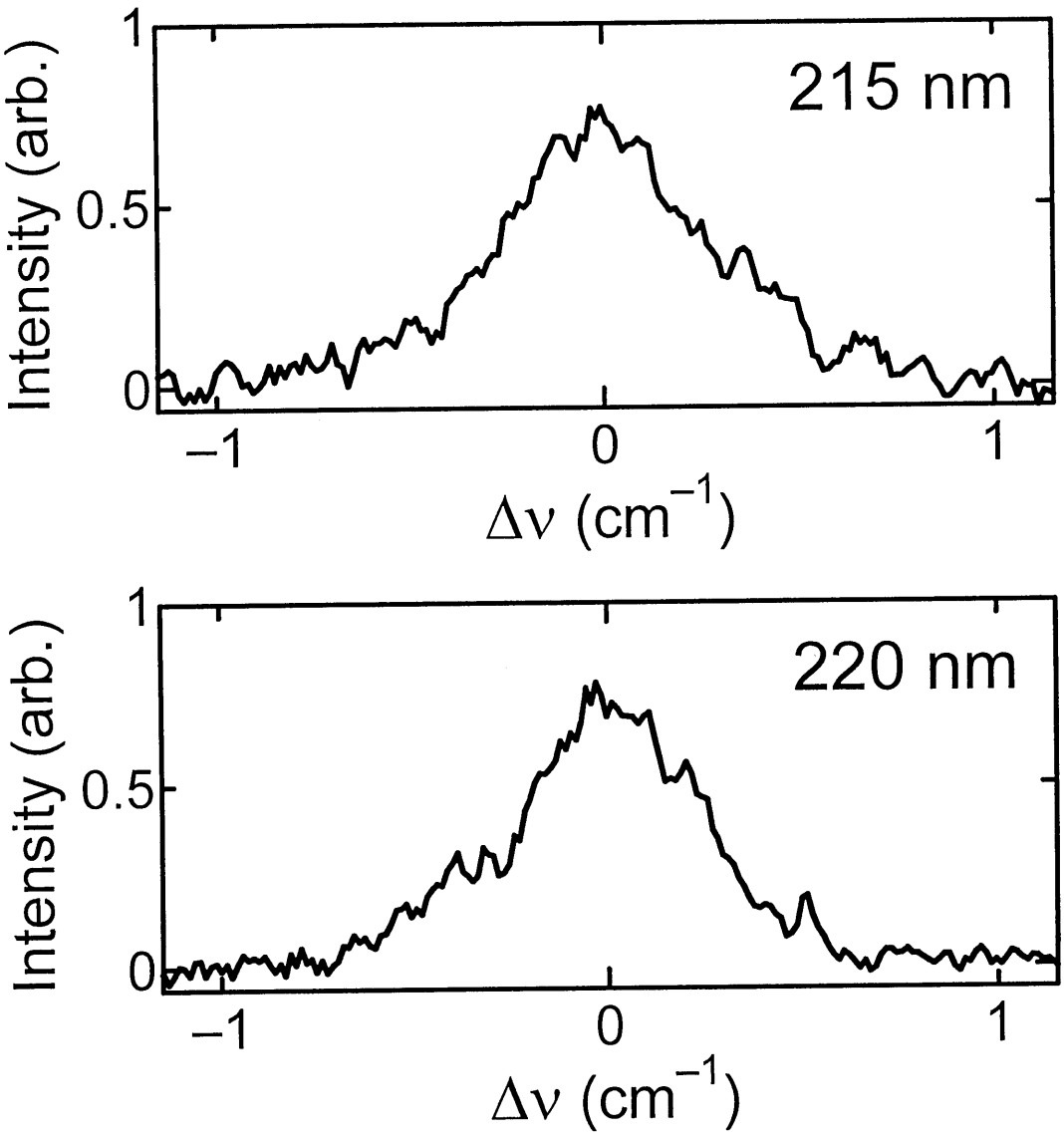

Figure 6.3. Fluorescence excitation spectra of $O(^1S)$ produced from the photolysis of O_3 at 215 and 220 nm. The spectrum was measured at the pressures of 25 mTorr O_3 and 1.2 Torr of O_2, and at the time delay of 100 ns between the photolysis and probe laser pulses.

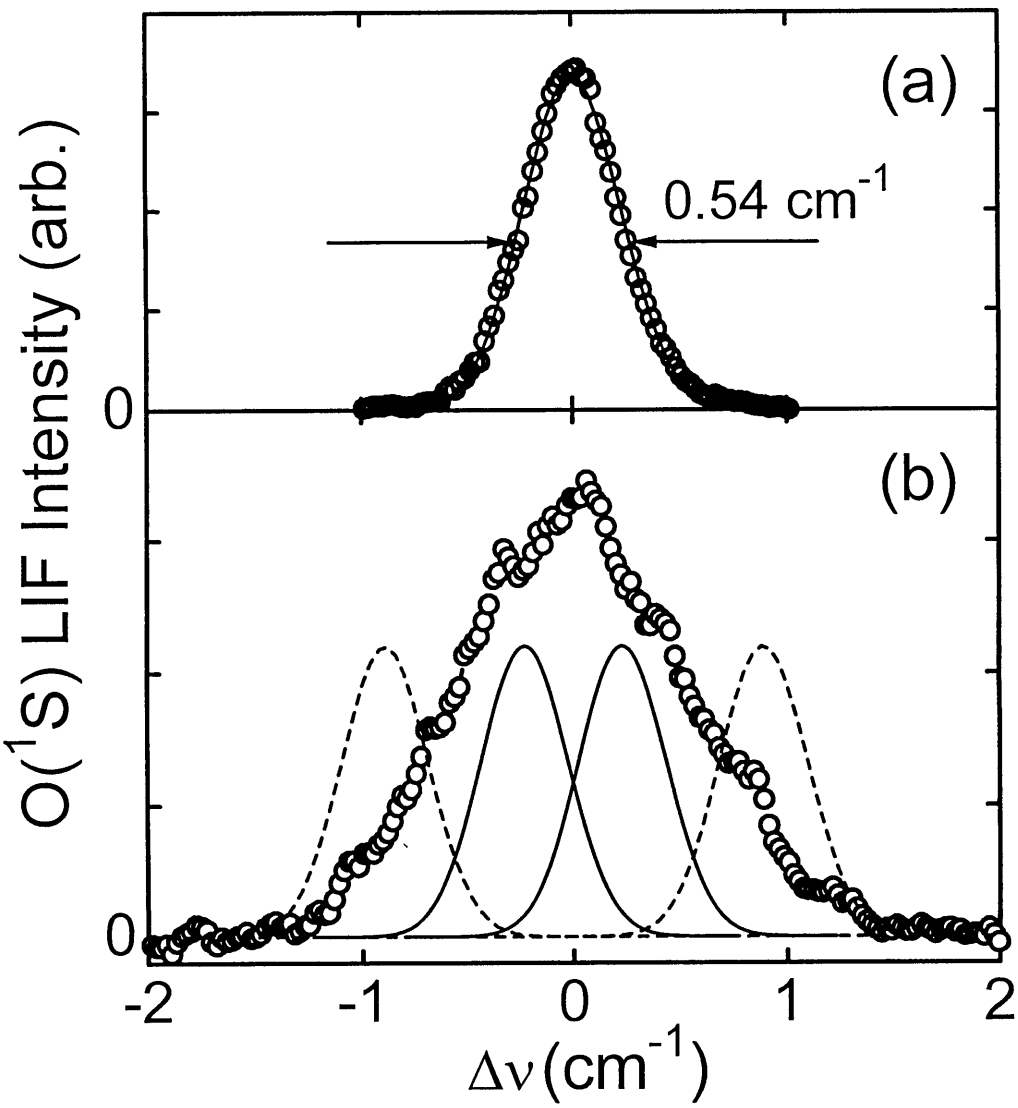

Figure 6.4. (a) Fluorescence excitation spectrum of thermalized O(^{1}S) atoms. The thermalized spectrum was measured with 17 mTorr O_3 in 2 Torr of He buffer gas, and a time delay of 3 μs between photolysis and probe laser pulses. The solid curve indicates a Gaussian shape with FWHM of 0.54 cm^{-1}, which fits the observed spectrum. (b) Fluorescence excitation spectrum of nascent O(^{1}S) from the photolysis of O_3 at 193 nm, which was measured at the pressures of 3 mTorr of O_3 and 150 mTorr of O_2 at the time delay of 70 ns. Solid and dashed curves indicate the expected maximum spectral shifts (0.23 and 0.89 cm^{-1}) convoluted with the probe laser linewidth (0.48 cm^{-1}) when O(^{1}S) + O_2($a^1\Delta_g$) (channel 6.1b) and O(^{1}S) + O_2($X^3\Sigma_g^-$) (channel 6.1a) processes was assumed, respectively (see text).

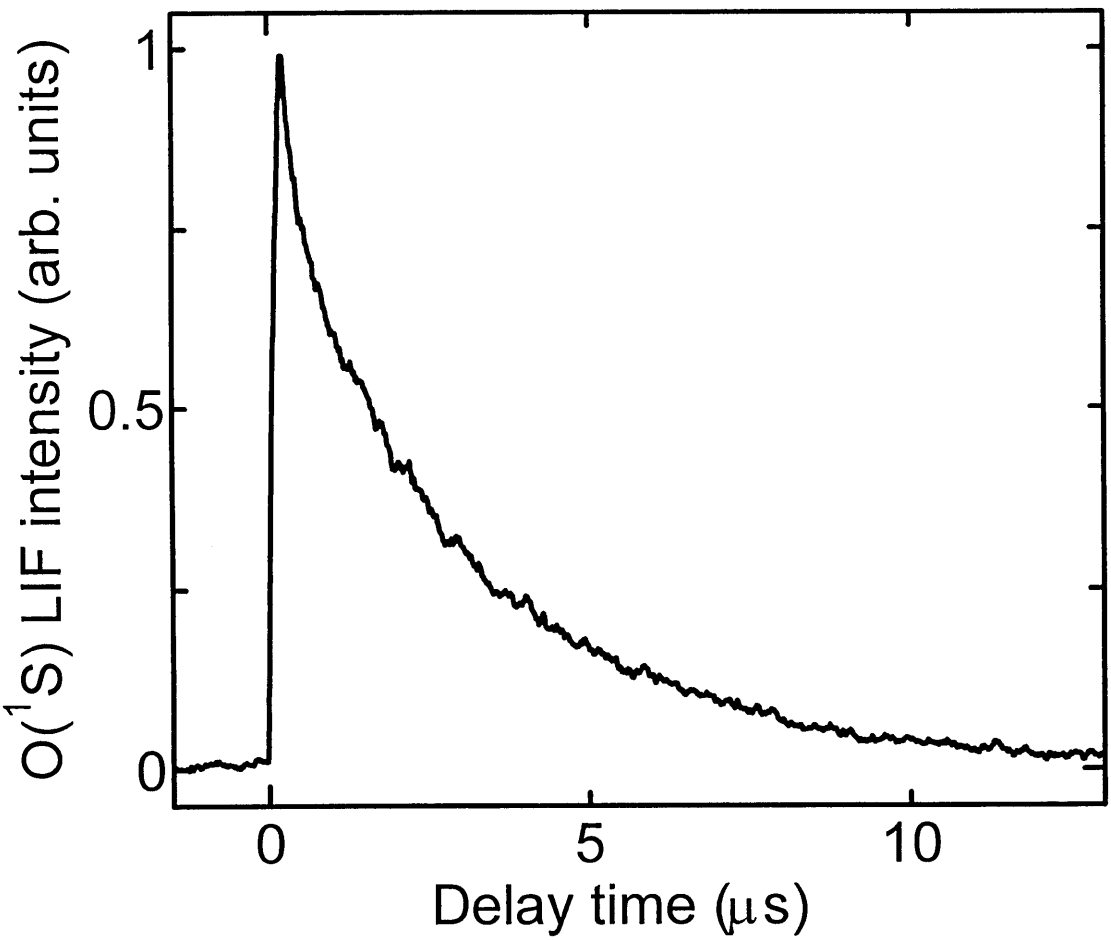

Figure 6.5. Typical example of the temporal decay curve of $O(^1S)$ following the 193-nm laser photolysis of the gas mixture containing 16 mTorr of O_3 in 750 mTorr of O_2 at 295 K. The $O(^1S)$ atoms were directly detected by the VUV-LIF spectroscopy technique at 121.76 nm.

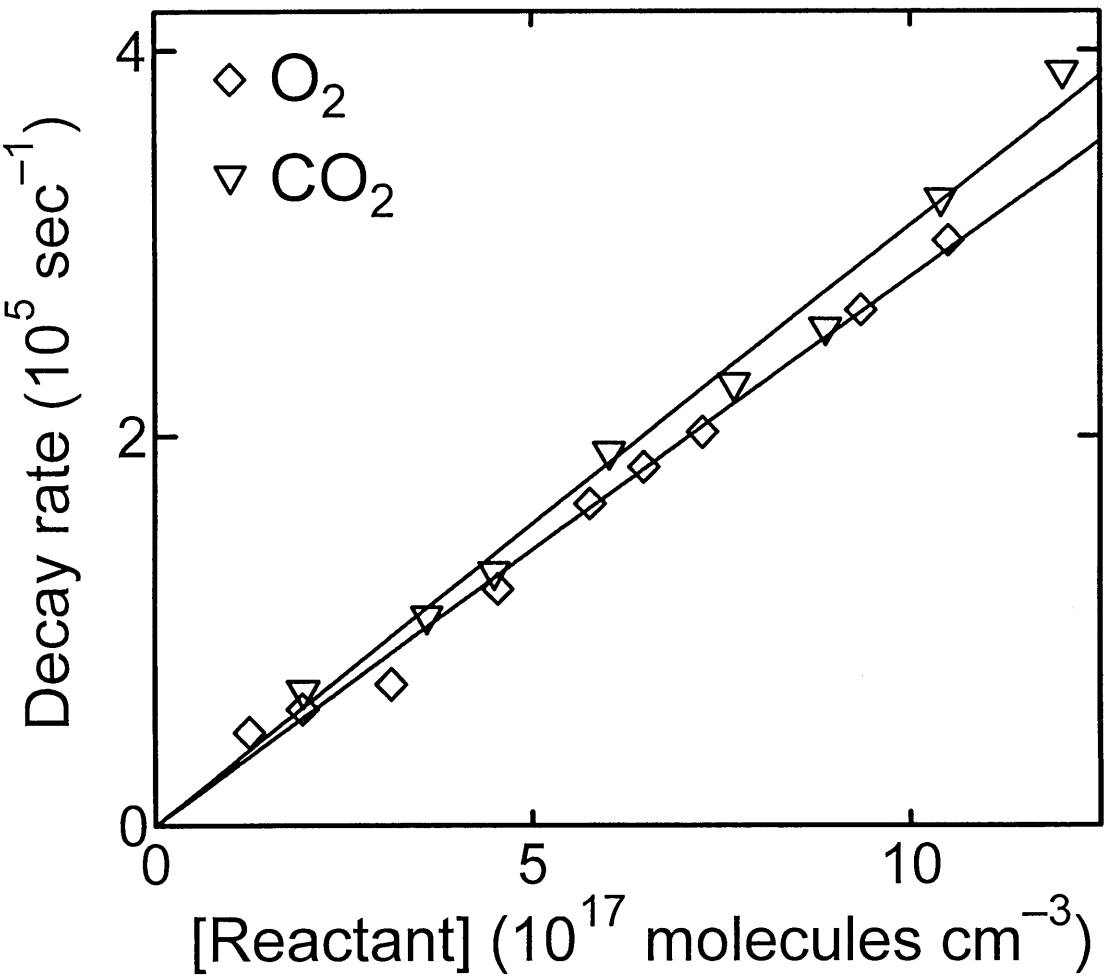

Figure 6.6. Plot of pseudo-first-order-loss of $O(^1S)$ atoms, $k_X[X]$, versus the concentration of the reactants (open diamond = O_2 and open inverted triangle = CO_2). Solid lines are the results of linear weighted fit analysis of the experimental data.

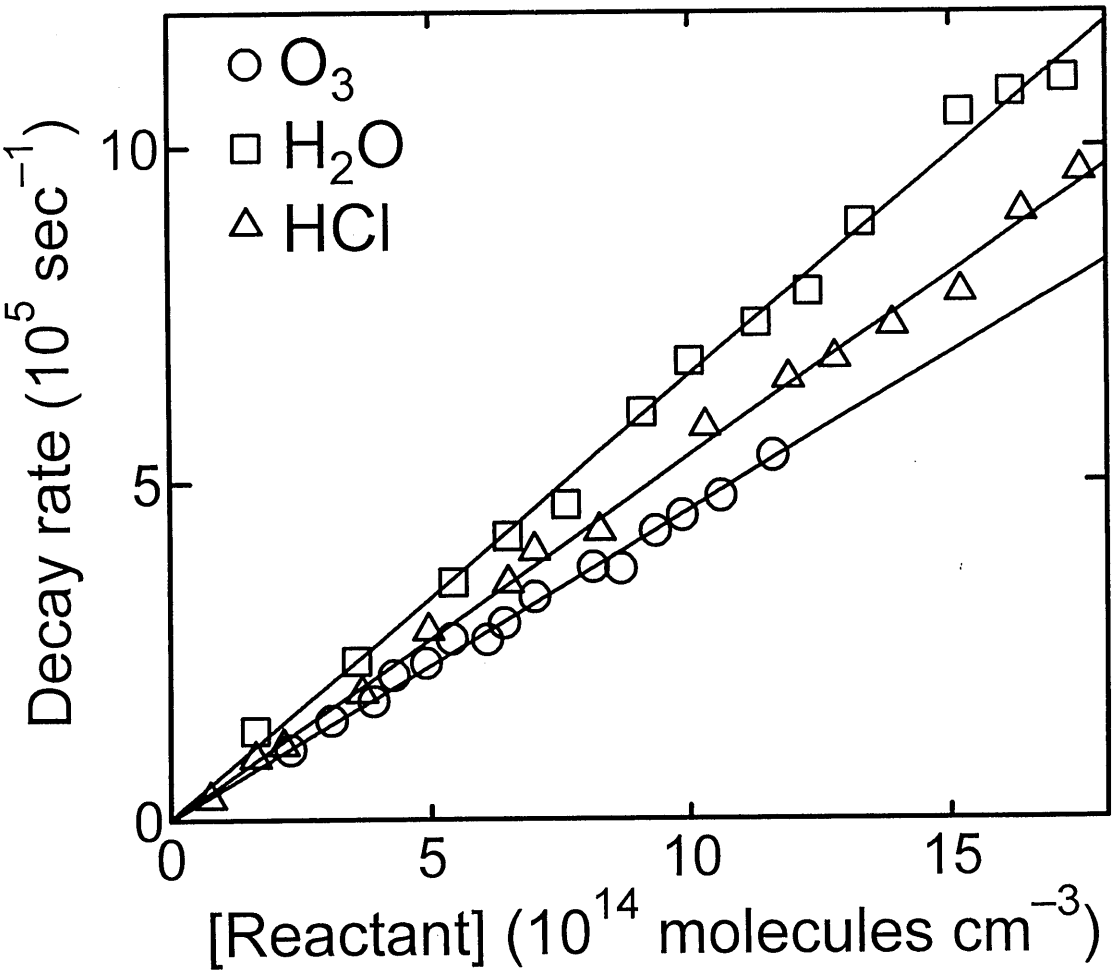

Figure 6.7. Plot of pseudo-first-order loss of $O(^1S)$ atoms, $k_X[X]$, versus the concentration of the reactants (open square = H_2O, open circle = O_3, and open triangle = HCl). Solid lines are the results of linear weighted fit analysis of the experimental data.

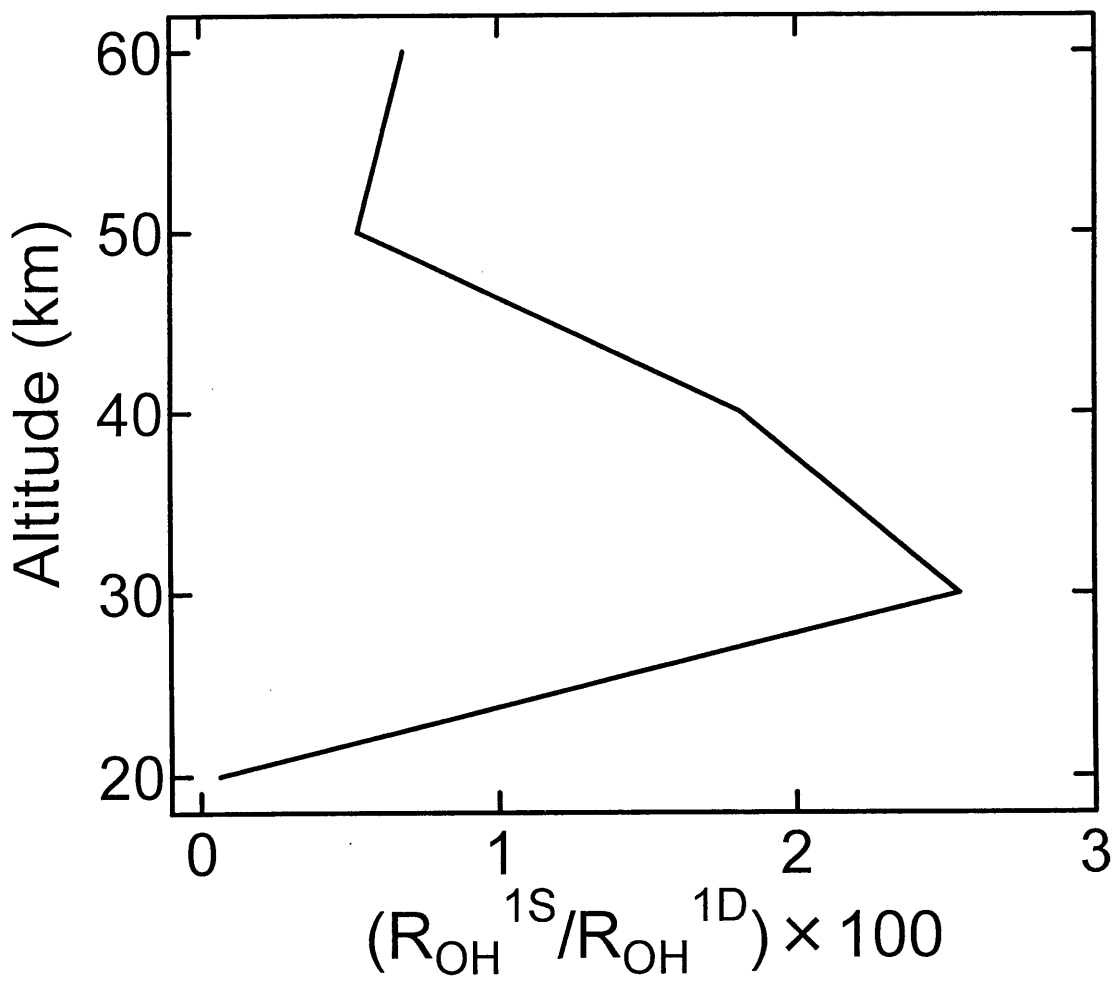

Figure 6.8. Percentage fraction of the calculated OH production from $O(^1S) + H_2O$ relative to $O(^1D) + H_2O$, $R_{OH}{}^{1S}/R_{OH}{}^{1D} \times 100$, as a function of altitude in the mid-latitudes (see text).

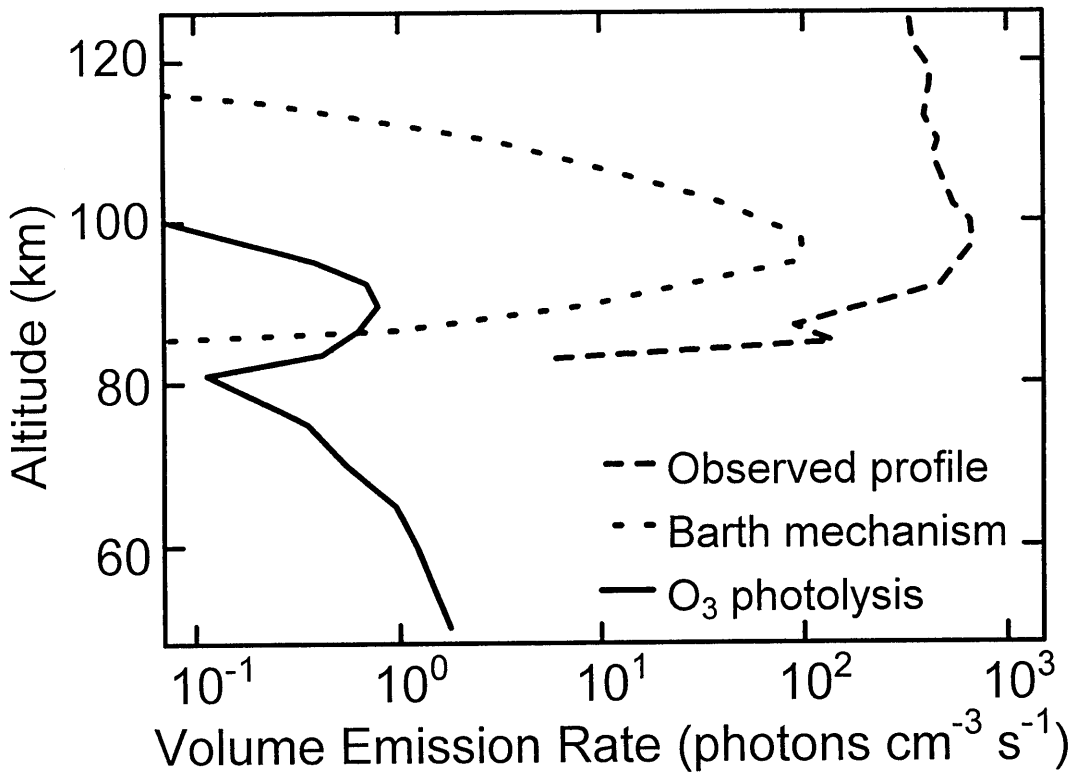

Figure 6.9. The calculated VER (volume emission rate) profiles of $O(^1S)$ produced from O_3 photolysis (solid line) and that of $O(^1S)$ produced by the Barth mechanism (dotted line), and a daytime VER profile observed by WINDII for a solar zenith angle (SZA) of 47.9° and the local time of 10.5 hr (dashed line) [50].

Table 6.1. Photodissociation channels and their branching ratios in the photodissociation of N_2O at 193 nm.

Channel	$\lambda_{threshold}$[a]	Branching ratio[b]	Detected Product	Refs.
$N_2 + O(^1D)$	341	~1.0	-	Sander *et al.* (2003) [12]
N + NO	248	$\leq 8 \times 10^{-3}$	NO	Greenblatt and Ravishankara (1990) [10]
N + NO	248	$(2.1 \pm 0.9) \times 10^{-3}$	N	This work
$N_2 + O(^3P)$	742	$(5 \pm 2) \times 10^{-3}$	$O(^3P)$	Nishida *et al.* (2004) [14]
$N_2 + O(^1S)$	211	$\leq 8 \times 10^{-5}$	$O(^1S)$	This work
$N_2 + O(^1S)$	211	≤ 0.04	O[c]	Felder *et al.* (1991) [11]

a. Thermochemical threshold for each channel in nm.

b. Quoted uncertainties include the 2σ-statistical errors.

c. Felder *et al.* (1991) [11] detected the translational energy distribution of O atoms with time-of-flight mass spectrometry in the molecular beam photodissociation experiment.

Table 6.2. Photodissociation channels and their branching ratios in the photodissociation of H_2O_2 at 193 nm.

Channel	$\lambda_{threshold}$[a]	Branching ratio[b]	Detected Product	Refs.
$2OH(X^2\Pi)$	555	0.76 ± 0.09	OH	Vaghjiani *et al.* (1992) [16]
		0.61 ± 0.07	OH	Schiffman *et al.* (1993) [17]
$H + HO_2$[c]	325	0.20 ± 0.03	H	This work
		0.25[d] ± 0.02	H	Gerlach-Meyer *et al.* (1987) [15]
		0.16 ± 0.04	H	Vaghjiani *et al.* (1992) [16]
$O(^3P)/O(^1D) + H_2O$	829/358	< 0.001	$O(^3P)$	Vaghjiani *et al.* (1992) [16]
$O(^1S) + H_2O$	213	$\leq 3 \times 10^{-5}$	$O(^1S)$	This work
		< 0.02	$O(^3P)$	Vaghjiani *et al.* (1992) [16]

a. Thermochemical threshold for each channel in nm.

b. Quoted uncertainties include 2σ-statistical errors.

c. $2H + O_2$ channel is also possible, $\lambda_{threshold} = 209$ nm.

d. The value of 0.12 ± 0.01 which was originally reported by Gerlach-Meyer et al. [15] has been modified using the new cross-section value recommended by NASA [12] and by Nicovich and Wine [58].

Table 6.3. Summary of former and present studies on the reaction kinetics of $O(^1S)$ with O_2, CO_2, H_2O, O_3, and HCl at room temperature.

	k [a]	$O(^1S)$ detection method	Refs.
O_2	1.0×10^{-13}	$O(^1S \rightarrow {}^1D)$ Emission [b]	Young and Black (1966) [19]
	3.2×10^{-13}	$O(^1S \rightarrow {}^1D)$ Emission [b]	Stuhl and Welge (1969) [20]
	5×10^{-13}	$O(^1S \rightarrow {}^1D)$ Emission [b]	Black et al. (1969) [21]
	3.7×10^{-13}	$O(^1S \rightarrow {}^1D)$ Emission [b]	Filseth and Welge (1969) [22]
	$(3.6 \pm 0.4) \times 10^{-13}$	$O(^1S \rightarrow {}^1D)$ Emission [b]	Filseth and Stuhl (1970) [23]
	$(2.57 \pm 0.3) \times 10^{-13}$	$O(^1S \rightarrow {}^1D)$ Emission [b]	Atkinson and Welge (1972) [26]
	2.1×10^{-13}	$O(^1S \rightarrow {}^1D)$ Emission [b]	Slanger et al. (1972) [27]
	$(5 \pm 3) \times 10^{-13}$	$O(^1S \rightarrow {}^1D)$ Emission [b]	Koroleva and Khvorostovskaya (1973) [28]
	$(2.58 \pm 0.08) \times 10^{-13}$ [c]	$O(^1S \rightarrow {}^1D)$ Emission [b]	Sondermann et al. (1990) [33]
	$(2.64 \pm 0.16) \times 10^{-13}$	$O(^1S \rightarrow {}^1D)$ Emission [b]	Capetanakis et al. (1993) [34]
	$(2.85 \pm 0.31) \times 10^{-13}$ [d]	VUV-LIF	This work
CO_2	2.5×10^{-14}	$O(^1S \rightarrow {}^1D)$ Emission [b]	Young and Black (1966) [19]
	4.6×10^{-13}	$O(^1S \rightarrow {}^1D)$ Emission [b]	Stuhl and Welge (1969) [20]
	3×10^{-13}	$O(^1S \rightarrow {}^1D)$ Emission [b]	Black et al. (1969) [21]
	$(3.6 \pm 0.4) \times 10^{-13}$	$O(^1S \rightarrow {}^1D)$ Emission [b]	Filseth and Stuhl (1970) [23]
	3.9×10^{-13}	$O(^1S \rightarrow {}^1D)$ Emission [b]	London et al. (1971) [24]
	5×10^{-13}	$O(^1S \rightarrow {}^1D)$ Emission [b]	Welge et al. (1971) [25]
	$(3.31 \pm 0.3) \times 10^{-13}$	$O(^1S \rightarrow {}^1D)$ Emission [b]	Atkison and Welge (1972) [26]
	$(3.8 \pm 0.4) \times 10^{-13}$	$O(^1S \rightarrow {}^1D)$ Emission [b]	Black et al. (1975) [29]
	$(3.80 \pm 0.22) \times 10^{-13}$	$O(^1S \rightarrow {}^1D)$ Emission [b]	Capetanakis et al. (1993) [34]
	$(3.09 \pm 0.29) \times 10^{-13}$ [d]	VUV-LIF	This work

H_2O	$\sim 4 \times 10^{-10}$	$O(^1S \rightarrow {}^1D)$ Emission [b]	Filseth and Welge (1969) [22]
	$(7.0 \pm 3.5) \times 10^{-11}$	$O(^1S \rightarrow {}^1D)$ Emission [b]	Filseth and Stuhl (1970) [23]
	$(1.27 \pm 0.15) \times 10^{-10}$ [e]	$O(^1S \rightarrow {}^1D)$ Emission [b]	Bingham et al. (1976) [30]
	5.0×10^{-10}	$O(^3P)$ detection [f]	Slanger and Black (1978) [31]
	$(6.38 \pm 0.38) \times 10^{-10}$ [d]	VUV-LIF	This work
O_3	$(5.8 \pm 1) \times 10^{-10}$	$O(^1S \rightarrow {}^1D)$ Emission [b]	London et al. (1971) [34]
	$(8 \pm 3) \times 10^{-10}$	$O(^1S \rightarrow {}^1D)$ Emission [b]	Koroleva and Khvorostovskaya (1973) [28]
	$(4.63 \pm 0.45) \times 10^{-10}$ [d]	VUV-LIF	This work
HCl	$(5.47 \pm 0.27) \times 10^{-10}$ [d]	VUV-LIF	This work

a. Bimolecular reaction rate constant at room temperature in units of cm^3 $molecule^{-1}$ s^{-1}.
b. Emission arising from $O(^1S - {}^1D)$ transition at 557.7 nm.
c. The error limits are estimates of 3σ.
d. The error limits are estimates of 2σ.
e. The error limits are estimates of 1σ.
f. Products analysis was performed with O(3P) detection using an atomic oxygen lamp [31].

Table 6.4. Adopted reaction rate constants(k) and Einstein coefficients(A)

Reactions	k^a and A^b	Refs.
6.9	$k_{6.9} = 2.2 \times 10^{-10}$	Sander *et al.* (2003) [12]
6.10	$k_{6.10} = 3.2 \times 10^{-11} \exp(\frac{-70}{T})$	Sander *et al.* (2003) [12]
6.11	$k_{6.11} = 1.8 \times 10^{-11} \exp(\frac{-110}{T})$	Sander *et al.* (2003) [12]
6.12	$k_{6.12} = 6.38 \times 10^{-10}$	This work
6.13	$k_{6.13} < 5 \times 10^{-17}$	Okabe (1978) [1]
6.14	$k_{6.14} = 2.64 \times 10^{-13} \exp(\frac{-812+18.2T^2}{T})$	Capetanakis *et al.* (1993) [34]
6.18	$A_{6.18} = 1.26$	Martin et al. (1999) [38]
6.19	$A_{6.19} = 7.54 \times 10^{-2}$	Martin et al. (1999) [38]
6.20	$k_{6.20} = 2 \times 10^{-14}$	Slanger and Black (1981) [59]
6.21	$k_{6.21} = 2.6 \times 10^{-10}$	Kenner and Ogryzlo (1982) [60]

a. in cm^3 $molecule^{-1}$ s^{-1}

b. in s^{-1}

References for Chapter 6

[1] Okabe, H. *Photochemistry of small molecules*, Wiley-Interscience, New York, 1978.

[2] Wayne, R. P., *Chemistry of Atmospheres*, third edn., Oxford University Press, New York, 2000.

[3] Ghosh, S. N., *The Neutral Upper Atmosphere*, Kluwer Academic Publishers, Dordrecht, 2002.

[4] Slanger, T. G., Copeland, R. A., *Chem. Rev.*, **103**, 4731 (2003).

[5] Lee, L. C., Black, G., Sharpless, R. L., Slanger, T. G., *J. Chem. Phys.*, **73**, 256 (1980).

[6] Turnipseed, A. A., Vaghjiani, G. L., Gierczak, T., Thompson, J. E. Ravishankara, A. R., *J. Chem. Phys.*, **95**, 3244 (1991).

[7] Cooper, I. A., Neill, P. J., Wiesenfeld, J. R., *J. Geophys. Res.*, **98**, 12795 (1993).

[8] Stranges, D., Yang, X., Chesko, J. D., Suits, A. G., *J. Chem. Phys.*, **102**, 6067 (1995).

[9] Nishida, S., Taketani, F., Takahashi, K., Matsumi, Y., *J. Phys. Chem.*, **A 108**, 2710 (2004).

[10] Greenblatt, G. D., Ravishankara, A. R., *J. Geophys. Res.*, **95**, 3539 (1990).

[11] Felder, P., Haas, B. –M., Huber, J. R., *Chem. Phys. Lett.*, **186**, 177 (1991).

[12] Sander, S. P., Friedl, R. R., Golden, D. M., Kurylo, M. J., Huie, R. E., Orkin, V. L., Moortgat, G. K., Ravishankara, A. R., Kolb, C. E., Molina, M. J., Finlayson-Pitts, B. J., *Chemical Kinetics and Photochemical Data for use in Atmospheric Studies*, Evaluation No. 14, JPL Publication 02-25, 2003.

[13] Nakayama, T., Takahashi, K; Matsumi, Y.; Taniguchi, N; Hayashida, S., *J. Geophys. Res.*, **108**, doi: 10.1029/2003JD003709 (2003).

[14] Nishida, S., Takahashi, K., Matsumi, Y., Taniguchi, N., Hayashida, S., *J. Phys. Chem.*, **A108**, 2451 (2004).

[15] Gerlach-Meyer, U., Linnebach, E., Kleinermanns, K., Wolfrum, J., *Chem. Phys. Lett.*, **133**, 113 (1987).

[16] Vaghjiani, G. L., Turnipseed, A. A., Warren, R. F., Ravishankara, A. R., *J. Chem. Phys.*, **96**, 5878 (1992).

[17] Schiffman, A., Nelson, Jr. D. D., Nesbitt, D. J., *J. Chem. Phys.*, **98**, 6935 (1993).

[18] Atkinson, R., Baulch, D. L., Cox, R. A., Crowley, J. N., Hampson Jr., R. F., Hynes, R. G., Jenkin, M. E., Kerr, J. A., Rossi, M. J., Troe, J., 2005: *Summary of evaluated kinetics and photochemical data for atmospheric chemistry, IUPAC subcommittee on gas kinetics data evaluation for atmospheric chemistry*, Web Version (http://www.iupac-kinetic.ch.cam.ac.uk/).

[19] Young, R. A., Black, G. J., *Chem. Phys.*, **44**, 3741 (1966).

[20] Stuhl, E. A., Welge, K. H., *Can. J. Chem.*, **47** 1870 (1969).

[21] Black, G., Slanger, T. G., St. John, G. A., Young, R. A., *J. Chem. Phys.*, **51**, 116 (1969).

[22] Filseth, S. V., Welge, K. H., *J. Chem. Phys.*, **51**, 839 (1969).

[23] Filseth, S. V., Stuhl, E. A., *J. Chem. Phys.*, **52**, 239 (1970).

[24] London, G., Gilpin, R., Schiff, H. I., Welge, K. H., *J. Chem. Phys.*, **54**, 4512 (1971).

[25] Welge, K. H., Zia, A., Vietzke, E., Filseth, S. V., *Chem. Phys. Lett.*, **10**, 13 (1971).

[26] Atkinson, R., Welge, K. H., *J. Chem. Phys.*, **57**, 3689 (1972).

[27] Slanger, T. G., Wood, B. J., Black, G., *Chem. Phys. Lett.*, **17**, 401 (1972).

[28] Koroleva, E. A., Khvorostovskaya, L. E., *Opt. Spectrosc.*, **35**, 11 (1973).

[29] Black, G., Sharpless, R. L., Slanger, T. G., Lorents, D. C., *J. Chem. Phys.*, **62**, 4266 (1975).

[30] Bingham, F. W., Johnson, A. W., *J. Chem. Phys.*, **65**, 1663 (1976).

[31] Slanger, T. G., Black, G., *J. Chem. Phys.*, **68**, 989 (1978).

[32] Slanger, T. G., Black ,G., *J. Chem. Phys.*, **68**, 998 (1978).

[33] Sondermann, F., Stuhl, F., *J. Chem. Phys.*, **93**, 3978 (1990).

[34] Capetanakis, F. P., Sondermann, F., Hoser, S., Stuhl, F., *J. Chem. Phys.*, **98**, 7883 (1993).

[35] Capetanakis, F. P., Sondermann, F., Hoser, S., Stuhl, F., *Chem. Phys. Lett.*, **206**, 361 (1993).

[36] Hoser, S., Capetanakis, F. P., Kassner, Ch., Stuhl, F., *Chem. Phys. Lett.*, **208**, 399 (1993).

[37] Schofield, K., *J. Photochem.*, **9**, 55 (1978).

[38] Martin, W.C., et al., *NIST Atomic Spectra Database (version 2.0)*, National Institute of Standards and Technology, Gaithersburg, MD (http://physics.nist.gov/asd), 1999.

[39] Molina, L. T., Molina, M. J., *J. Geophys. Res.*, **91**, 14501 (1986).

[40] Matsumi, Y., Kawasaki, M., *Chem. Rev.*, **103**, 4767 (2003).

[41] Zare, R. N., Herschback, D. R., *Proc. IEEE*, **51**, 173 (1963).

[42] Hopper, D. G., *J. Chem. Phys.* **80**, 4290 (1984).

[43] Suzuki, T., Katayanagi, H., Mo, Y., Tonokura, K., *Chem. Phys. Lett.* **256**, 90 (1996).

[44] Teule, J. M., Groenenboom, G. C., Neyer, D. W., Chandler, D. W., Janssen, M. H. M., *Chem. Phys. Lett.* **320**, 177 (2000).

[45] Brouard, M., Clark, A. P., Vallance, C., Vasyutinskii, O. S., *J. Chem. Phys.* **119**, 771 (2003).

[46] Brassuer, G. P., J .J. Orlando, G. S. Tyndall, *Atmospheric Chemistry and Global Change*, Oxford University Press, New York, 1999.

[47] Kylling, A., Stamnes, K., Tasay, S. -C., *J. Atmos. Chem.* **21**, 115 (1995).

[48] Shepherd, G. G., et al., *J. Geophys. Res.*, **98**, 10,725 (1993).

[49] Singh, V., McDade, I. C., Shepherd G. G., Solheim, B. H., Ward, W. E., *Ann. Geophysicae.*, **14**, 637 (1996).

[50] Shepherd, G. G., Siddiqi, N. J., Wiens, R. H., Zhang, S., *Adv. Space. Res.*, **20**, 2127 (1997).

[51] Sharma, R. M-., Shepherd, G. G., *J. Geophys. Res.*, **109**, A03303, doi:10.1029/2003JA010183 (2004).

[52] McDade, I. C., Murtagh, D. P., Greer, R. G. H., Dickinson, P. H. G., Witt, G., Stegman, J., Llewellyn, E. J., Thomas, L., Jenkins, D. B., *Planet. Space Sci.* **34**, 789 (1986)

[53] Shimazaki, T., *Minor constituents in the middle atmosphere*, Kluwer Academic Publishers, 1985.

[54] Hedin, A. E., *J. Geophys. Res.* **96**, 1159 (1991).

[55] Evans, W. F., McDade, I. C., Yuen, J., Llewellyn, E., *Can. J. Phys.* **66**, 941 (1998).

[56] Gunson, M. R., Farmer, C. B., Norton, R. H., Zander, R., Rinsland, C. P., Shaw, J. H., Gao, B. -C., *J. Geophys. Res.* **95**, 13,867 (1990).

[57] Vardavas, I. M., Carver, J. H., Taylor, F. W., *Ann. Geophysicae.* **16**, 189 (1998).

[58] Nicovich, J. M., Wine, P. H., *J. Geophys. Res.*, **94**, 3487 (1988).

[59] Slanger T. G., Black, G., *Geophys. Res. Lett.* **8**, 535 (1981).

[60] Kenner, R. D., Ogryzlo, E. A., *J. Photochem.* **18**, 379 (1982).

Chapter 7

Summary and future perspective

In the present study, the high-sensitive techniques for $N(^4S)$ and $O(^1S)$ detection using vacuum ultraviolet laser-induced fluorescence (VUV-LIF) spectroscopy at 120.07 and 121.76 nm, respectively, were developed. The minimum detection limits for $N(^4S)$ and $O(^1S)$ atoms were estimated to be 2×10^9 and 3×10^8 atoms cm^{-3}, respectively. Using the new detection techniques, several important photochemical reactions related to NO_x and HO_x chemistry in the middle and upper atmosphere was studied.

The $N(^4S)$ formation process from UV photolysis of N_2O was studied. The quantum yield for $N(^4S)$ formation in the N_2O photolysis at 193 nm was determined to be $(2.1 \pm 0.9) \times 10^{-3}$. Impact of the photolytic $N(^4S)$ and $NO(X^2\Pi)$ production from N_2O photolysis on stratospheric chemistry was explored using a one-dimensional photochemical model while the fragmentation was not considered in former model calculations. When the $N(^4S)$ + NO dissociation channel was considered in the photochemical model, an enhancement of the NO_x production rate (up to 3%) was observed, which was followed by a decrease of the steady-state O_3 concentration throughout the stratosphere. The experimental technique of pulsed laser photolysis combined with the VUV-LIF detection was applied for the first time to the kinetic studies of the important reactions of $N(^4S)$ in the middle and upper atmosphere. The $N(^4S)$ atoms were produced following 193 nm ArF laser irradiation of NO and NO_2. The rate coefficients of $N(^4S)$ with NO and NO_2 at 295 ± 2 K were determined to be $(3.8 \pm 0.2) \times 10^{-11}$ and $(7.3 \pm 0.9) \times 10^{-12}$ cm^3 $molecule^{-1}$ s^{-1}, respectively. The competitive processes of the inelastic collisions to produce NO and the elastic collisions to thermalize the translational energy of $N(^4S)$ was also investigated for the reaction of suprathermal $N(^4S)$ reaction with O_2 at initial center-of-mass collision energy of about 0.24 - 0.6 eV. The suprathermal $N(^4S)$ atoms which have an average translational energy of 0.92 ± 0.095 eV in the laboratory flame were produced by 193 nm photolysis of NO_2 in bath gas of O_2. No clear evidence of the NO production was observed, which will be explained by a relatively large value of the thermalization cross section

compared with the inelastic collision cross section. The thermalization rates of suprathermal $N(^4S)$ in collisions with N_2, O_2, He and Ar were experimentally determined for the first time. Those thermalization rates are crucial parameters for evaluating the contribution of the reaction of suprathermal $N(^4S)$ with O_2 in the thermospheric NO production rates. The thermalization cross section values for suprathermal $N(^4S)$ in collisions with N_2, O_2, He, and Ar are (3.8 ± 0.4), (2.8 ± 0.4), (1.8 ± 0.2), and (2.3 ± 0.2) in units of 10^{-15} cm^2, respectively.

The $O(^1S)$ formation processes from UV photolysis of O_3, N_2O, and H_2O_2 was studied. The $O(^1S)$ formation in the photodissociation of O_3 around 200 nm was observed for the first time, and the quantum yields at 193, 215, and 220 nm was determined to be $(2.5 \pm 1.1) \times 10^{-3}$, $(1.4 \pm 0.4) \times 10^{-4}$, and $(5 \pm 3) \times 10^{-5}$, respectively. The upper limit values of the quantum yields for $O(^1S)$ production from N_2O and H_2O_2 photolysis at 193 nm were determined to be 8×10^{-5} and 3×10^{-5}, respectively. The quantum yield for H atom production from H_2O_2 photolysis at 193 nm was also determined to be 0.20 ± 0.03. The pulsed laser photolysis / VUV-LIF technique was applied for the first time to the kinetic studies of $O(^1S)$. The rate coefficients of $O(^1S)$ with O_2, CO_2, H_2O, O_3, and HCl at 295 ± 2 K was determined to be $(2.85 \pm 0.31) \times 10^{-13}$, $(3.09 \pm 0.29) \times 10^{-13}$, $(6.38 \pm 0.38) \times 10^{-10}$, $(4.63 \pm 0.45) \times 10^{-10}$, and $(5.47 \pm 0.27) \times 10^{-10}$ cm^3 $molecules^{-1}$ s^{-1}, respectively. Based on the present laboratory data, the impact of $O(^1S)$ formation from the UV photolysis of O_3 on the OH production through $O(^1S) + H_2O$ reaction in the stratosphere and mesosphere was estimated. It was found that the relative contributions of the $O(^1S) + H_2O$ reaction against the $O(^1D) + H_2O$ reaction in the OH productions have its maximum at 30 km altitude and its contribution is about 2.5 %. The impact of direct formation of $O(^1S)$ in the UV photolysis of O_3 on the 557.7-nm dayglow emission in the mesosphere and lower thermosphere was also estimated. The contribution of the $O(^1S)$ formation in the O_3 photolysis was found to be of minor importance as an excitation process of 557.7-nm dayglow around 90 km altitude.

The present study has demonstrated that the VUV-LIF technique is a powerful tool to investigate the important photochemical processes involving $N(^4S)$ and $O(^1S)$ in the middle and upper atmosphere. The results in this thesis show that the photolytic formation of $N(^4S)$ and NO from N_2O can act as a new source of stratospheric NO_x, and that the reaction of H_2O with $O(^1S)$ which is formed from O_3 photolysis can act as a

new source of stratospheric and mesospheric HO_x. The kinetic data (quantum yield, rate coefficient, and thermalization cross section) determined precisely in the present study will be important for detail understanding of the photochemical processes related to the steady-state O_3 concentration in the middle atmosphere and $O(^1S)$ dayglow emission in the upper atmosphere.

Further laboratory studies of the photochemical reactions involving $N(^4S)$ and $O(^1S)$ atoms are necessary for detail understanding of the chemical process including NO_x and HO_x in the middle and upper atmosphere. In the present study, the rate coefficients for the reactions of $N(^4S)$ with NO and NO_2 at 295 ± 2 K have been determined. However, the temperature-dependent rate coefficients of these reactions are required for atmospheric model calculations to study the stratospheric and mesospheric reaction processes of $N(^4S)$ atoms. Only a limited number of the temperature-dependent kinetic studies for those $N(^4S)$ reactions have been reported previously and agreement between the resultant data is relatively poor. The pulse laser photolysis coupled with the VUV-LIF spectroscopy developed in the present study, which has been approved as a promising technique for kinetic studies at room temperature, is applicable to the temperature-dependent kinetic studies for the reactions involving $N(^4S)$ atoms at atmospheric temperatures. A temperature-controlled reaction chamber should be developed originally for the experiments. The state of the art technique of the VUV-LIF spectroscopy will provide precise kinetic data as a function of gas temperature and clarify the discrepancies reported in the previous studies.

The collisional relaxation rates of suprathermal $N(^4S)$ in collisions with N_2 and O_2 determined in the present study will make it possible to perform more precise model calculations relevant to the thermospheric NO formation processes. Using the thermalization cross section values obtained in the present study, a steady state translational energy distributions of $N(^4S)$ will be calculated as a function of altitude. To estimate the implications of the reaction of suprathermal $N(^4S)$ on the thermospheric NO formation, the energy-depend rate coefficients of the reaction of suprathermal $N(^4S)$ with O_2 are also needed. However, no laboratory study determining the energy-depend rate coefficients of the reaction of suprathermal $N(^4S)$ with O_2 has been reported. The relevant experimental techniques including the production of suprathermal $N(^4S)$ atom and the detection of the reaction products, NO or $O(^3P)$, should be applied for the

kinetic studies of the reaction. Development of a new experimental technique to produce suprathermal $N(^4S)$ atom without formation of NO and $O(^3P)$ is required.

In the present study, the impact of $O(^1S)$ formation from the UV photolysis of O_3 on the OH production through $O(^1S) + H_2O$ reaction has been estimated based on the present and available literature data. Since no laboratory study to determine the temperature dependence of the rate coefficients of $O(^1S)$ with H_2O has been reported, the rate coefficients at room temperature obtained in the present study was adopted in the estimation. If the rate coefficient of $O(^1S) + H_2O$ reaction had a significant temperature dependence, the result of the estimation would have changed. In future, determinations of the temperature dependence of the reactions of $O(^1S)$ with H_2O will be performed. The state of the art technique of the VUV-LIF detection of $O(^1S)$ will has a potential to be applied to the temperature-dependent studies.

The excitation processes of 557.7-nm dayglow and nightglow emissions around 90-100 km are still controversial. The three-body recombination process of atomic oxygen (Barth mechanism) is known as a primary excitation process for both dayglow and nightglow emission. As the excited state(s) of molecular oxygen in Barth mechanism, three candidates, $O_2(A\ ^3\Sigma_u^+)$, $O_2(c\ ^1\Sigma_u^-)$, and $O_2(A'\ ^3\Delta_u)$, have been proposed on the basis of energy considerations. However, no direct evidence about the molecular quantum states has been obtained. Beyond doubt, such the spectroscopic data is highly needed for complete understanding of the airglow emission processes. Further experimental studies for the energy transfer reactions of these candidates in collisions with $O(^3P)$ to produce $O(^1S)$ are required. In the my dissertation, laboratory experiments using the VUV-LIF technique with atmospheric model calculations have been made to clarify a discrepancy in the volume emission rates of 557.7-nm dayglow between the observation and model calculations. It has been found that, for the first time, the contribution of the $O(^1S)$ formation in the O_3 photolysis is of minor importance as an excitation process. The $O(^1S)$ formation in the VUV photolysis around 100-130 nm was also reported to be a candidate for excitation process. The quantum yields for $O(^1S)$ formation in the VUV photolysis of O_2 around 100-130 nm have not been well known. The VUV-LIF technique is applicable to the precise determinations of the quantum yields for $O(^1S)$ formation in the VUV photolysis of O_2 around 100-130 nm.

Acknowledgments

The present work was carried out at the Solar-Terrestrial Environment Laboratory (STEL), Nagoya University and was achieved under the supervision of Professor Yutaka Matsumi. Foremost, the author owes a special thanks to Prof. Yutaka Matsumi for the opportunity to work on this project and for providing guidance, comments, suggestions, and encouragements through the work. Dr. Kenshi Takahashi (STEL, Nagoya Univ.) is also acknowledged for his help, guidance, advice, and encouragements.

The author would like to thank to Prof. Kazuo Shiokawa (STEL, Nagoya Univ.), Prof. Akira Mizuno (STEL, Nagoya Univ.) and Dr. Noriyuki Tanaka (Univ. Alaska Fairbanks) for their valuable comments on the manuscript. The author is grateful to Prof. Masahiro Kawasaki (Kyoto Univ.), Prof. William R. Simpson (Univ. Alaska Fairbanks), and Dr. Timothy J. Wallington (Ford Motor Co.) for providing the opportunities to learn experimental skills in their laboratory.

The author wishes to acknowledge Dr. Nori Taniguchi and Prof. Sachiko Hayashida (Nara Women's Univ.) for providing the model calculations in Chapter 3 and Prof. Kazuhiko Shibuya (Tokyo Institute of Technology) for fruitful discussions on photolytic $N(^4S)$ formations in Chapter 4. The author would like to thank the technical staffs of the STEL; Mr. Noriji Toriyama, Mr. Hidehiko Jindou, Mr. Masahiro Kaneda, Mr. Hiroshi Nakada, and Mr. Masahiro Nagatani for their technical assistance. Special thanks are due to all the member of the Matsumi laboratory for the many fruitful discussions and assistance.

Finally, I am grateful to my family for their support and encouragements.